Supplementary Information

Solid–Vapor Synthesis of Dynamic Crystalline One-Dimensional Supramolecular Polymers from Amorphous Macrocycles

Qian Yang[1], Zhen Sun[1], Linnan Zhang[1], Jingwei Huang[1], Wang Xie[1], Leyong Wang[1], and Kecheng Jie[1,*]

[1]State Key Laboratory of Coordination Chemistry, Key Laboratory of Mesoscopic Chemistry of MOE, Jiangsu Key Laboratory of Advanced Organic Materials, School of Chemistry and Chemical Engineering, Nanjing University, Nanjing 210023, P. R. China

*Correspondence should be addressed to K.J. (email: jiekecheng@nju.edu.cn)

Table of Contents

1. Materials and methods

1.1. Chemicals and materials.

All reagents and solvents were commercially available and used as supplied without further purification.

1.2. Solution NMR.

Solution ^{1}H NMR, ^{13}C NMR, NOESY and DOSY spectra were recorded with BRUKER AVANCE III HD 400, 500 or 600 MHz instruments at 298 K.

1.3. High-resolution mass spectrometry (HR-MS).

The HR-MS spectra were obtained on Thermo Scientific™ Q Exactive™ mass spectrometer equipped with an ESI and APCI ion source.

1.4. Thermogravimetric analysis (TGA).

TGA was performed under N_2 atmosphere with a heating rate of 10 °C/min using Netzsch STA 449 F3 thermal analyzer.

1.5. Powder X-ray diffraction (PXRD).

PXRD patterns were recorded on Bruker D8 Advance diffractometer with Cu Kα radiation (λ = 1.5418 Å) at room temperature. Data were measured over the range of 4–40° at a scan rate of 0.15 sec/step for 4 minutes.

1.6. Single crystal X-ray diffraction (SC-XRD).

SC-XRD data were collected on Bruker D8 venture diffractometer equipped with a PHOTON-100 COMS detector (Mo-Kα, λ = 0.71073 Å, and Ga-Kα, λ = 1.34139 Å) at 193 K or 293K.

1.7. Dynamic light scattering (DLS).

DLS data were collected on 90PLUS PALS (Bruker) using a glass cuvette (Starna Cells, Inc.) with 830 nm diode laser as a light source, using a fixed angle (90°) at 298 K.

1.8. Differential scanning calorimetry (DSC).

DSC curves were collected using Mettler-Toledo DSC1 STARe analyzer under N_2 atmosphere (flow rate of 50 mL min^{-1}). The samples were heated at 1 °C/min or 2 °C/min using N_2 as the protective

gas.

1.9. Temperature-variable powder X-ray diffraction (VT-PXRD).

Temperature-variable PXRD patterns were collected using Bruker D8 Advance diffractometer with Cu Kα radiation (λ = 1.5418 Å) over the range of 30–165 °C, with data acquisition every 10 °C or 5 °C at a scan rate of 0.4 sec/step. The sample was held for 50 minutes at temperatures between 30–150 °C before measurement, and for 20 minutes at temperatures between 155–165 °C before measurement.

1.10. Theoretical calculations.

All quantum chemical calculations were performed using Gaussian 16 Rev. C.01. The ground-state geometries of all studied molecules and complexes were fully optimized using the B3LYP functional[1–3] with Grimme's D3 dispersion correction and Becke–Johnson damping[4]. The 6-31G(d)[5, 6] basis set was employed for all atoms. Vibrational frequency calculations were performed at the same level. All optimized structures were confirmed to be local minima on the potential energy surface by the absence of imaginary frequencies. Single-point energy calculations were performed at the PBE0/def2-TZVP level[7, 8]. Wavefunction analyses were performed using Multiwfn 3.8 (dev)[9, 10]. Noncovalent interaction analyses were conducted using the Independent Gradient Model based on Hirshfeld partition (IGMH)[11]. All visualizations were generated using Visual Molecular Dynamics software[12]. Initial structures were extracted from the SC-XRD structures of CSP-1 and DCE@P5PA-2C_6N.

2. Synthetic procedures of three macrocycle precursors

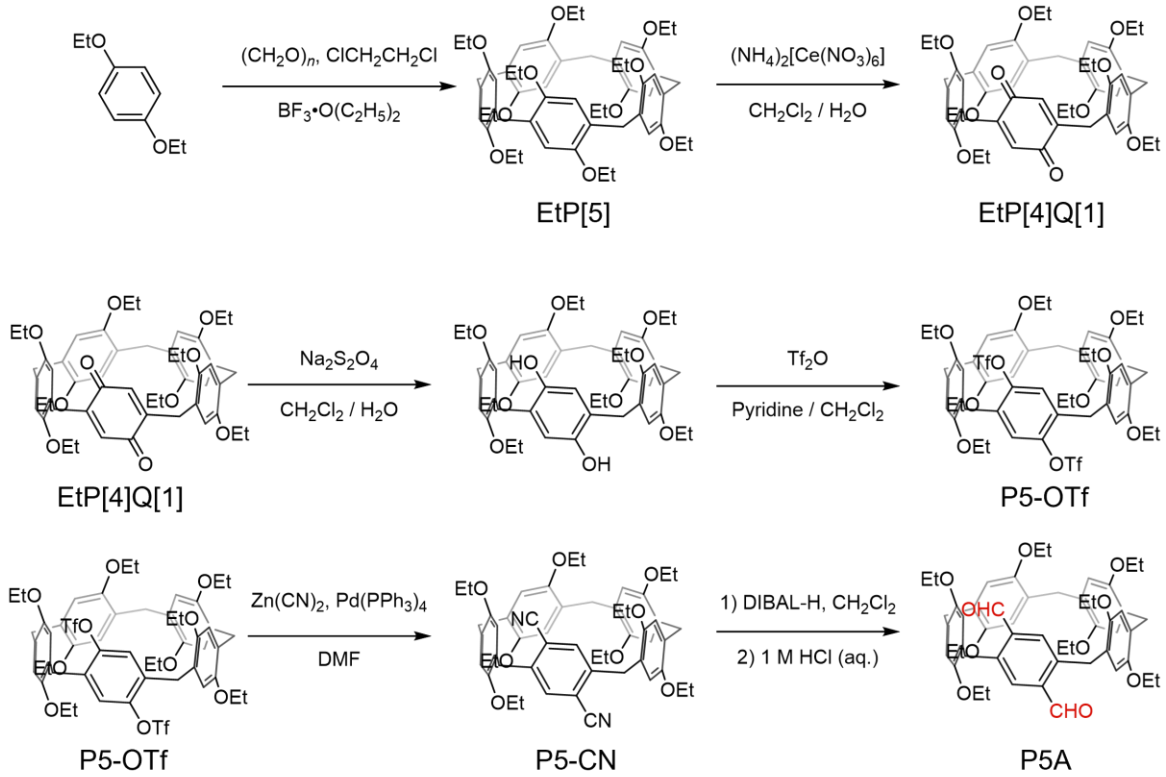

P5-OTf: EtP[5] (6.00 g, 6.74 mmol) was dissolved in dichloromethane (250 mL), and an aqueous solution of diammonium cerium (IV) nitrate (CAN, 7.40 g, 13.35 mmol in 40 mL of water) was added dropwise. The reaction mixture was stirred at room temperature for 30 min. After completion of the reaction, the organic phase was separated, washed with water (3×30 mL), dried over anhydrous Na_2SO_4 and concentrated. The crude product was purified by silica gel column chromatography using dichloromethane/hexane (2:1) to afford EtP[4]Q[1] as a red solid (3.66 g, 65% yield). Subsequently, EtP[4]Q[1] (3.66 g, 4.38 mmol) was dissolved in dichloromethane (200 mL), and an aqueous solution of $Na_2S_2O_4$ (3.81 g, 21.92 mmol in 50 mL of water) was added. The mixture was stirred at room temperature overnight. After the reaction was complete, the solution became colorless. The organic layer was separated, washed with water (3×30 mL) and concentrated to give a white solid, which was used directly in the subsequent step without further purification. Finally, the resulting white solid was dissolved in mixture of dry dichloromethane/pyridine (120 mL:8 mL), and trifluoromethanesulfonic anhydride (Tf_2O, 3.29 mL, 6.57 mmol) was added dropwise at 0 °C under a nitrogen atmosphere. The reaction mixture was stirred overnight at room temperature and then quenched with water. The organic phase was separated, washed with water (3×30 mL) and concentrated. The crude product was purified via silica gel column chromatography using dichloromethane/hexane (4:1) to afford P5-OTf as a white powder (3.65 g, 76% yield).

P5-CN: P5-OTf (1.00 g, 0.92 mmol) was dissolved in dry N,N-dimethylformamide (DMF, 30 mL). Under a nitrogen atmosphere, $Zn(CN)_2$ (0.24 g, 2.01 mmol) and $Pd(PPh_3)_4$, (0.16 g, 0.14 mmol) were added sequentially. The reaction mixture was heated at 100 °C and stirred overnight. After completion of the reaction, the mixture was cooled to room temperature and poured into water (80 mL) with stirring. The resulting mixture was extracted with ethyl acetate (3×40 mL). The combined organic layers were washed with water (3×30 mL), dried over anhydrous Na_2SO_4 and concentrated. The crude product was purified by silica gel column chromatography using dichloromethane/hexane (1:1) to afford P5-CN as a yellow solid (0.47 g, 70% yield).

P5A: DIBAL-H (2.11 mL, 1.0 M in hexane, 2.11 mmol) was added dropwise into a solution of P5-CN (0.45 g, 0.53 mmol) in 150 mL of dichloromethane at 0 °C overnight. After the reaction was deemed complete, the reaction was quenched with 1 M HCl (20 mL). The separated organic layer was washed with water (3×30 mL), dried over anhydrous Na_2SO_4 and concentrated. Then the crude product was purified via silica gel column chromatography using dichloromethane/hexane (1:1) as the eluent. And the yellow product P5A (0.29 g, 65% yield) was obtained and dried *in vacuo* at 120 °C overnight to afford the desolvated phase. ^{1}H NMR (400 MHz, $CDCl_3$, 298 K) δ 10.49 (s, 2H), 7.83 (s, 2H), 6.71 (s, 2H), 6.65 (s, 2H), 6.63 (s, 4H), 4.24 (s, 4H), 3.88–3.69 (m, 22H), 1.30–1.20 (m, 18H), 1.11 (t, J = 7.0 Hz, 6H). ^{13}C NMR (101 MHz, $CDCl_3$, 298 K) δ 192.56, 150.23, 150.01, 149.97, 149.42, 142.06, 136.52, 132.86, 130.11, 129.02, 128.31, 126.44, 123.61, 115.31, 115.24, 114.93, 114.67, 64.42, 64.07, 63.52, 31.65, 31.31, 30.29, 30.01, 29.84, 15.17, 15.09, 15.06, 14.64. HR-MS (m/z) calcd. for $C_{53}H_{62}O_{10}$, $[M+NH_4]^+$: 876.4681, found, 876.4666; $[M+Na]^+$: 881.4235, found, 881.4221.

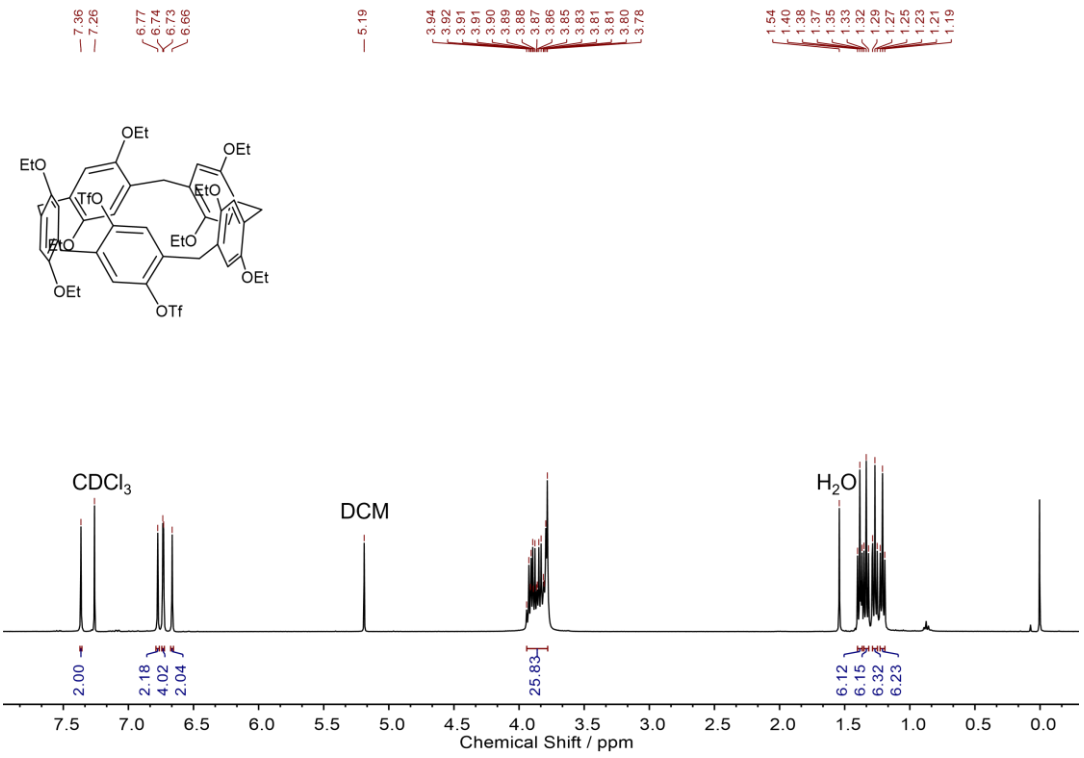

Supplementary Figure 1. ^{1}H NMR spectrum (400 MHz, $CDCl_3$, 298 K) of P5-OTf.

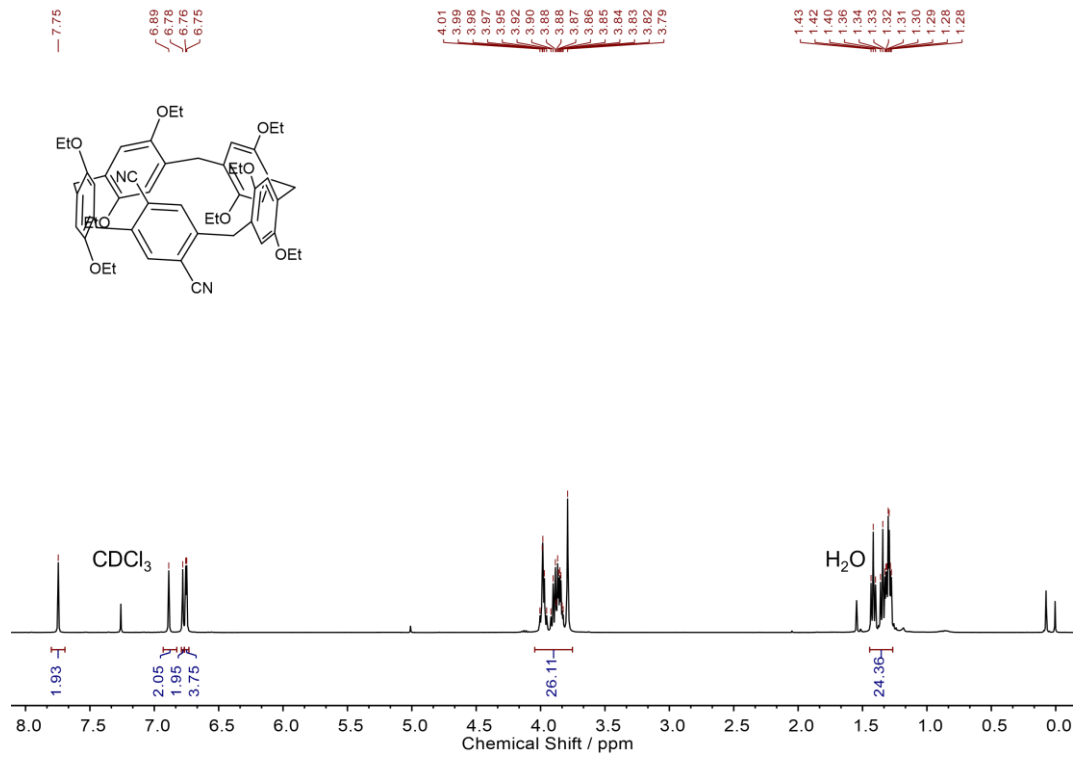

Supplementary Figure 2. ^{1}H NMR spectrum (400 MHz, $CDCl_3$, 298 K) of P5-CN.

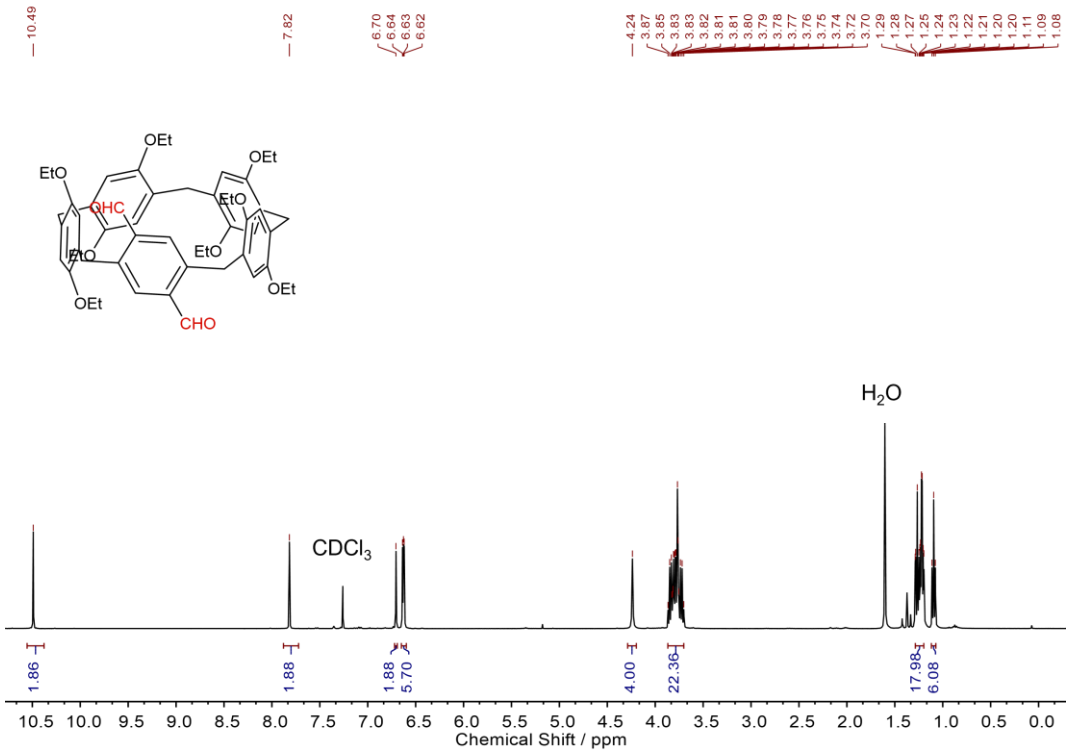

Supplementary Figure 3. ^{1}H NMR spectrum (400 MHz, $CDCl_3$, 298 K) of P5A after desolvation.

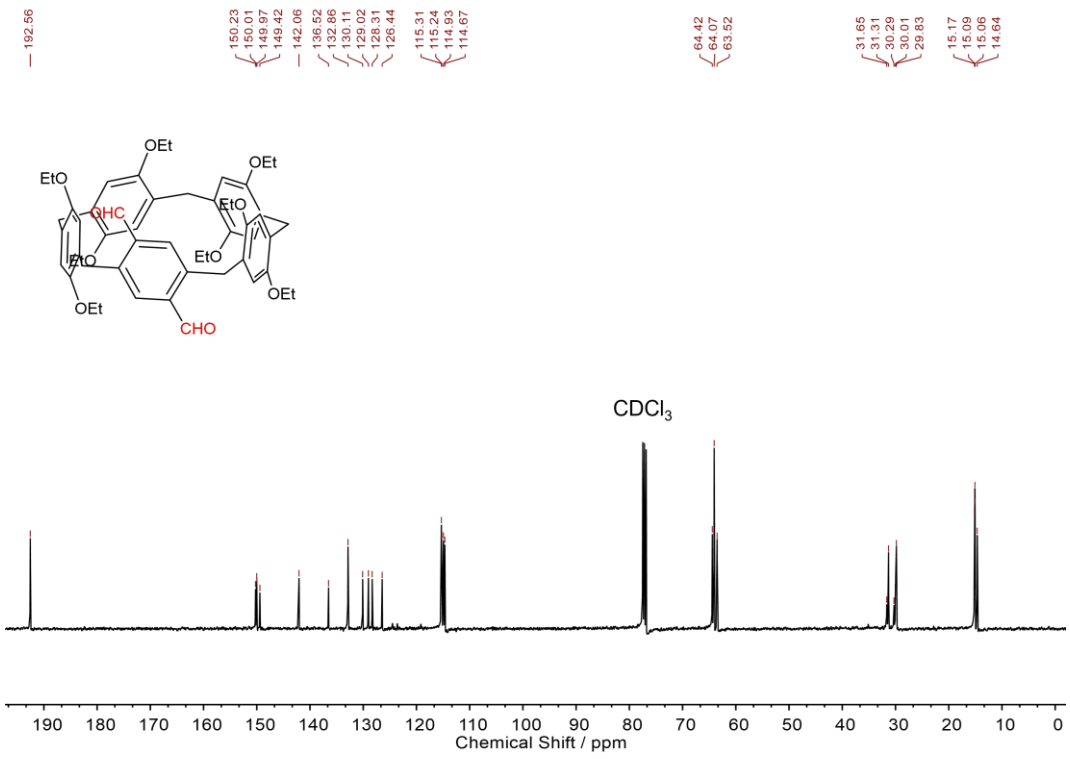

Supplementary Figure 4. ^{13}C NMR spectrum (101 MHz, $CDCl_3$, 298 K) of P5A.

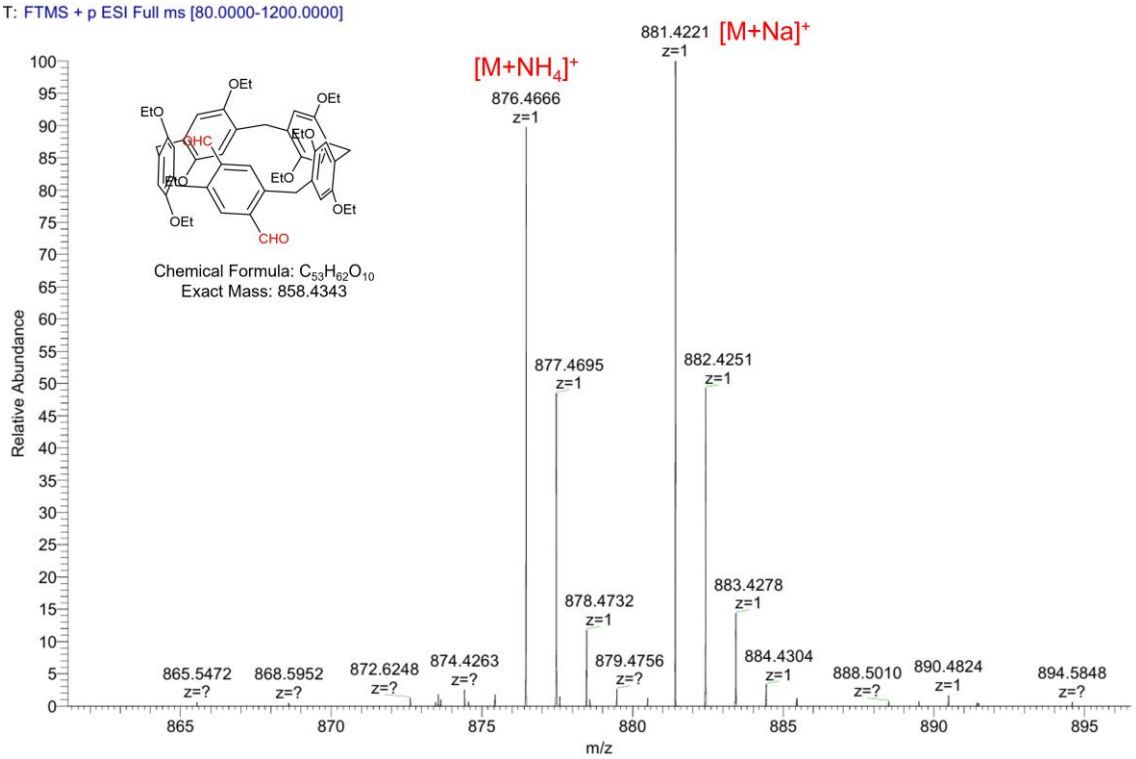

Supplementary Figure 5. HR-MS spectrum of P5A.

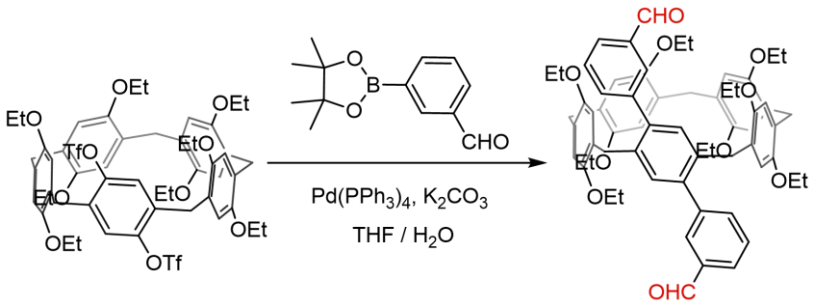

P5-OTf P5MA

P5MA: Under the protection of nitrogen, P5-OTf (1.00 g, 0.92 mmol), 3-formylphenylboronic acid pinacol ester (0.64 g, 2.75 mmol), $Pd(PPh_3)_4$ (0.16 g, 0.14 mmol) and K_2CO_3 (0.38 g, 2.74 mmol) were heated at reflux in mixture of THF/H_2O (200 mL:20 mL) for 36 h. After the solvent was removed under vacuum, the mixture was extracted with dichloromethane (3×20 mL). The organic layer was washed with water (3×30 mL), dried over anhydrous Na_2SO_4 and concentrated. Then the crude product was purified via silica gel column chromatography using dichloromethane/hexane (1:1) as the eluent. And the white product P5MA (0.40 g, 43% yield) was obtained and dried *in vacuo* at 120 °C overnight to afford the desolvated phase. ^{1}H NMR (400 MHz, $CDCl_3$, 298 K) δ 9.92 (s, 2H), 7.83 (dt, J = 7.7, 1.4 Hz, 2H), 7.58 (t, J = 1.7 Hz, 2H), 7.37 (t, J = 7.6 Hz, 2H), 7.18 (dt, J = 7.6, 1.5 Hz, 2H), 6.99 (s, 2H), 6.82 (s, 2H), 6.73 (s, 2H), 6.51 (s, 2H), 5.90 (s, 2H), 3.99-3.49 (m, 26H), 1.41 (t, J = 6.9 Hz, 6H), 1.20 (t, J = 6.9 Hz, 6H), 1.14 (t, J = 6.9 Hz, 6H), 0.87 (t, J = 6.9 Hz, 6H). ^{13}C NMR (101 MHz, $CDCl_3$, 298 K) δ 192.39, 150.23, 150.13, 149.69, 149.62, 143.15, 139.58, 137.09, 136.28, 135.51, 132.10, 131.35, 129.62, 129.21, 128.83, 128.80, 127.40, 127.32, 115.40, 115.27, 115.18, 114.79, 64.27, 64.15, 63.40, 33.28, 30.07, 29.67, 15.41, 15.21, 14.97, 14.59. HR-MS (m/z) calcd. for $C_{65}H_{70}O_{10}$, $[M+H]^+$: 1011.5003; found, 1011.4998.

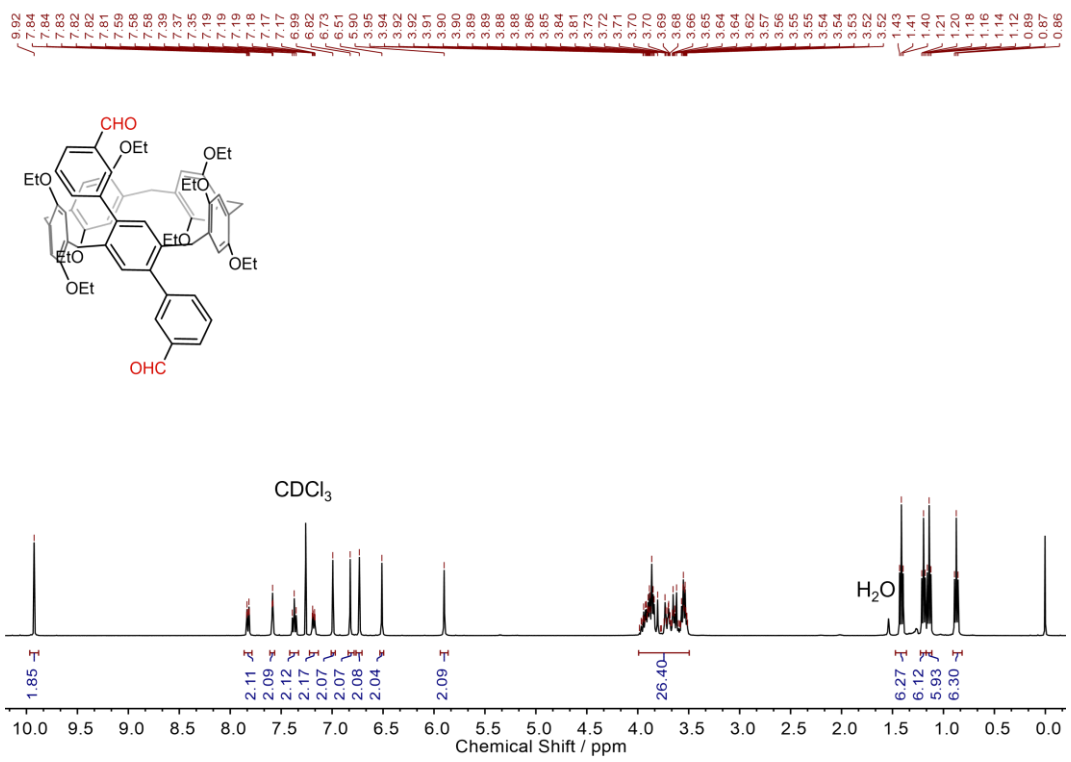

Supplementary Figure 6. ^{1}H NMR spectrum (400 MHz, $CDCl_3$, 298 K) of P5MA after desolvation.

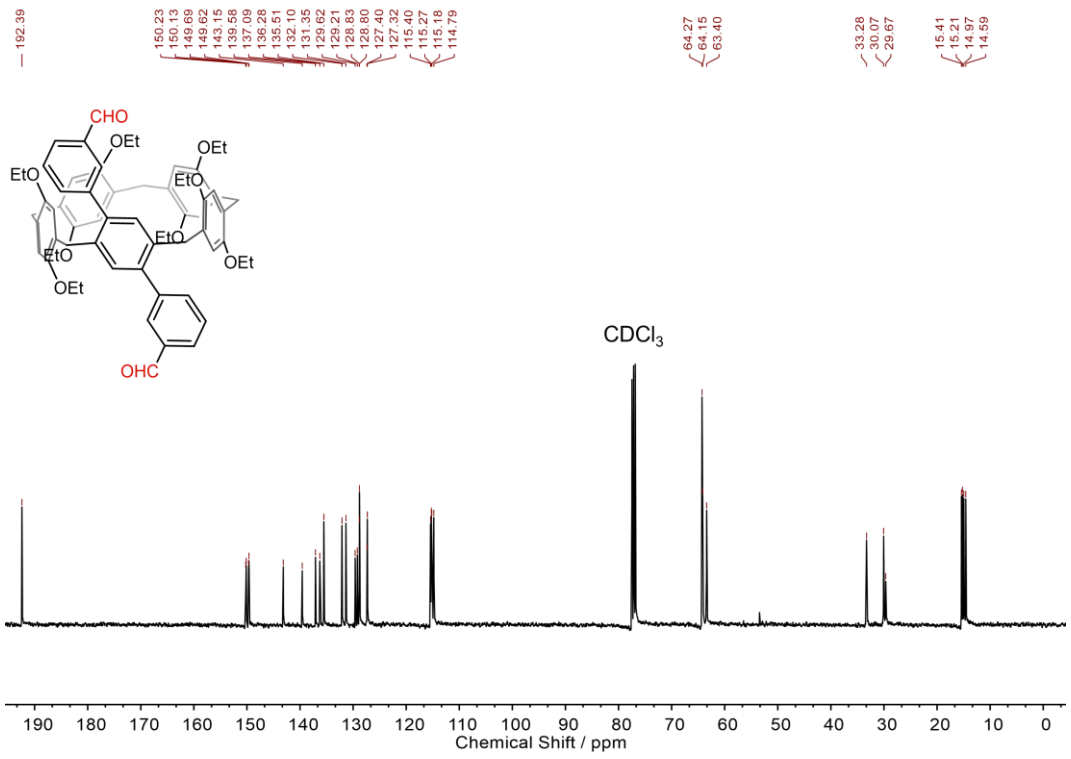

Supplementary Figure 7. ^{13}C NMR spectrum (101 MHz, $CDCl_3$, 298 K) of P5MA.

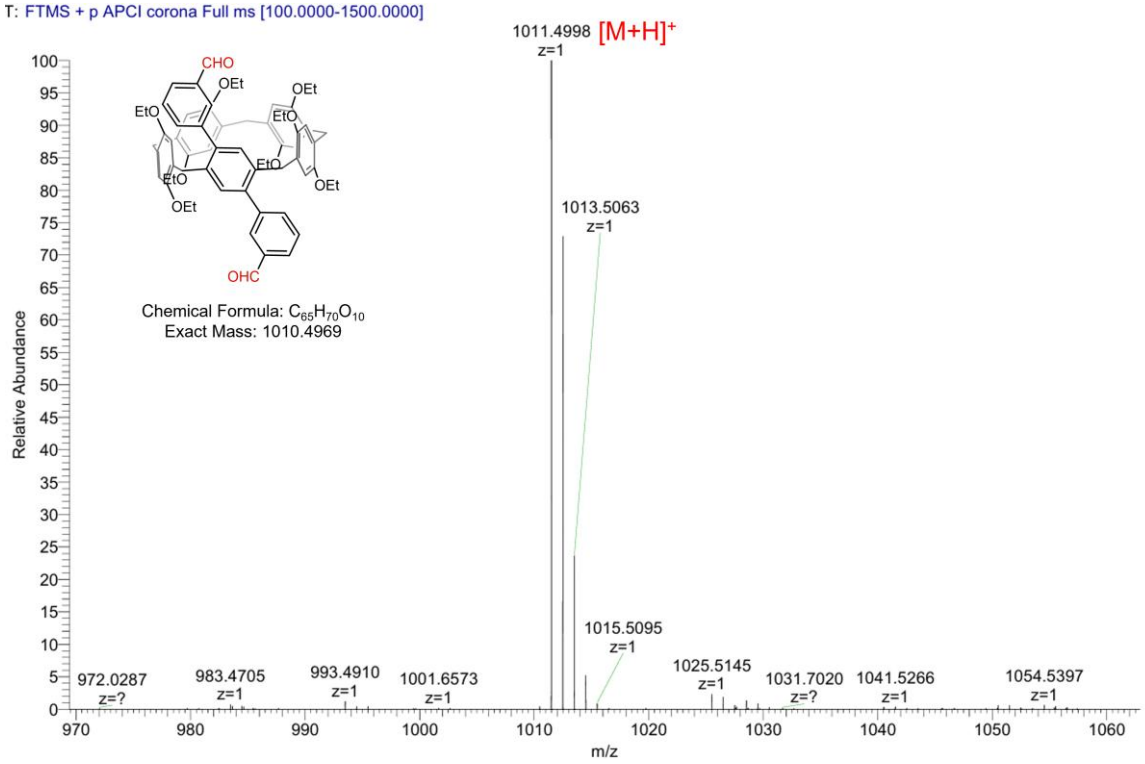

Supplementary Figure 8. HR-MS spectrum of P5MA.

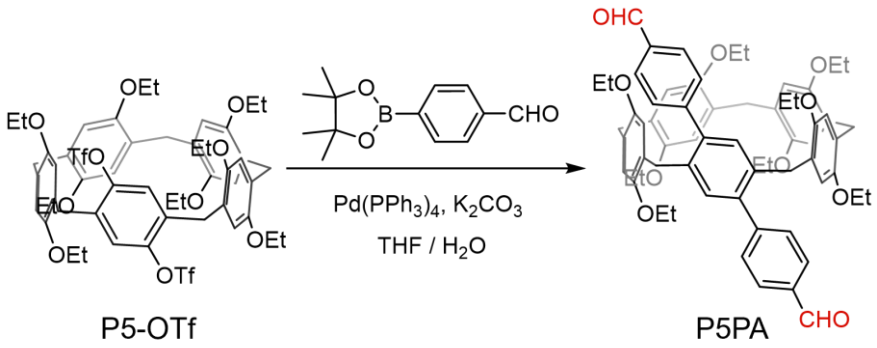

P5PA: Under the protection of nitrogen, P5-OTf (1.00 g, 0.92 mmol), 4-formylphenylboronic acid pinacol ester (0.64 g, 2.75 mmol), $Pd(PPh_3)_4$ (0.16 g, 0.14 mmol) and K_2CO_3 (0.38 g, 2.74 mmol) were heated at reflux in mixture of THF/H_2O (200 mL:20 mL) for 36 h. After the solvent was removed under vacuum, the mixture was extracted with dichloromethane (3×20 mL). The organic layer was washed with water (3×30 mL), dried over anhydrous Na_2SO_4 and concentrated. Then the crude product was purified via silica gel column chromatography using dichloromethane/hexane (1:1) as the eluent. And the white product P5PA (0.52 g, 56% yield) was obtained and dried *in vacuo* at 120 °C overnight to afford the desolvated phase.^{1}H NMR (400 MHz, $CDCl_3$, 298 K) δ 10.07 (s, 2H), 7.73 (d, J = 8.0 Hz, 4H), 7.14 (d, J = 7.8 Hz, 4H), 6.93 (s, 2H), 6.78 (d, J = 9.1 Hz, 4H), 6.55 (s, 2H), 5.87 (s, 2H), 4.05–3.44 (m, 26H), 1.44 (t, J = 7.0 Hz, 6H), 1.18 (t, J = 6.9 Hz, 6H), 1.12 (t, J = 7.0 Hz, 6H), 0.92 (t, J = 6.9 Hz, 6H). ^{13}C NMR (101 MHz, $CDCl_3$, 298 K) δ 192.19, 150.42, 150.07, 149.82, 149.63, 148.76, 139.89, 136.96, 134.88, 131.86, 130.05, 129.63, 129.48, 128.99, 127.30, 115.73, 115.42, 115.16, 114.94, 64.63, 64.31, 63.98, 63.51, 33.70, 30.24, 29.18, 15.47, 15.21, 14.95, 14.65. HR-MS (m/z) calcd. for $C_{65}H_{70}O_{10}$, $[M+H]^+$: 1011.5003; found, 1011.4998.

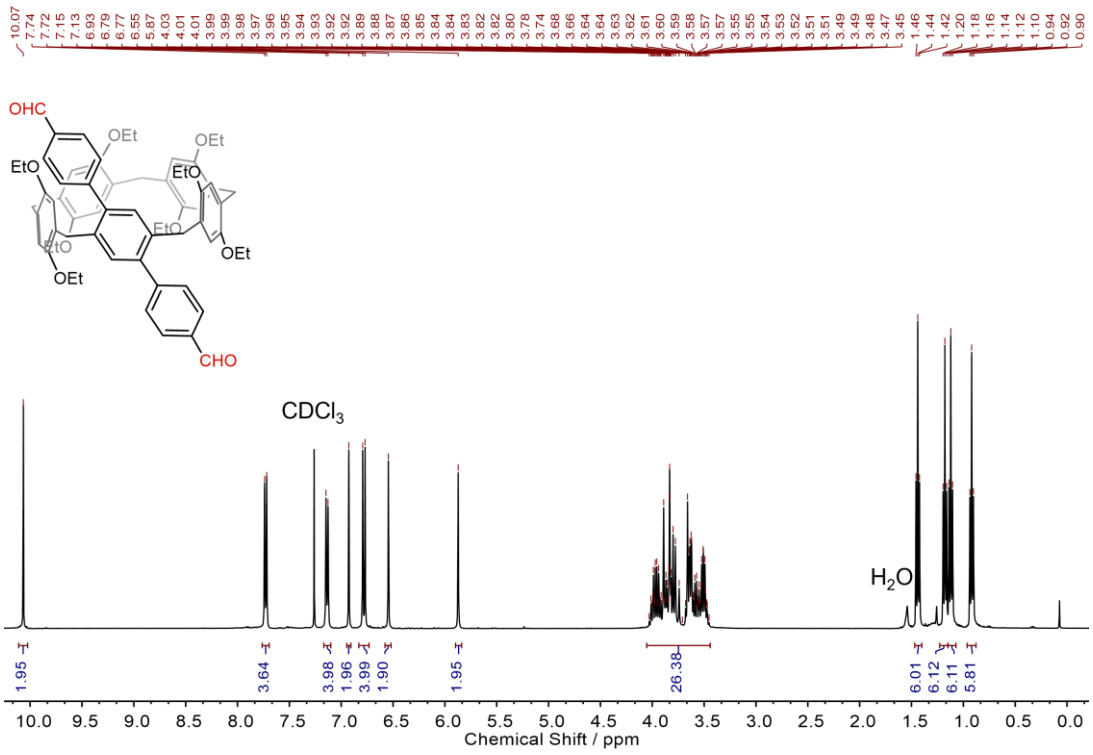

Supplementary Figure 9. ^{1}H NMR spectrum (400 MHz, $CDCl_3$, 298 K) of P5PA after desolvation**.**

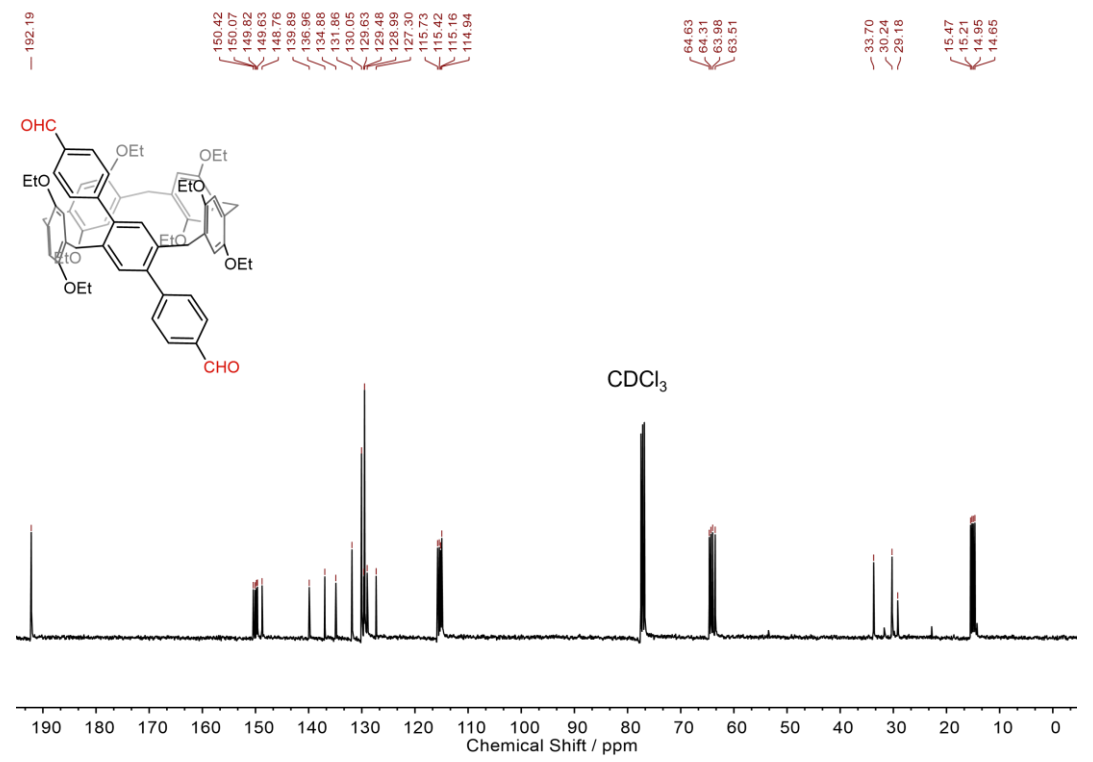

Supplementary Figure 10. ^{13}C NMR spectrum (101 MHz, $CDCl_3$, 298 K) of P5PA.

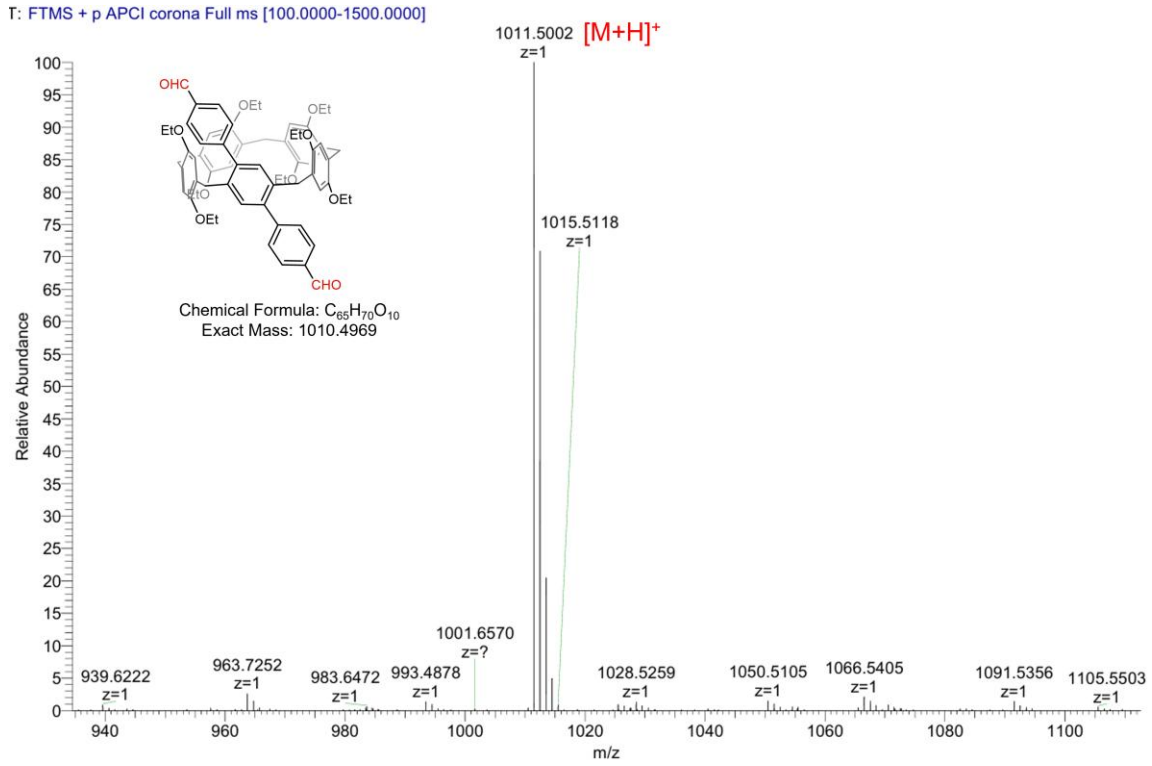

Supplementary Figure 11. HR-MS spectrum of P5PA.

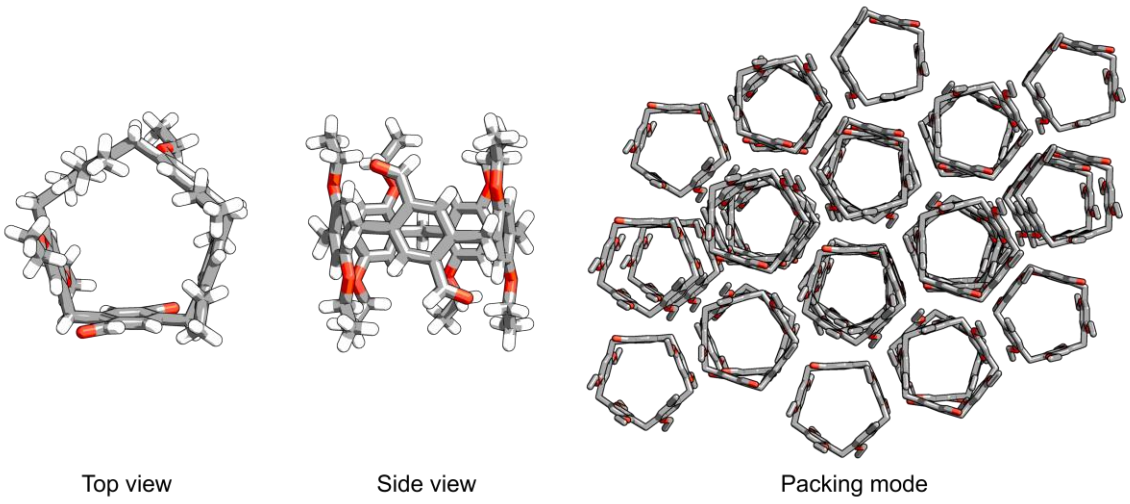

Supplementary Figure 12. SC-XRD structure of P5A. Solvent molecules are removed for clarity.

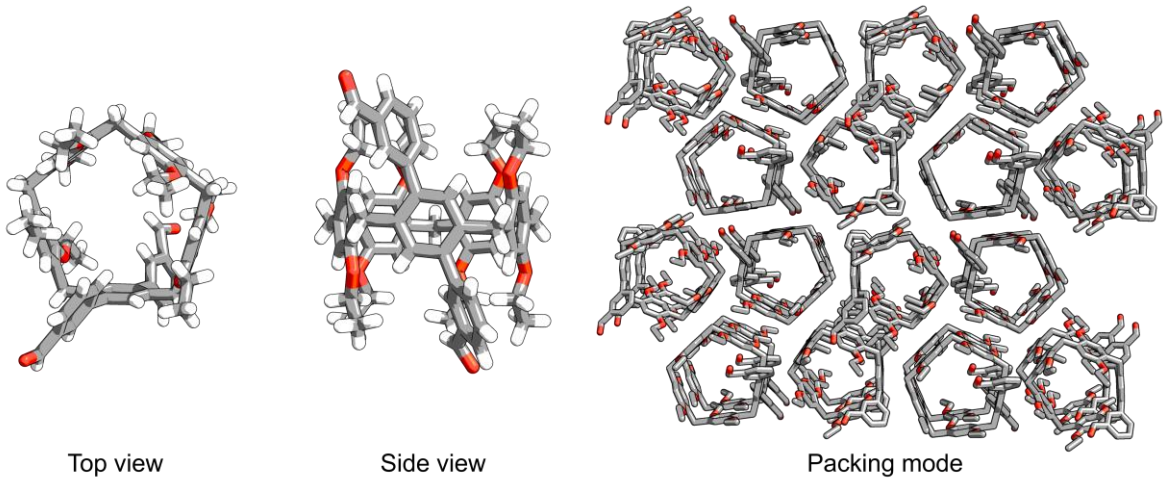

Supplementary Figure 13. SC-XRD structure of P5MA. Solvent molecules are removed for clarity.

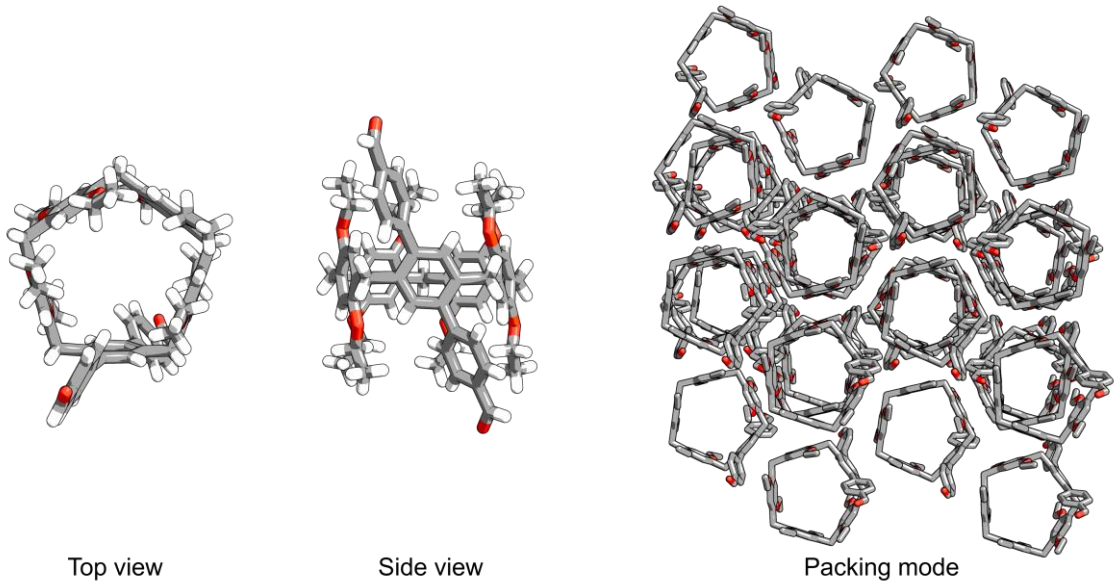

Supplementary Figure 14. SC-XRD structure of P5PA. Solvent molecules are removed for clarity.

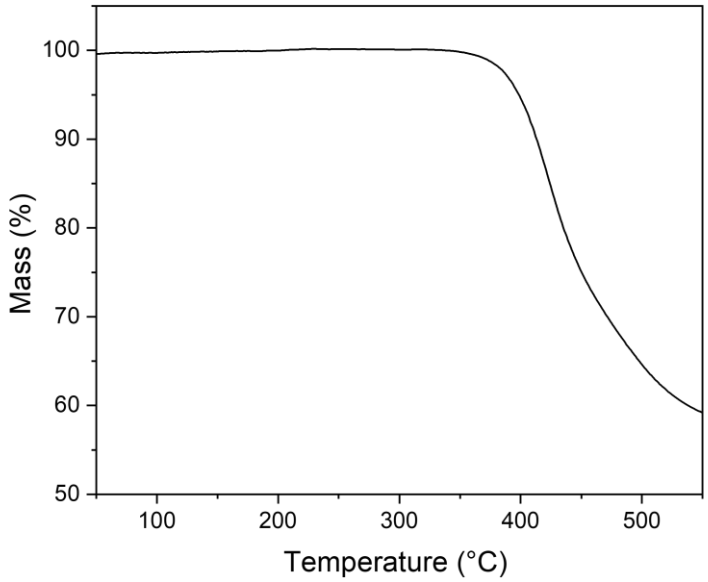

Supplementary Figure 15. TGA curve of P5A after desolvation.

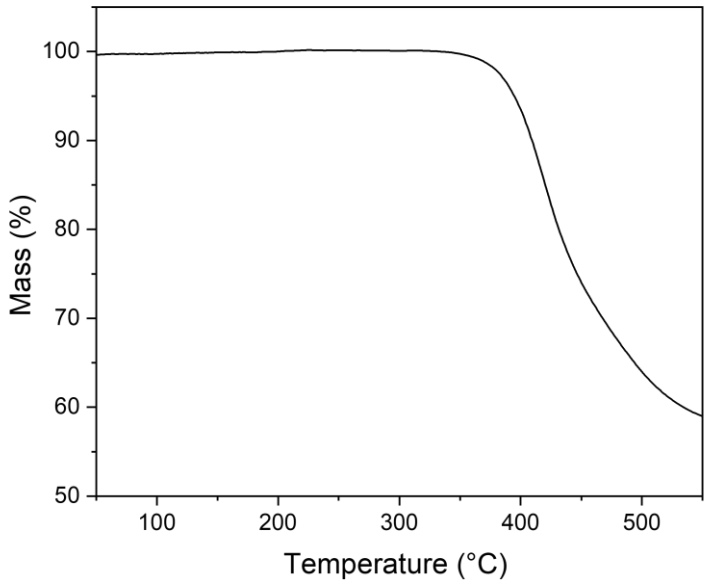

Supplementary Figure 16. TGA curve of P5MA after desolvation.

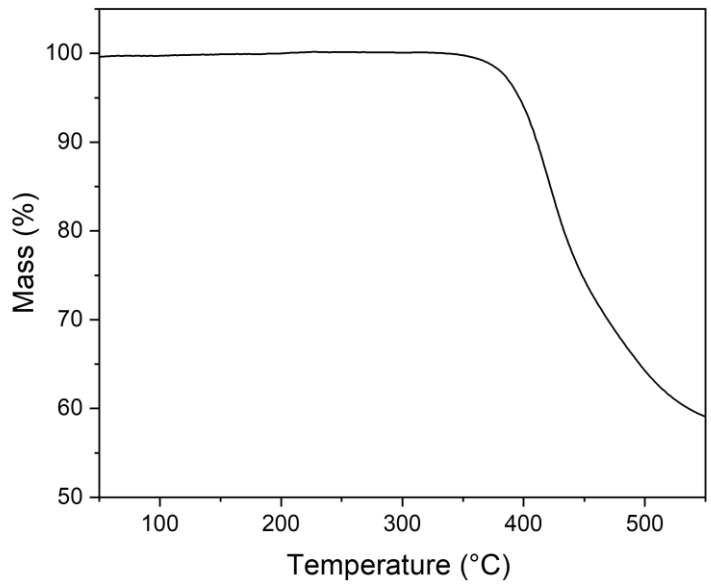

Supplementary Figure 17. TGA curve of P5PA after desolvation.

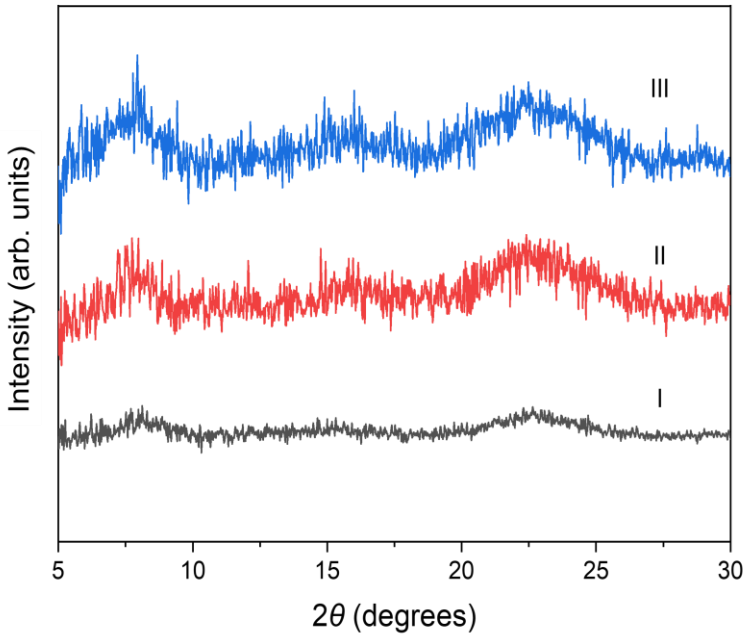

Supplementary Figure 18. PXRD patterns of activated precursors: (I) P5A; (II) P5MA; (III) P5PA.

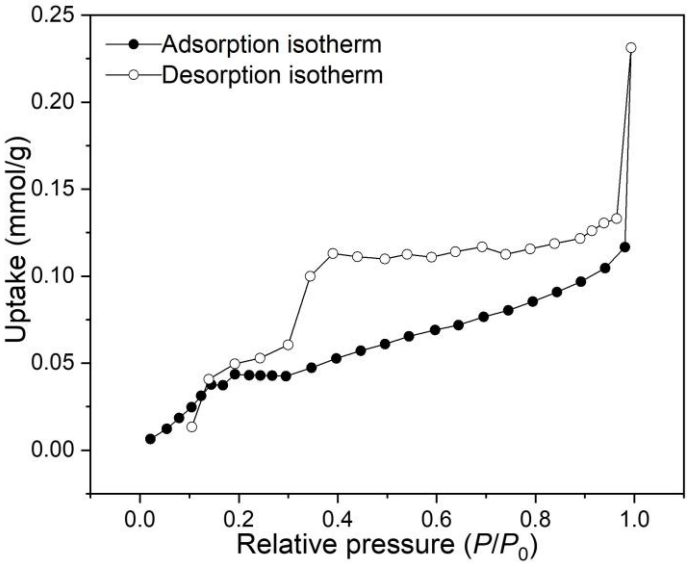

Supplementary Figure 19. N_2 adsorption and desorption isotherms at 77 K for activated P5A.

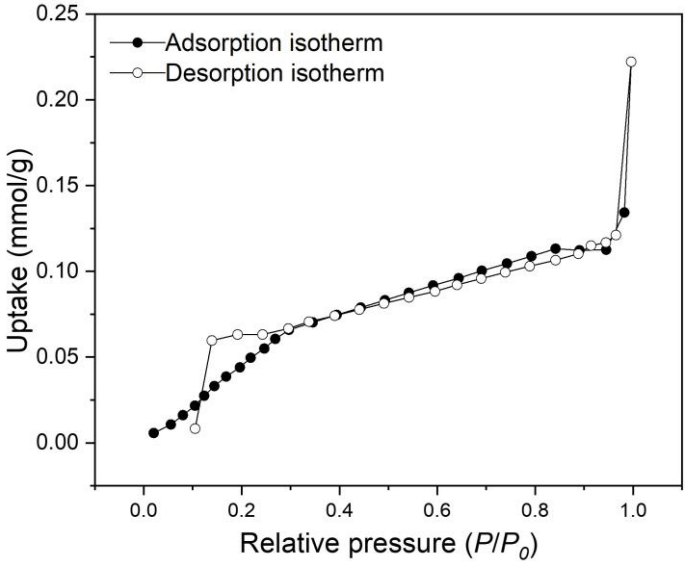

Supplementary Figure 20. N_2 adsorption and desorption isotherms at 77 K for activated P5MA.

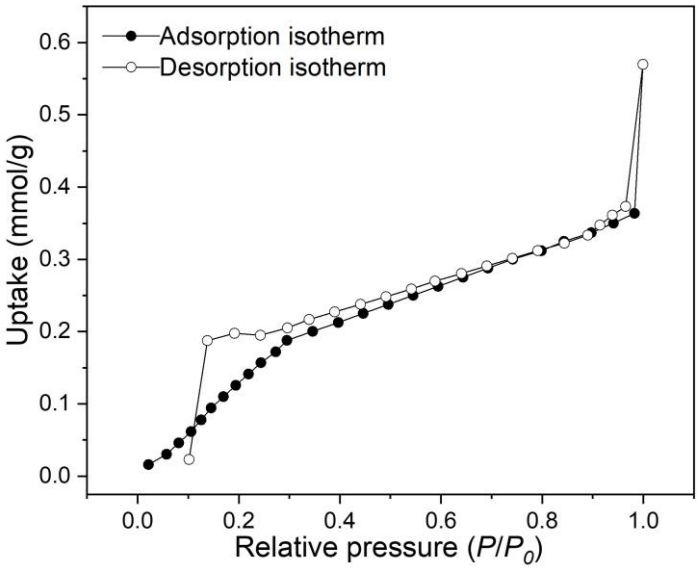

Supplementary Figure 21. N_2 adsorption and desorption isotherms at 77 K for activated P5PA.

Supplementary Table 1. Summary of BET surface area and pore volume for the three activated precursors obtained from 77 K N_2 adsorption isotherms.

Precursors	BET (m^2/g)	Pore Volume (cm^3/g)	Micropore Volume (cm^3/g)
P5A	4.3716	0.0070	0
P5MA	7.9119	0.0063	0
P5PA	22.7421	0.0158	0

3. Solid–vapor synthesis and *in situ* solution growth of *n*-alkyl-appended imine derivatives

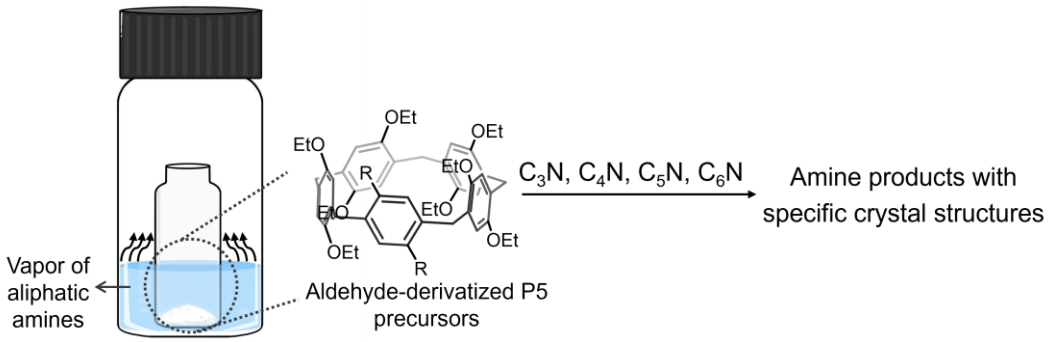

Supplementary Figure 22. Schematic representation of solid–vapor synthesis. Activated macrocycle precursors were exposed to vapors of aliphatic amines in a sealed vial under ambient conditions to afford the corresponding imine derivatives.

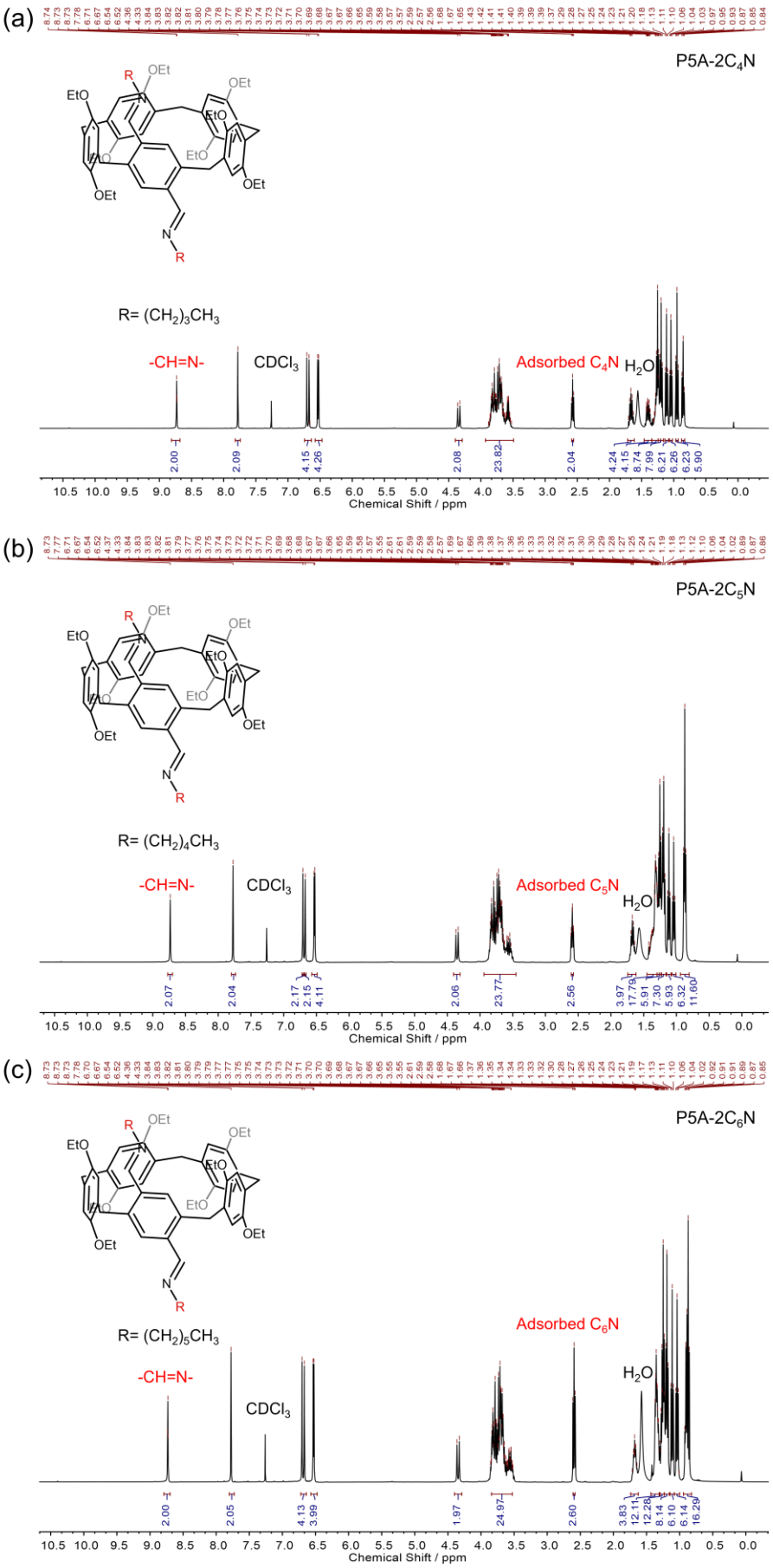

Supplementary Figure 23. ^{1}H NMR spectrum (400 MHz, $CDCl_3$, 298 K) of P5A after exposure to aliphatic amine vapors: (a) C_4N, (b) C_5N and (c) C_6N.

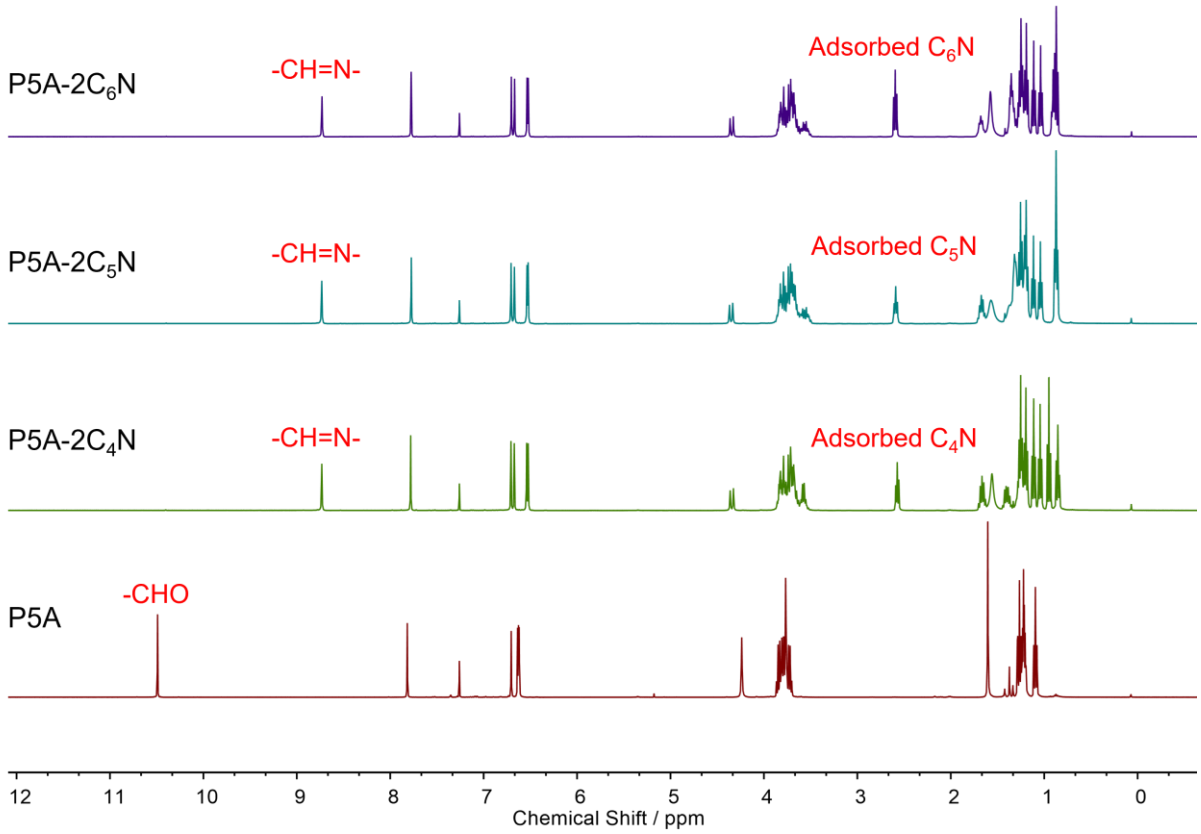

Supplementary Figure 24. Stacked ^{1}H NMR spectra (400 MHz, $CDCl_3$, 298 K) of P5A and the corresponding solid–vapor products after exposure to C_4N, C_5N and C_6N vapors (from bottom to top).

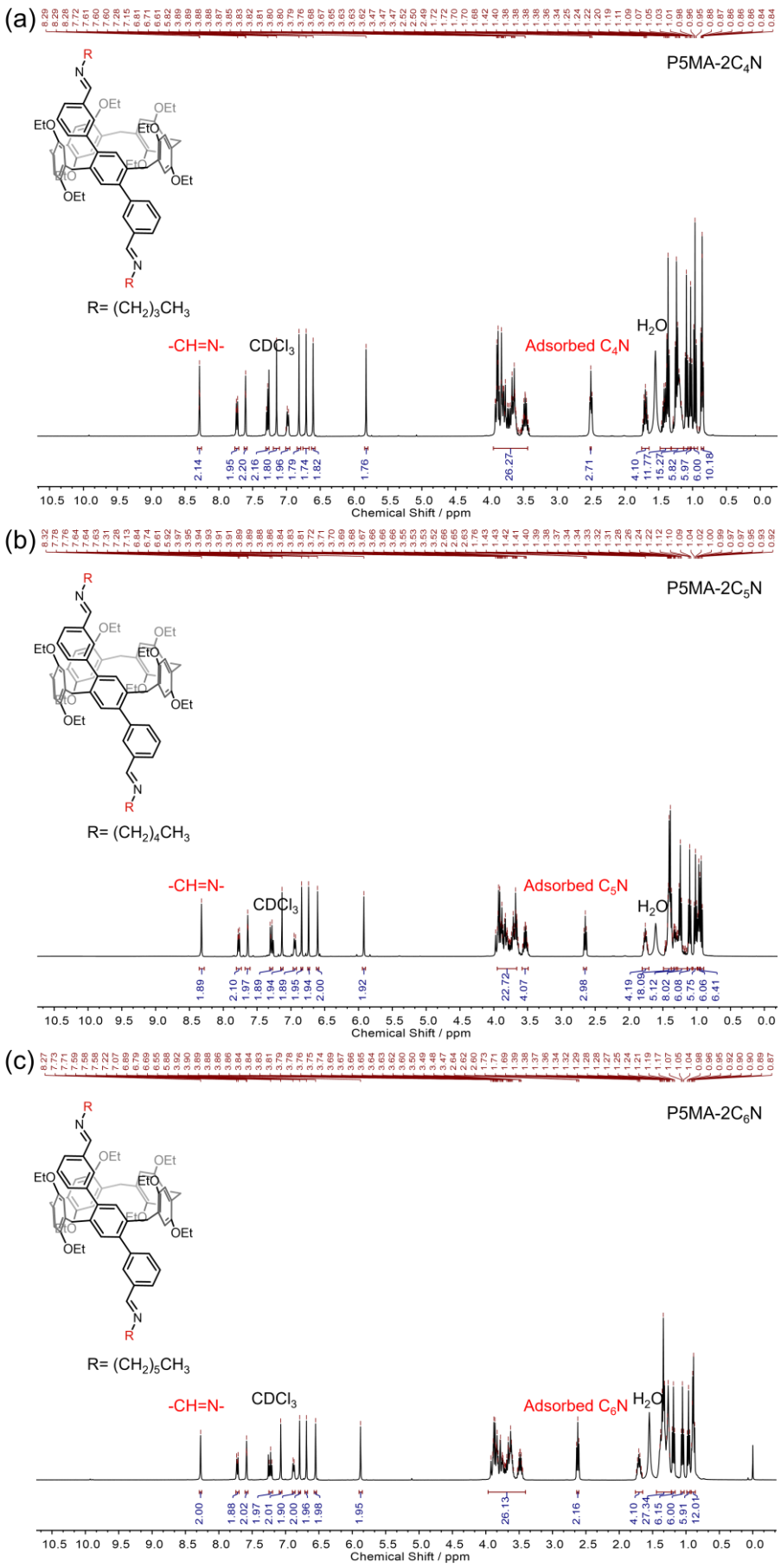

Supplementary Figure 25. ^{1}H NMR spectrum (400 MHz, $CDCl_3$, 298 K) of P5MA after exposure to aliphatic amine vapors: (a) C_4N, (b) C_5N and (c) C_6N.

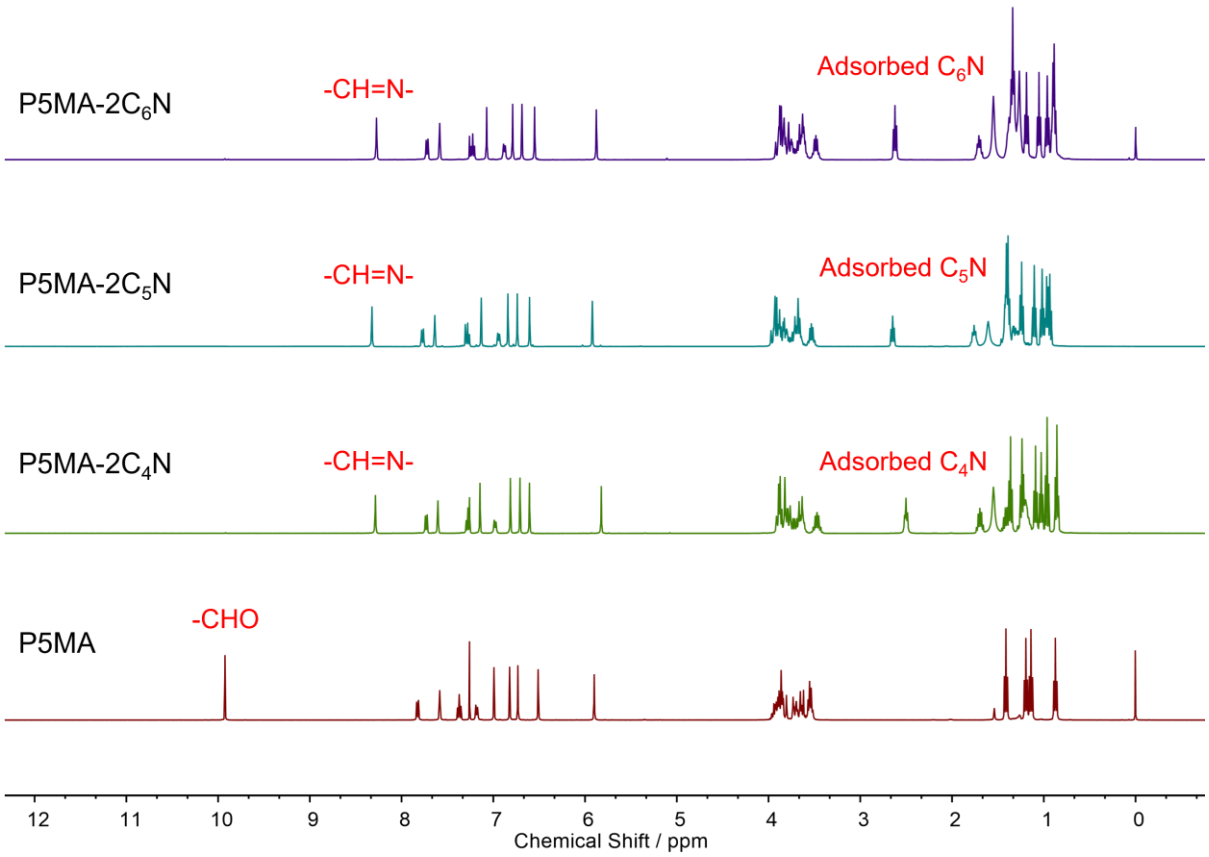

Supplementary Figure 26. Stacked ^{1}H NMR spectra (400 MHz, $CDCl_3$, 298 K) of P5MA and the corresponding solid–vapor products after exposure to C_4N, C_5N and C_6N vapors (from bottom to top).

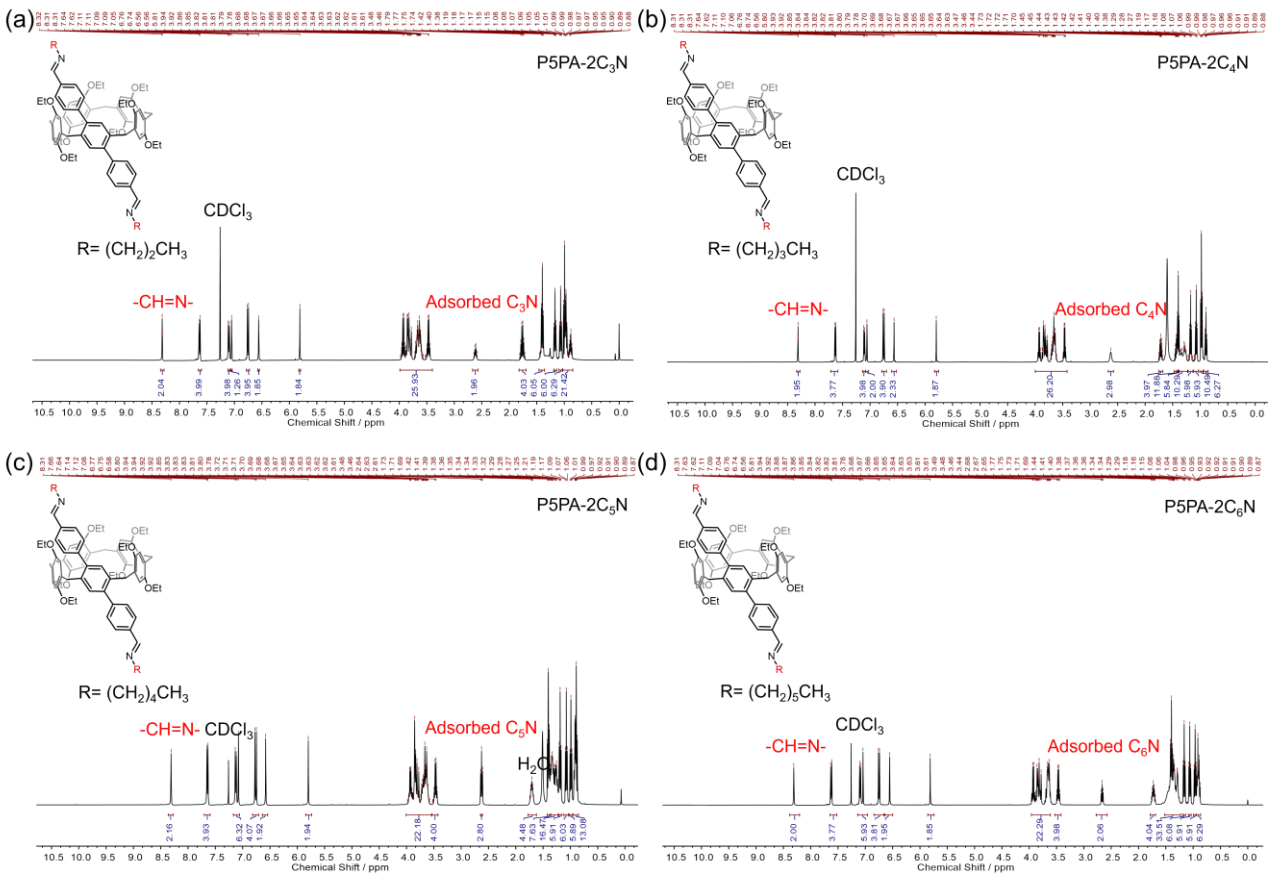

Supplementary Figure 27. ^{1}H NMR spectrum (400 MHz, $CDCl_3$, 298 K) of P5PA after exposure to aliphatic amine vapors: (a) C_3N, (b) C_4N, (c) C_5N and (d) C_6N.

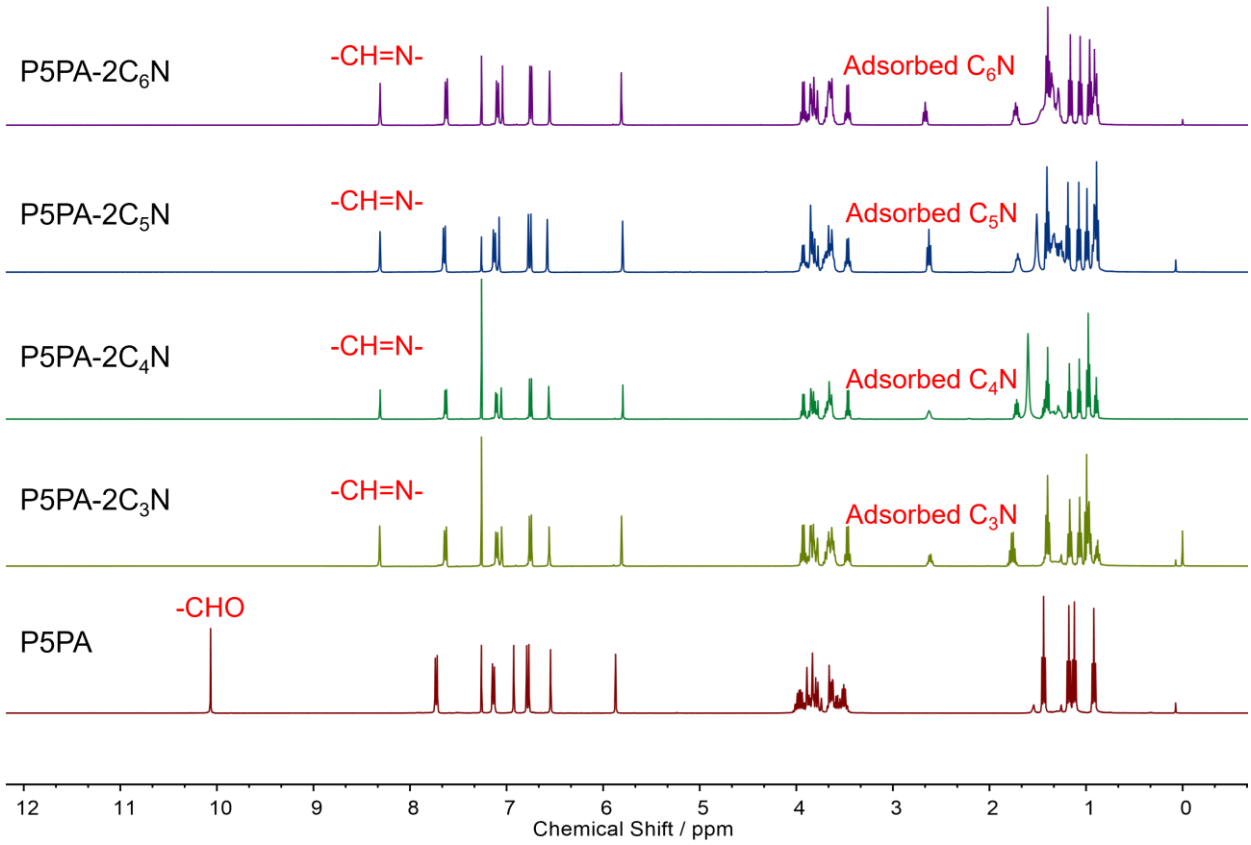

Supplementary Figure 28. Stacked ^{1}H NMR spectra (400 MHz, $CDCl_3$, 298 K) of P5PA and the corresponding solid–vapor products after exposure to C_3N, C_4N, C_5N and C_6N vapors (from bottom to top).

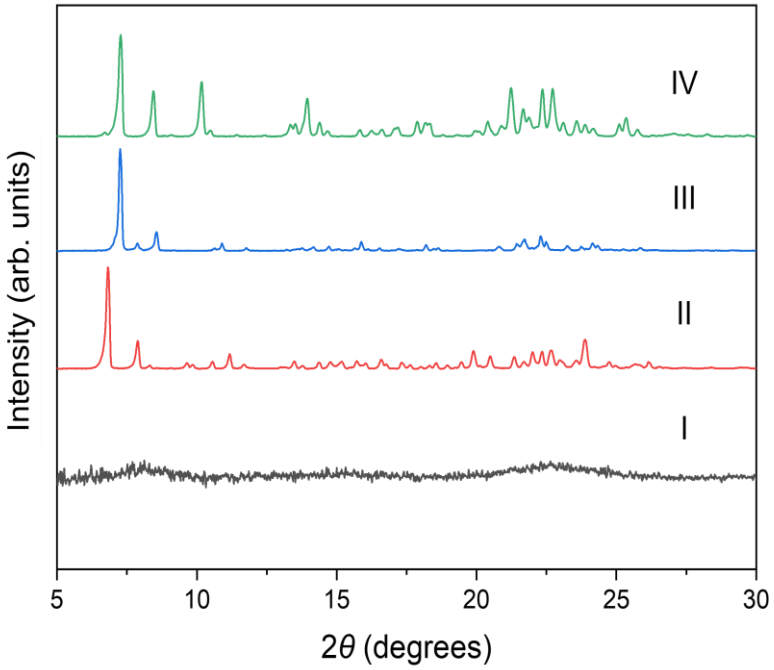

Supplementary Figure 29. PXRD patterns: (I) activated P5A; (II) P5A after exposure to C_4N vapor; (III) P5A after exposure to C_5N vapor; (IV) P5A after exposure to C_6N vapor.

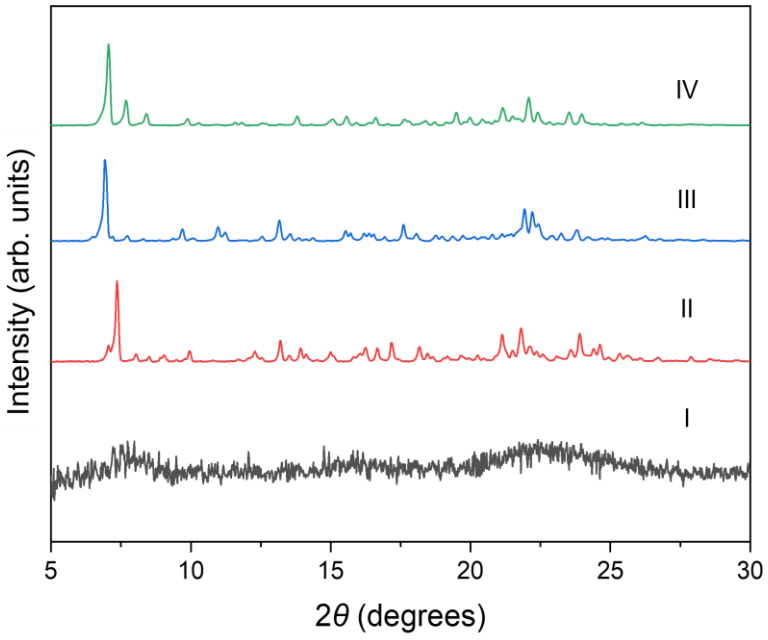

Supplementary Figure 30. PXRD patterns: (I) activated P5MA; (II) P5MA after exposure to C_4N vapor; (III) P5MA after exposure to C_5N vapor; (IV) P5MA after exposure to C_6N vapor.

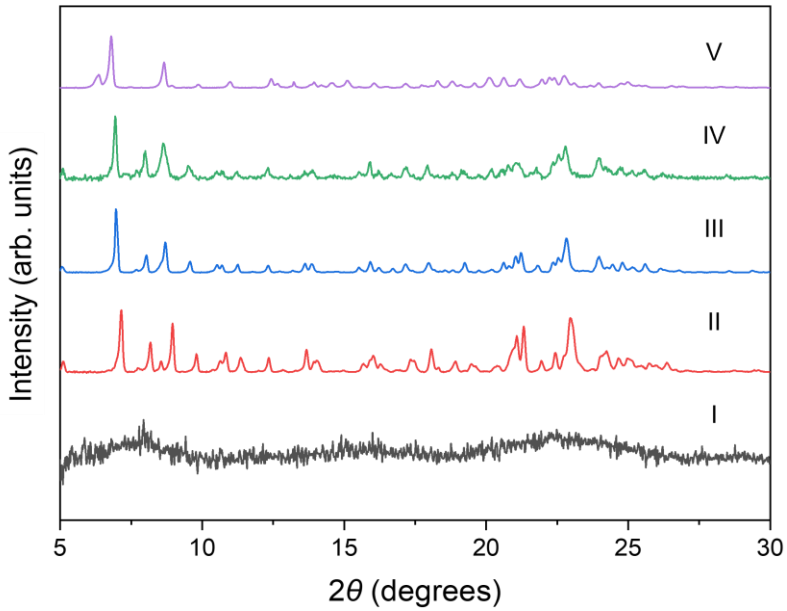

Supplementary Figure 31. PXRD patterns: (I) activated P5PA; (II) P5PA after exposure to C_3N vapor; (III) P5PA after exposure to C_4N vapor; (IV) P5PA after exposure to C_5N vapor; (V) P5PA after exposure to C_6N vapor.

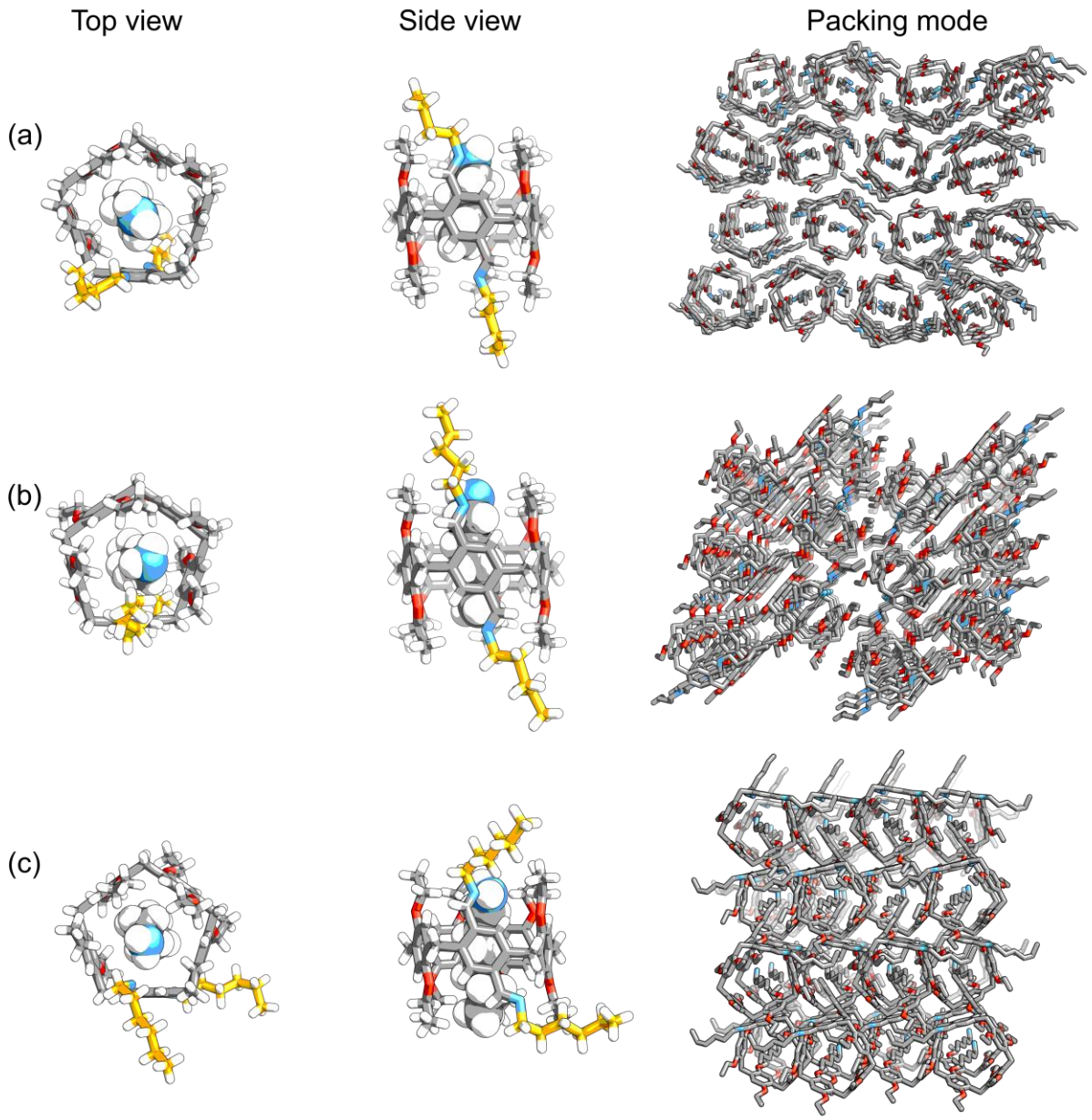

Supplementary Figure 32. SC-XRD structures of (a) C_4N@P5A-2C_4N; (b) C_5N@P5A-2C_5N; (c) C_6N@P5A-2C_6N.

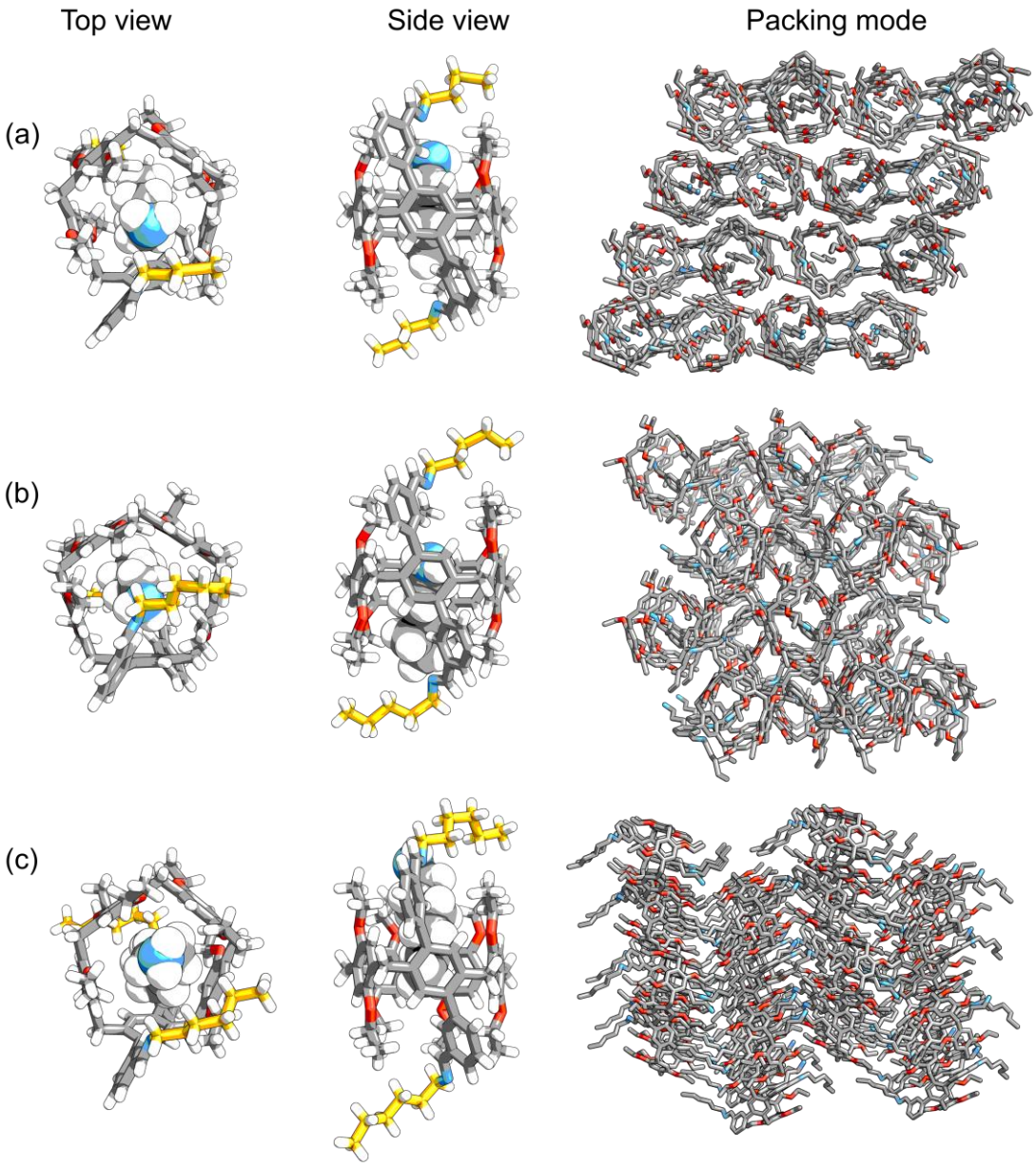

Supplementary Figure 33. SC-XRD structures of (a) C_4N@P5MA-2C_4N; (b) C_5N@P5MA-2C_5N; (c) C_6N@P5MA-2C_6N.

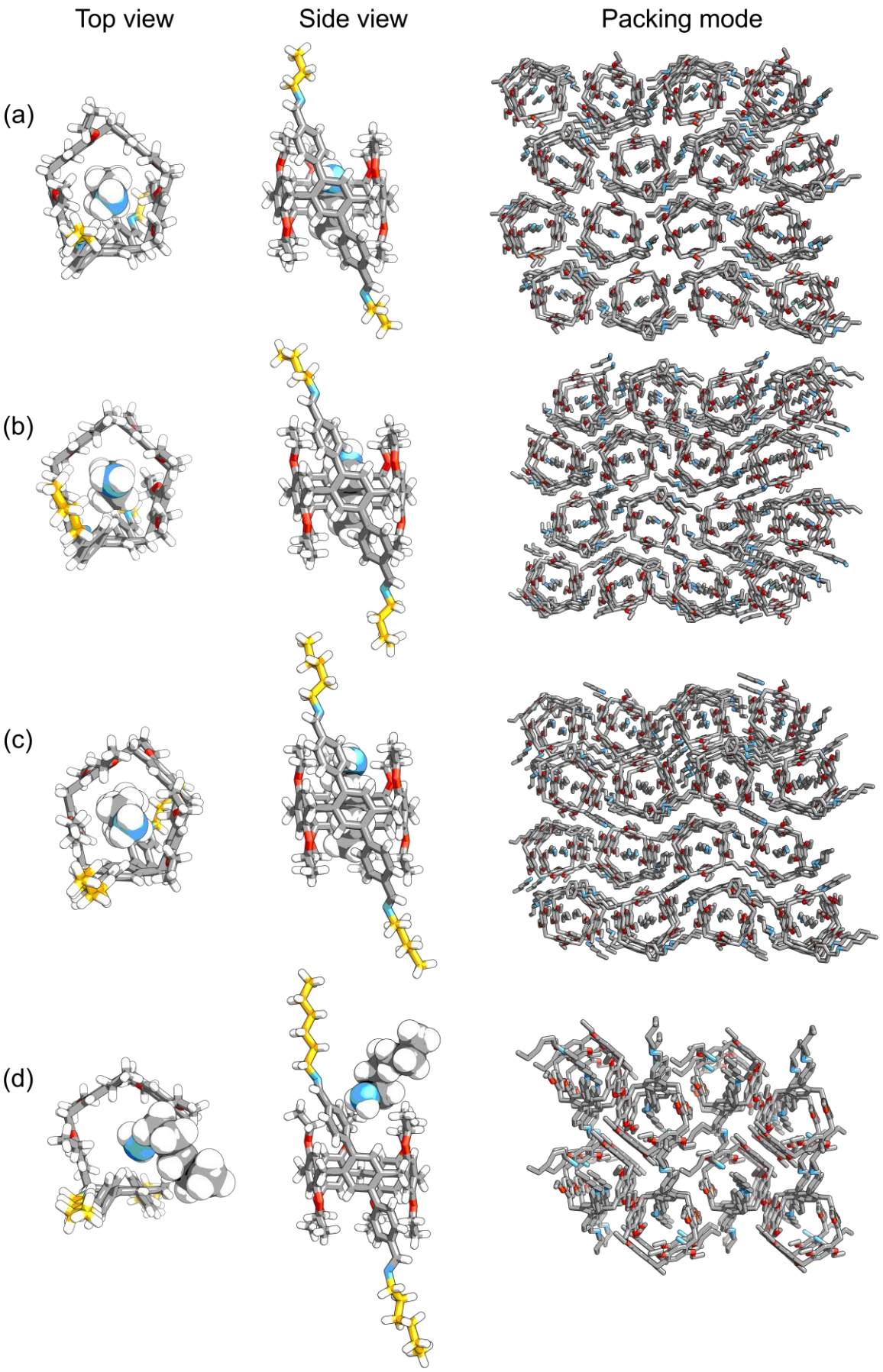

Supplementary Figure 34. SC-XRD structures of (a) C_3N@P5PA-2C_3N; (b) C_4N@P5PA-2C_4N; (c) C_5N@P5PA-2C_5N; (d) CSP-1.

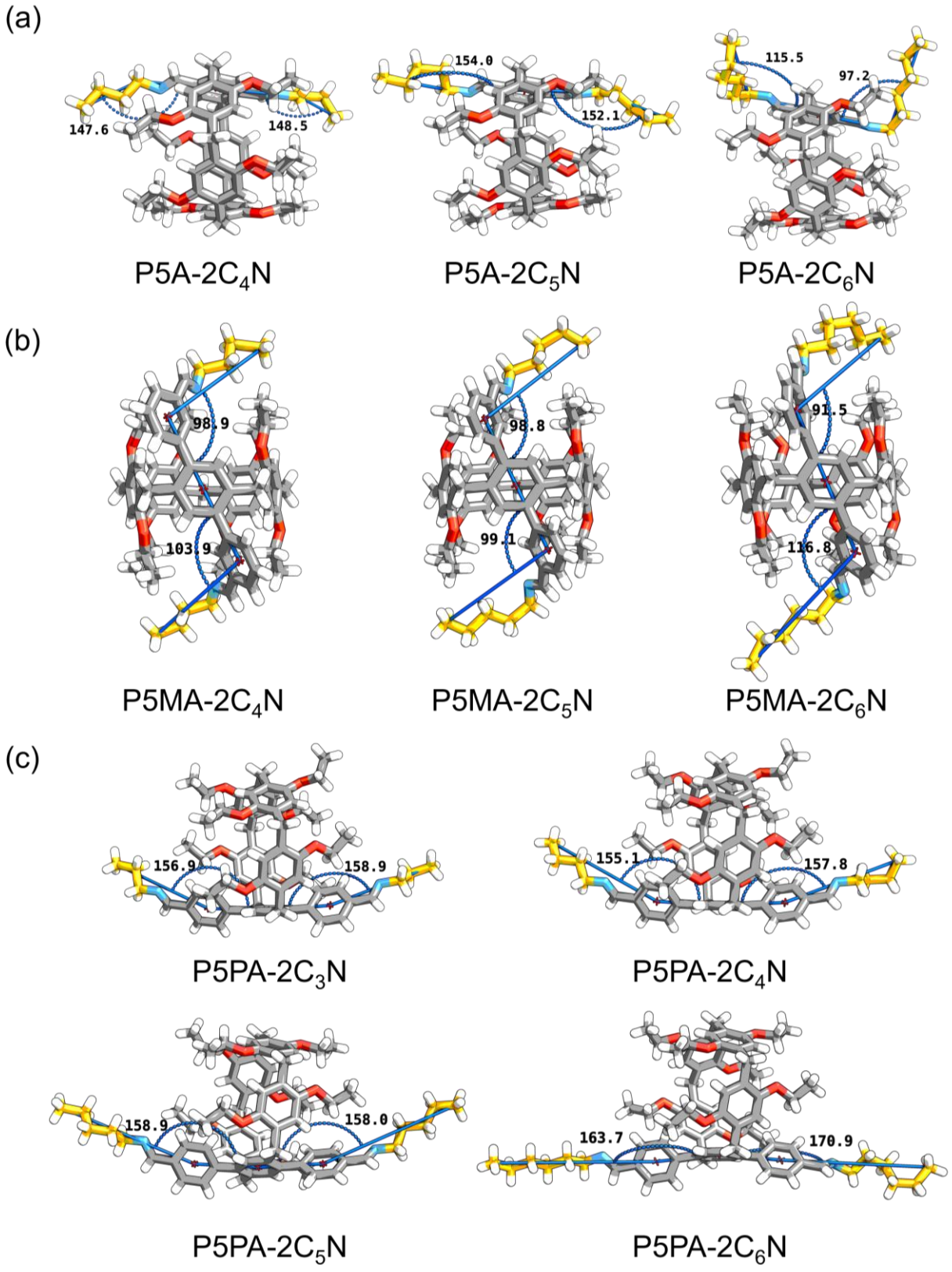

Supplementary Figure 35. Bending angles of appended *n*-alkyl chains in imine derivatives crystals synthesized from (a) P5A, (b) P5MA, and (c) P5PA, respectively.

Notes: For P5A-2C$_n$N, the bending angles of the appended chains vary with their length. The *n*-butyl chains of C$_4$N@P5A-2C$_4$N and *n*-pentyl chains of C$_5$N@P5A-2C$_5$N are oriented at approximately 150° relative to the attached benzene unit of the macrocycle, whereas the longer *n*-hexyl chains in C$_6$N@P5A-2C$_6$N are aligned nearly perpendicularly. This suggests that the shorter chains (C$_4$ and C$_5$) extend upwards, while the longer *n*-hexyl chains fit in a bent conformation. A reasonable speculation is that the increasing steric hindrance between the monomers may compel longer chains to assume a constrained rather than an outstretched conformation, despite the latter's potential for stronger interactions[13–15]. One unreacted C$_n$N molecule is encapsulated in the macrocycle cavity.

For P5MA-2C$_n$N, the length of the appended chains does not affect the overall molecular conformation. The bending angles of the appended *n*-butyl, *n*-pentyl and *n*-hexyl chains predominantly range from 90° to 117°. This phenomenon is attributed to the unfavorable positioning of the substituents in P5MA-2C$_n$N, which directs the extension orientation of the appended chains. One unreacted C$_n$N molecule is encapsulated in the macrocycle cavity.

For P5PA-2C$_n$N, the length of the appended chains does not affect the overall molecular conformation, with the bending angles of these chains falling within a tight interval of 155° to 159°. This conformational characteristic favors the threading of appended chains into adjacent cavities over any potentially accessible amine molecules. However, the shorter alkyl chains (C$_3$, C$_4$ and C$_5$) still fail to penetrate the cavities, which are occupied by amine molecules. In contrast, the longer C$_6$ chains can enter the cavities, forming the 1-D SP chain, while the C$_6$N molecules only occupy the interstitial spaces between the SP chains.

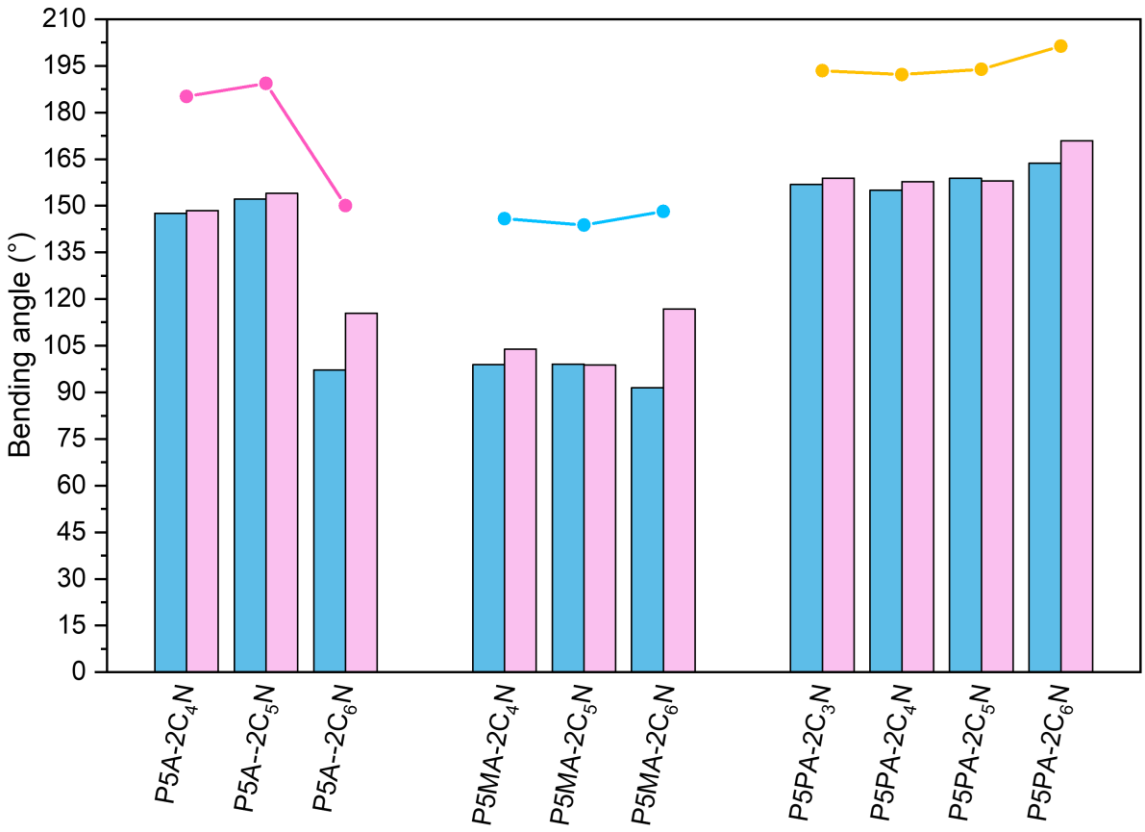

Supplementary Figure 36. Trend analysis for the bending angles of the appended *n*-alkyl chains in imine derivatives crystals synthesized from P5A, P5MA, and P5PA, respectively. The pink, blue and yellow lines represent the variations in bending angle for the P5A, P5MA and P5PA series, respectively.

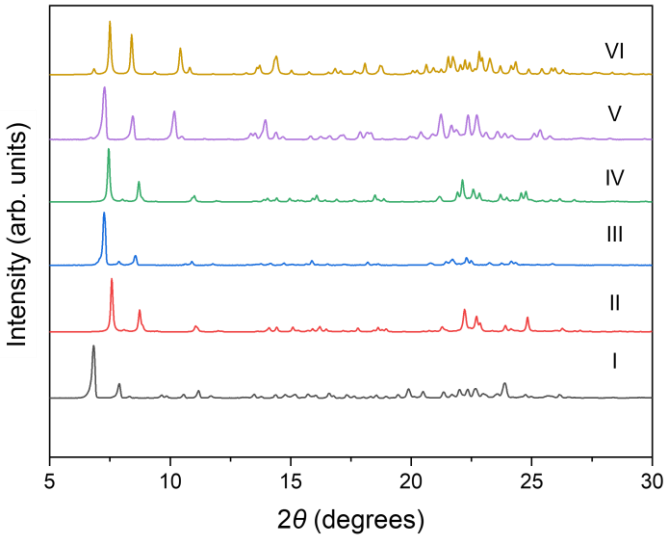

Supplementary Figure 37. PXRD patterns: (I) P5A after exposure to C_4N vapor; (II) simulated from the SC-XRD structure of C_4N@P5A-2C_4N; (III) P5A after exposure to C_5N vapor; (IV) simulated from the SC-XRD structure of C_5N@P5A-2C_5N; (V) P5A after exposure to C_6N vapor; (VI) simulated from the SC-XRD structure of C_6N@P5A-2C_6N. The slight peak shifts observed in the PXRD patterns of the vapor-treated powders (I, III, and V), relative to the simulated patterns from SC-XRD structures, can be attributed to slight variations in the unit cell volume.

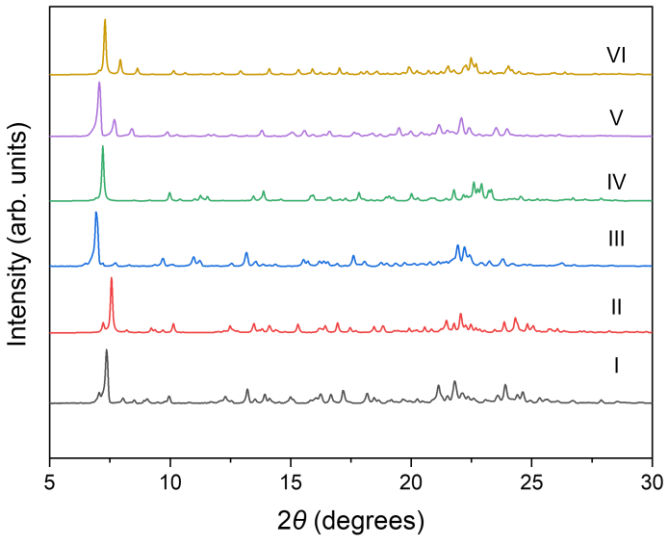

Supplementary Figure 38. PXRD patterns: (I) P5MA after exposure to C_4N vapor; (II) simulated from the SC-XRD structure of C_4N@P5MA-2C_4N; (III) P5MA after exposure to C_5N vapor; (IV) simulated from the SC-XRD structure of C_5N@P5MA-2C_5N; (V) P5MA after exposure to C_6N vapor; (VI) simulated from the SC-XRD structure of C_6N@P5MA-2C_6N.

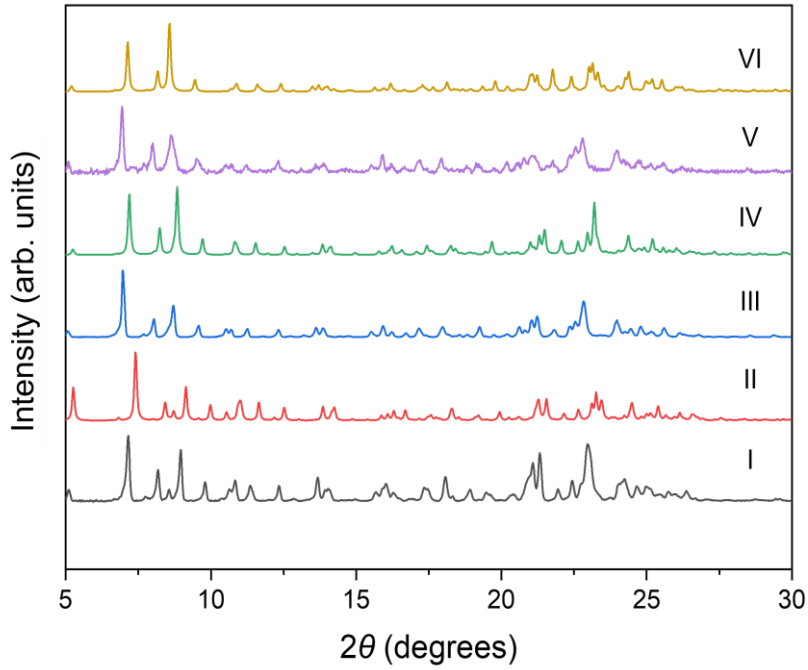

Supplementary Figure 39. PXRD patterns: (I) P5PA after exposure to C_3N vapor; (II) simulated from the SC-XRD structure of C_3N@P5PA-2C_3N; (III) P5PA after exposure to C_4N vapor; (IV) simulated from the SC-XRD structure of C_4N@P5PA-2C_4N; (V) P5PA after exposure to C_5N vapor; (VI) simulated from the SC-XRD structure of C_5N@P5PA-2C_5N.

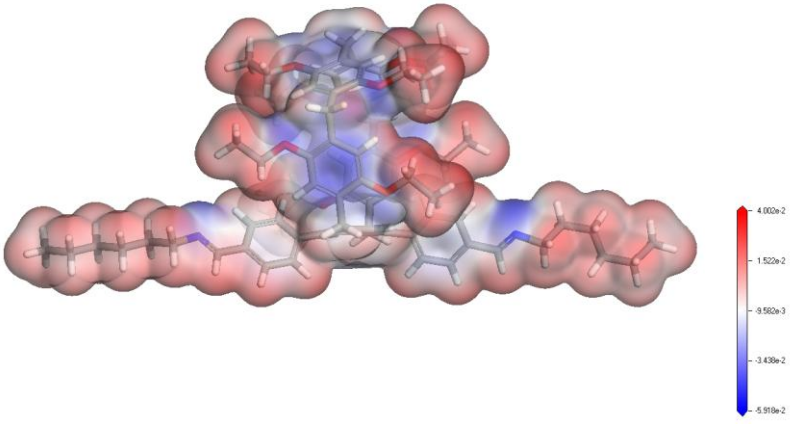

Supplementary Figure 40. The electrostatic potential map of P5PA-2C_6N.

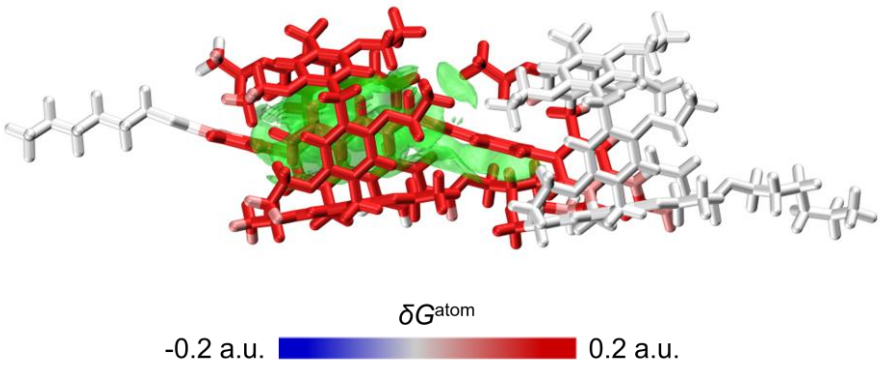

Supplementary Figure 41. Distribution of noncovalent interaction regions in CSP-1 investigated by IGMH. The red-colored regions highlight the parts of P5PA-2C_6N that contribute most significantly to the overall interactions.

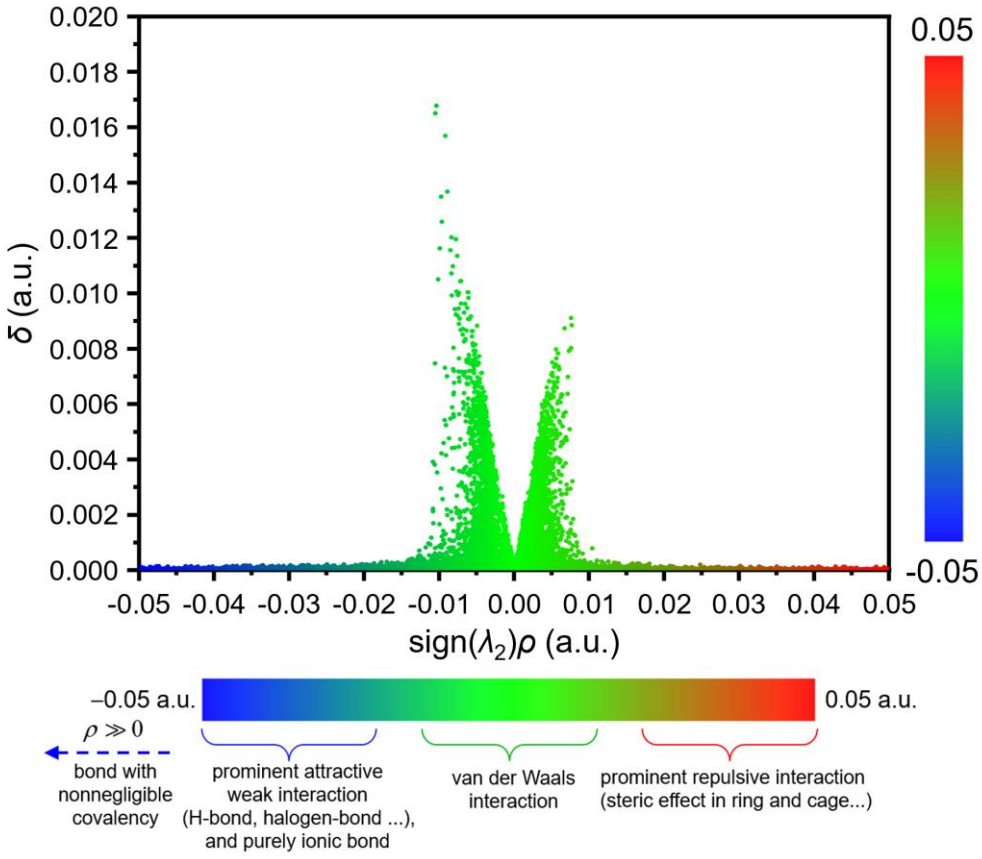

Supplementary Figure 42. IGMH scatter plot for noncovalent interactions in CSP-1.

Supplementary Table 2. Atomic *ΔG* indices and percentage contributions of the threading *n*-hexyl chain in CSP-1.

Atom Index	Element	*ΔG* Value	% Contribution
67	C	0.267011	5.09 %
119	C	0.261973	5.00 %
62	C	0.257522	4.91 %
31	C	0.242326	4.62 %
136	C	0.226598	4.32 %
58	C	0.191080	3.65 %
69	H	0.248104	4.73 %
68	H	0.243150	4.64 %
120	H	0.232855	4.44 %
63	H	0.229501	4.38 %
64	H	0.227332	4.34 %
121	H	0.222663	4.25 %
33	H	0.207398	3.96 %
32	H	0.201098	3.84 %
137	H	0.179458	3.42 %
138	H	0.165158	3.15 %
60	H	0.149215	2.85 %
139	H	0.125517	2.39 %
59	H	0.147351	2.81 %

The total contribution of all atoms on the threading *n*-hexyl chain is 76.79 %.

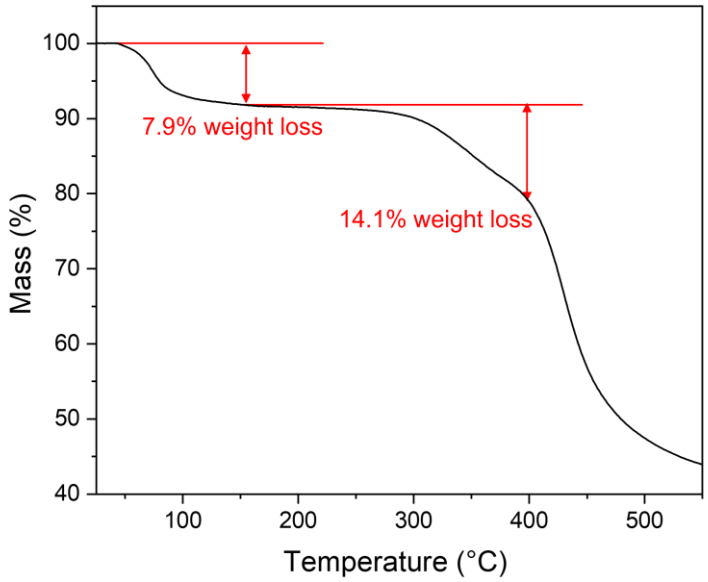

Supplementary Figure 43. TGA curve of as-synthesized CSP-1.

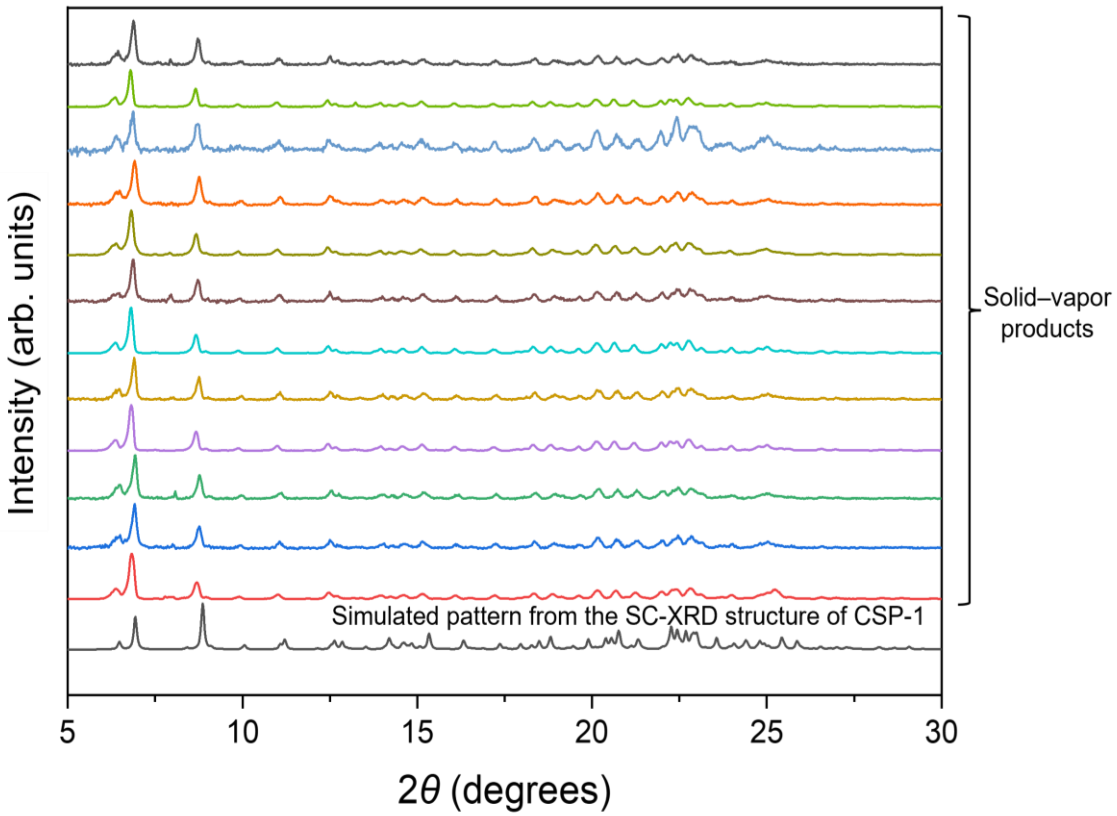

Supplementary Figure 44. PXRD pattern of P5PA after exposure to C_6N vapor (12 trials) and the simulated pattern from the SC-XRD structure of CSP-1.

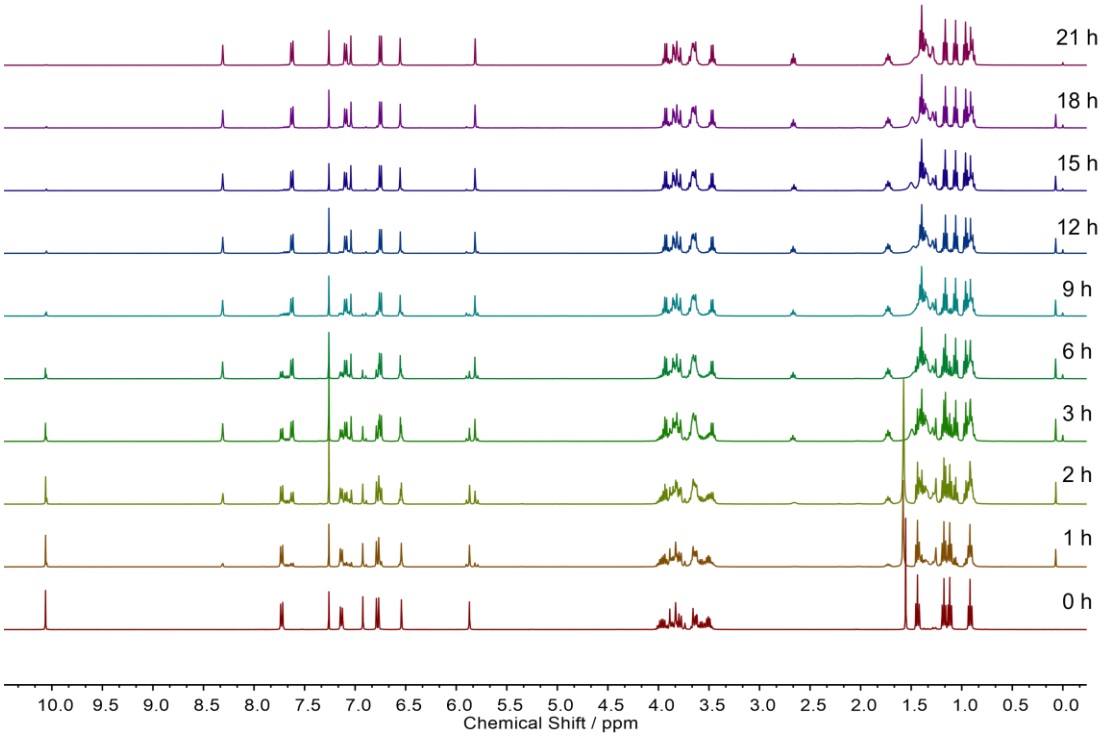

Supplementary Figure 45. Time-dependent ^{1}H NMR spectra (400 MHz, $CDCl_3$, 293 K) of P5PA after exposure to C_6N vapor.

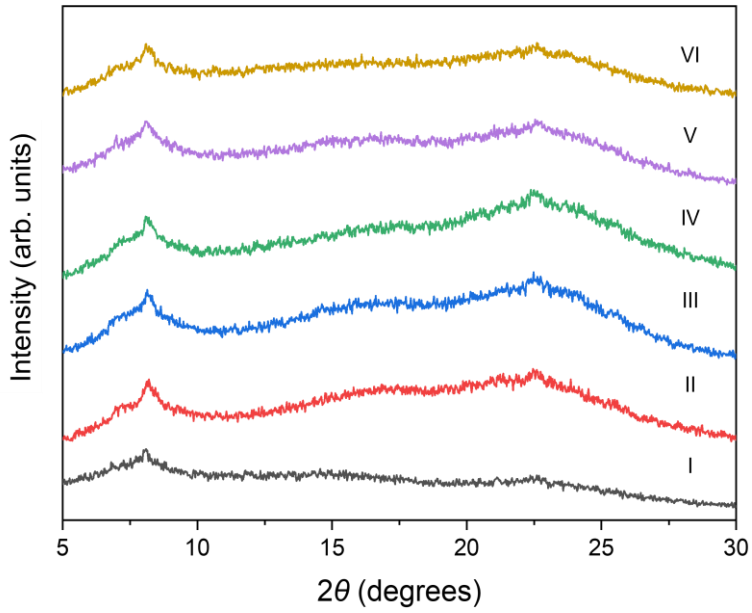

Supplementary Figure 46. PXRD patterns: (I) activated P5PA; (II) powders of I after exposure to aniline vapor for 1 hour; (III) powders of I after exposure to aniline vapor for 2 hours; (IV) powders of I after exposure to aniline vapor for 4 hours; (V) powders of I after exposure to aniline vapor for 6 hours; (VI) powders of I after exposure to aniline vapor for 8 hours.

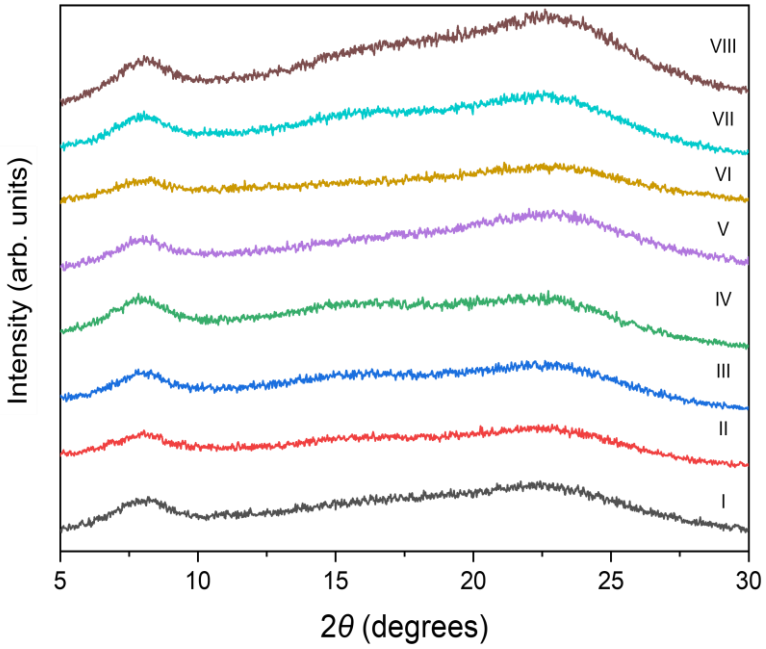

Supplementary Figure 47. PXRD patterns: (I) activated P5MA; (II) powders of I after exposure to aniline vapor for 1 hour; (III) powders of I after exposure to aniline vapor for 2 hours; (IV) powders of I after exposure to aniline vapor for 3 hours; (V) powders of I after exposure to aniline vapor for 4 hours; (VI) powders of I after exposure to aniline vapor for 5 hours; (VII) powders of I after exposure to aniline vapor for 6 hours; (VIII) powders of I after exposure to aniline vapor for 7 hours.

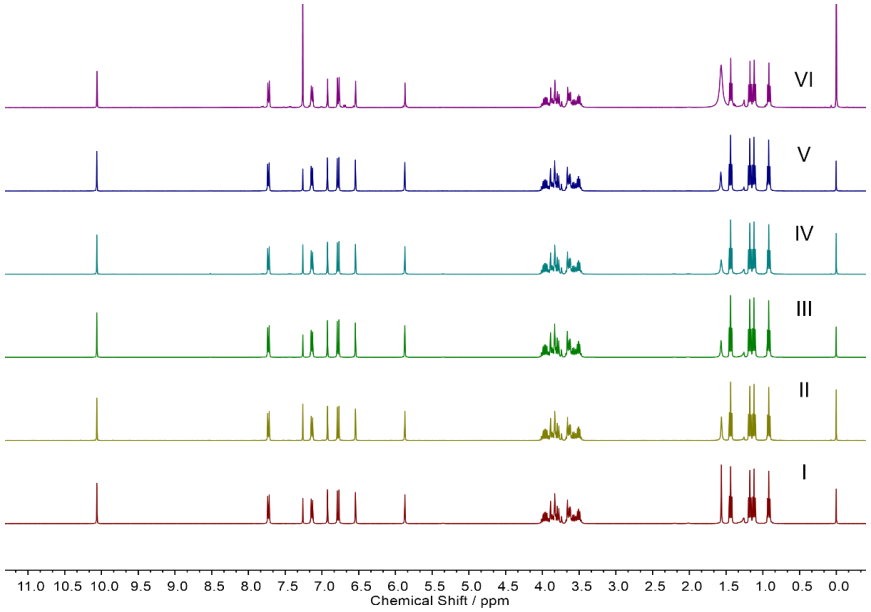

Supplementary Figure 48. ^{1}H NMR profile: (I) activated P5PA; (II) powders of I after exposure to aniline vapor for 1 hour; (III) powders of I after exposure to aniline vapor for 2 hours; (IV) powders of I after exposure to aniline vapor for 4 hours; (V) powders of I after exposure to aniline vapor for 6 hours; (VI) powders of I after exposure to aniline vapor for 8 hours.

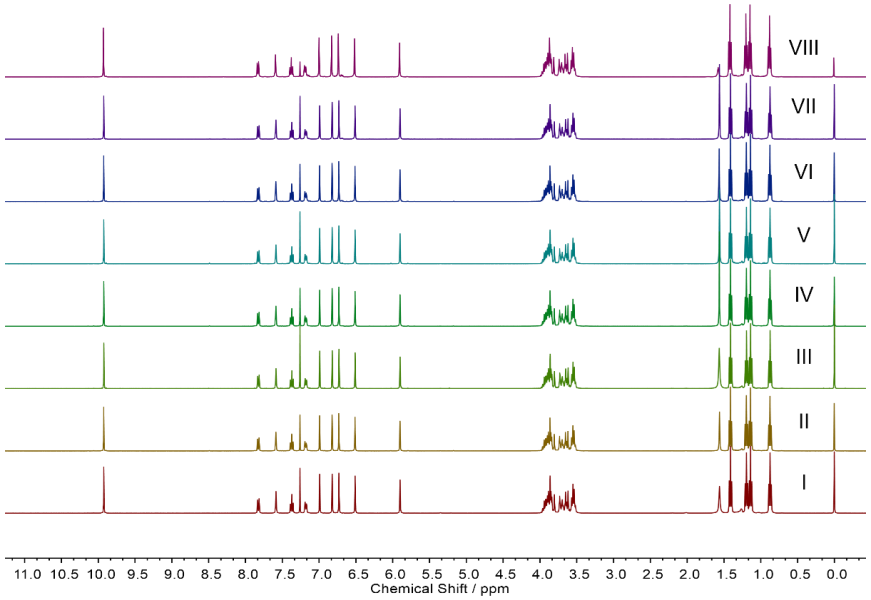

Supplementary Figure 49. ^{1}H NMR profile: (I) activated P5MA; (II) powders of I after exposure to aniline vapor for 1 hour; (III) powders of I after exposure to aniline vapor for 2 hours; (IV) powders of I after exposure to aniline vapor for 3 hours; (V) powders of I after exposure to aniline vapor for 4 hours; (VI) powders of I after exposure to aniline vapor for 5 hours; (VII) powders of I after exposure to aniline vapor for 6 hours; (VIII) powders of I after exposure to aniline vapor for 7 hours.

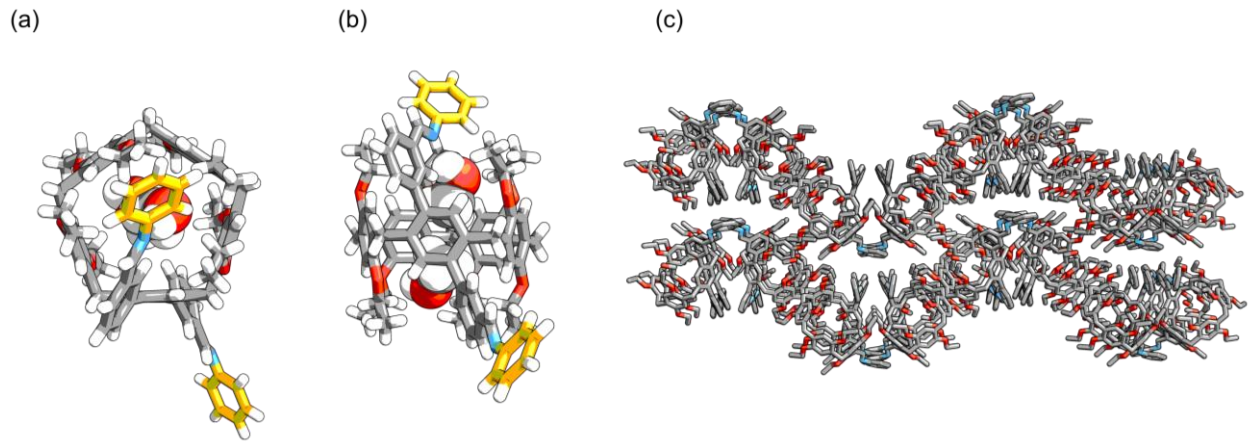

Supplementary Figure 50. SC-XRD structure of MeOH@P5MA-2Aniline: (a) top view; (b) side view; (c) packing mode. The above single crystal was obtained by dissolving P5MA in MeOH/aniline mixed solvent, indicating that the imine product was formed in the solution phase. This result is completely different from that observed in the solid state. Additionally, only MeOH molecules were incorporated as guests into the crystal lattice, with aniline not being included.

Notes: The solid–vapor synthesis is not universally applicable to all amine vapors. For example, upon exposure to aniline vapor, the precursors remain amorphous (Supplementary Figs. 46 and 47). No physically adsorbed aniline molecules were detected in the powders, let alone any imine condensation reactions (Supplementary Figs. 48 and 49).

However, in contrast to the solid–vapor case, imine condensation occurs in solution to afford an aniline-appended P5PA derivative. Meanwhile, bulky unreacted aniline is not observed within the corresponding crystal lattice (Supplementary Fig. 50). This result reveals the distinct behavior of the solid–vapor reaction from the solution-phase reaction, the former of which shows reactant size selectivity. In other words, bulky amine vapors that cannot be physically adsorbed are unable to induce the reaction or crystallization.

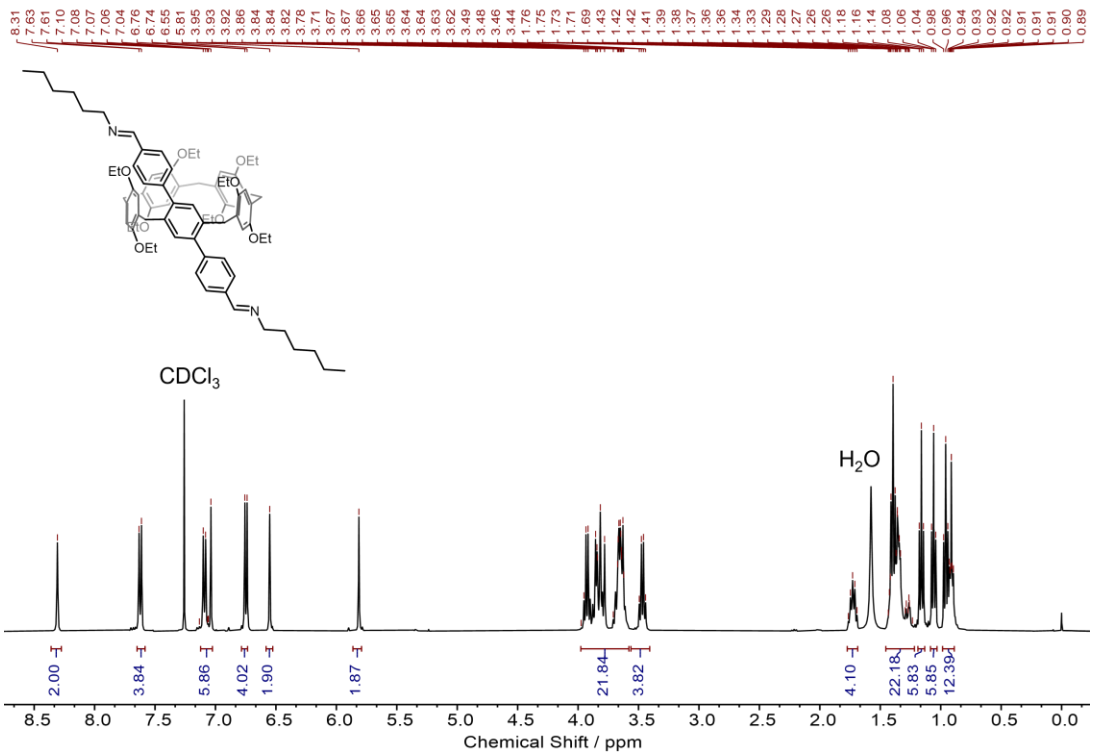

Supplementary Figure 51. ^{1}H NMR spectrum (400 MHz, $CDCl_3$, 298 K) of the solvent-free CSP-1.

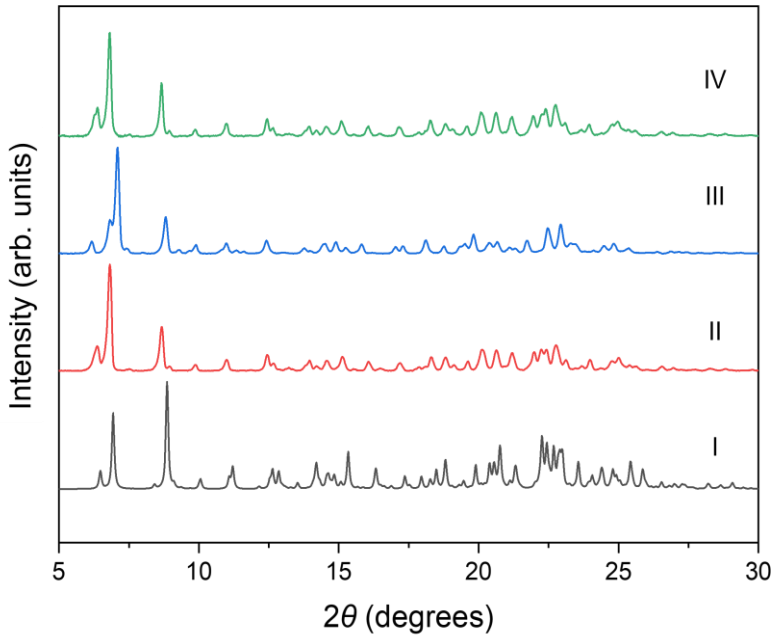

Supplementary Figure 52. PXRD patterns: (I) simulated from the SC-XRD structure of CSP-1; (II) as-synthesized CSP-1; (III) solvent-free CSP-1 (obtained by drying as-synthesized CSP-1 at 100 °C *in vacuo* overnight); (IV) crystals of III after exposure to C_6N vapor.

4. Investigation of CSP-1 in solution

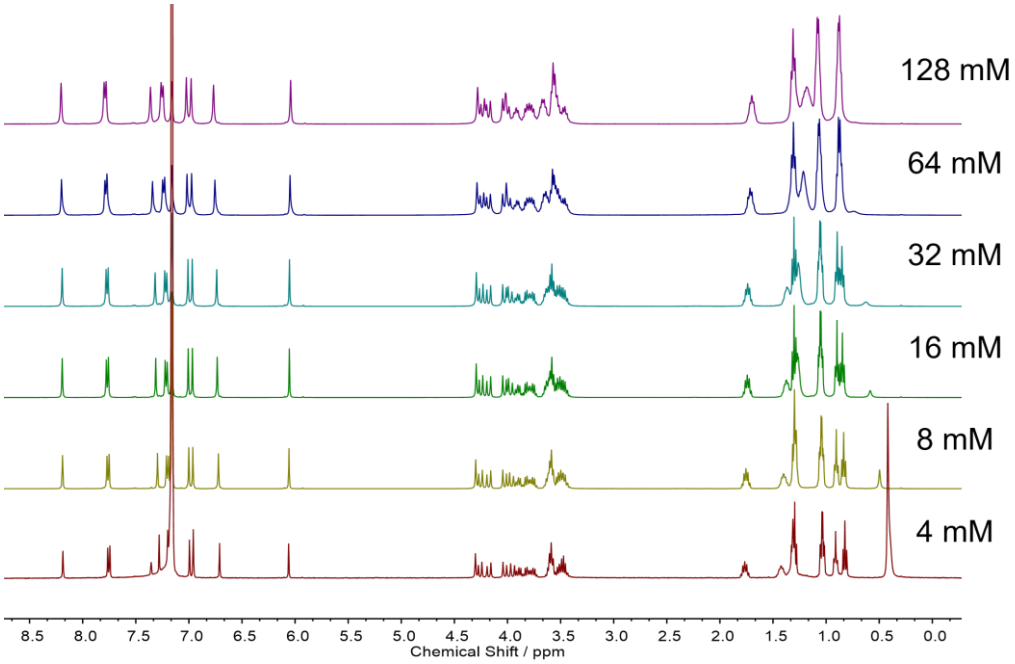

Supplementary Figure 53. ^{1}H NMR spectra (400 MHz, C_6D_6, 293 K) of the solvent-free CSP-1 at different P5PA-2C_6N concentrations, ranging from 4 mM to 128 mM.

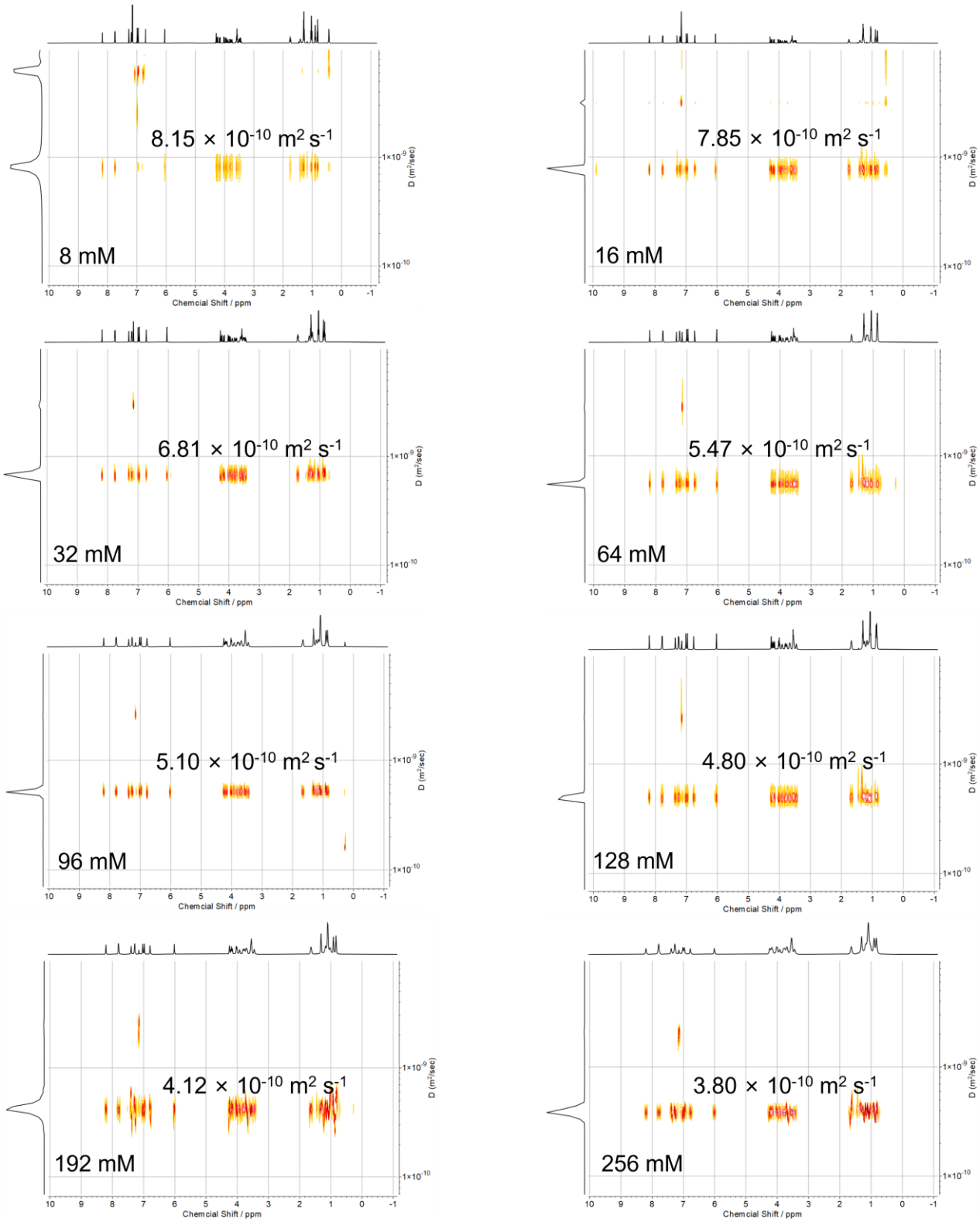

Supplementary Figure 54. DOSY spectra (600 MHz, C_6D_6, 293 K) of the solvent-free CSP-1 at different P5PA-2C_6N concentrations. The corresponding diffusion coefficients are labeled in each spectrum.

Supplementary Table 3. The average hydrodynamic diameter of aggregated assemblies at different P5PA-2C_6N concentrations determined from DLS measurements.

Concentration	Hydrodynamic diameter
18 mM	307.14 nm
24 mM	374.28 nm
32 mM	453.79 nm
36 mM	529.30 nm
48 mM	631.31 nm
72 mM	863.66 nm
96 mM	1099.94 nm

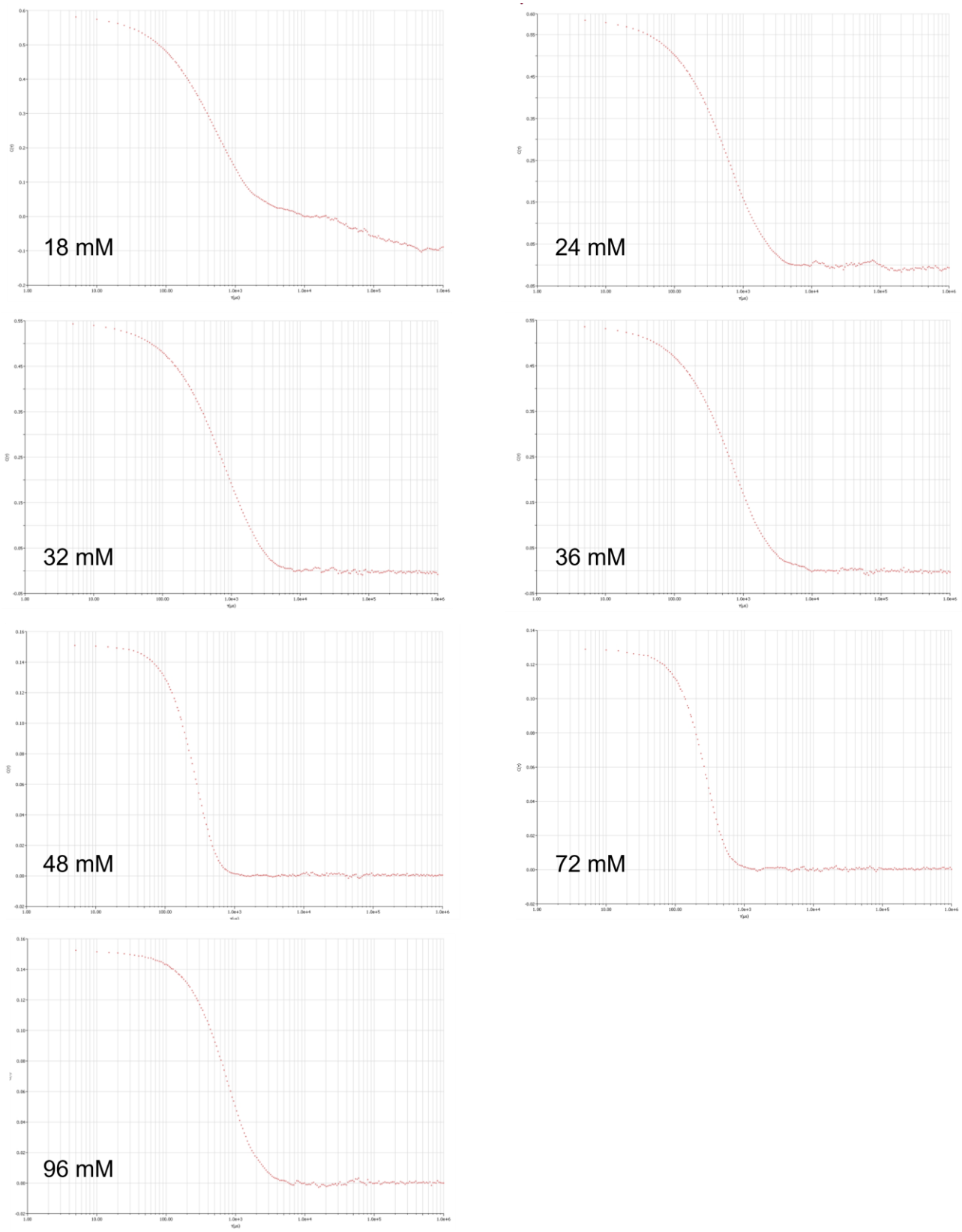

Supplementary Figure 55. Selected electric field autocorrelation functions $g_1(\tau)$ obtained from DLS measurements at different P5PA-2C_6N concentrations. The red dots represent experimental data.

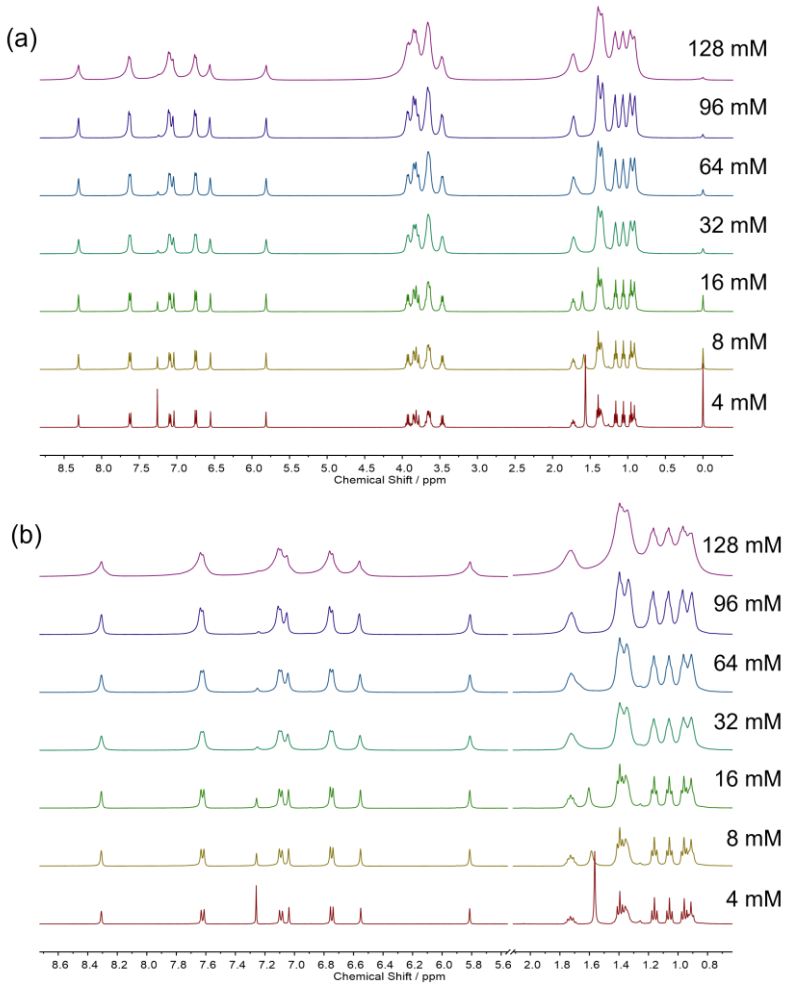

Supplementary Figure 56. (a) ^{1}H NMR spectra (400 MHz, $CDCl_3$, 293 K) of the solvent-free CSP-1 at different P5PA-2C_6N concentrations, ranging from 4 mM to 128 mM. (b) Partial ^{1}H NMR spectra (400 MHz, $CDCl_3$, 293 K) from (a). As the concentration increased, peak broadening due to high concentration occurred, but no apparent chemical shift changes were observed.

5. Transformation of CSP-1 induced by imine exchange

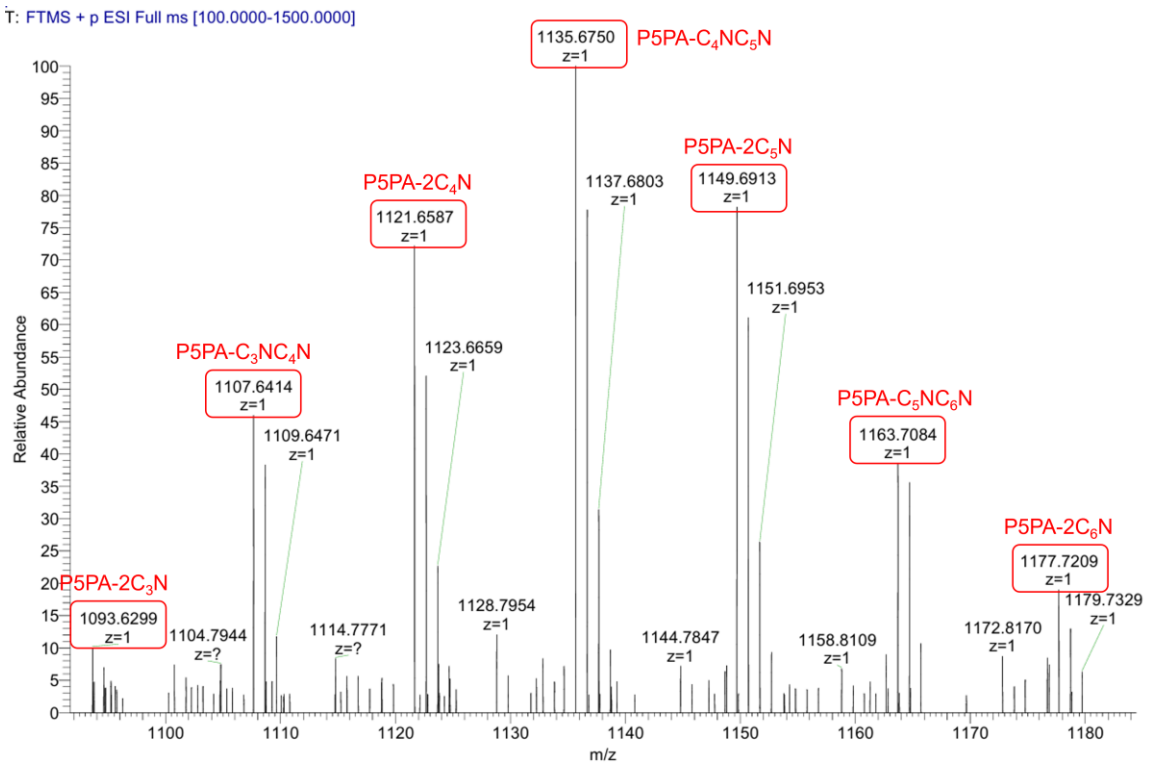

Supplementary Figure 57. HR-MS spectrum of P5PA after exposure to the vapor of mixed aliphatic amines (C_3N:C_4N:C_5N:C_6N = 1:1:1:1). After treating activated P5PA with the mixed amine vapor overnight, a mixture of imine products was obtained with no discernible selectivity. This result indicates that the solid–vapor reaction exhibits comparable reactivity towards aliphatic amines of different chain lengths.

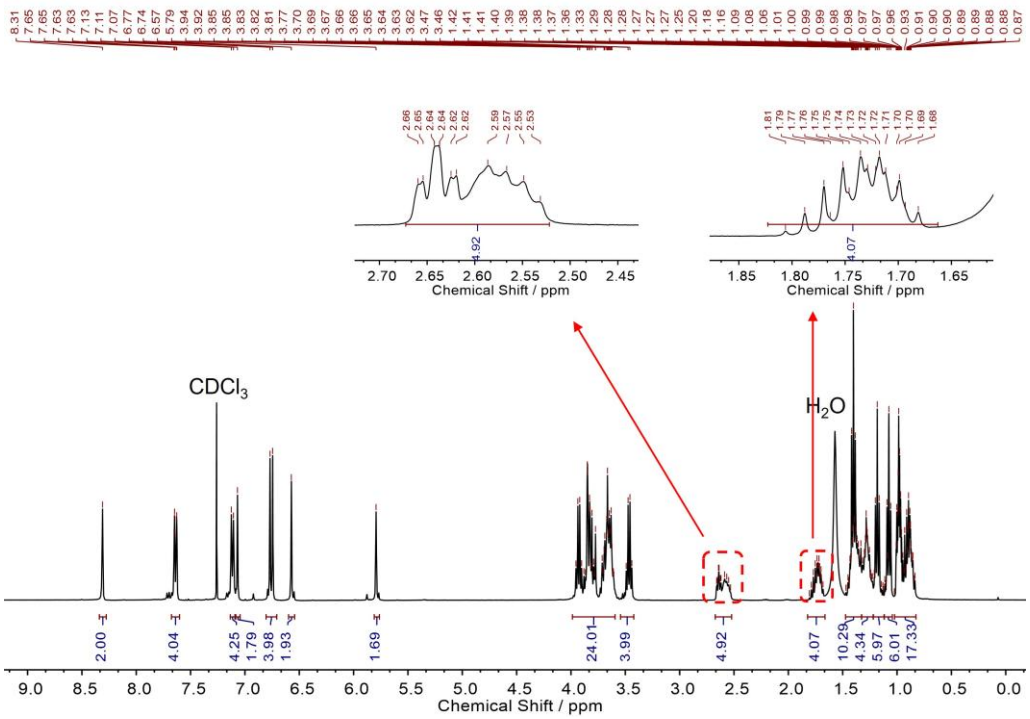

Supplementary Figure 58. ^{1}H NMR spectrum (400 MHz, $CDCl_3$, 298 K) of P5PA after exposure to the vapor of mixed aliphatic amines (C_3N:C_4N:C_5N:C_6N = 1:1:1:1). The overlapping signals in the enlarged regions indicate that more than one aliphatic amine was adsorbed under this condition, and the imine products obtained were mixtures.

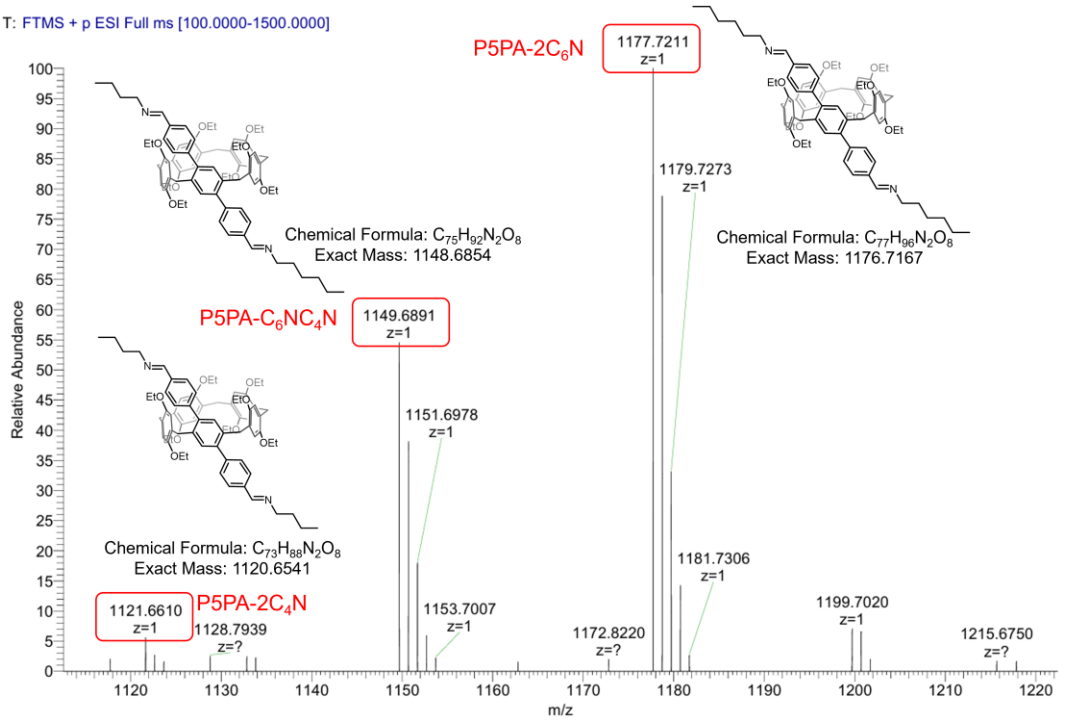

Supplementary Figure 59. HR-MS spectrum of as-synthesized CSP-1 after exposure to C_4N vapor for 1 hour.

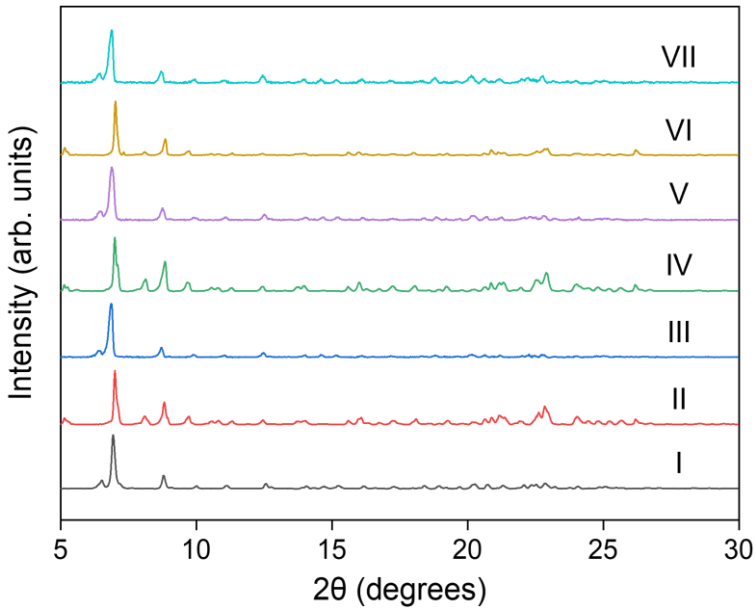

Supplementary Figure 60. Reversible transformations between CSP-1 and C_4N@P5PA-2C_4N over three vapor-treatment cycles: (I) experimental CSP-1; (II) crystals of I after exposure to C_4N vapor for 12 hours; (III) crystals of II after exposure to C_6N vapor for 24 hours; (IV) crystals of III after exposure to C_4N vapor for 12 hours; (V) crystals of IV after exposure to C_6N vapor for 24 hours; (VI) crystals of V after exposure to C_4N vapor for 12 hours; (VII) crystals of VI after exposure to C_6N vapor for 24 hours.

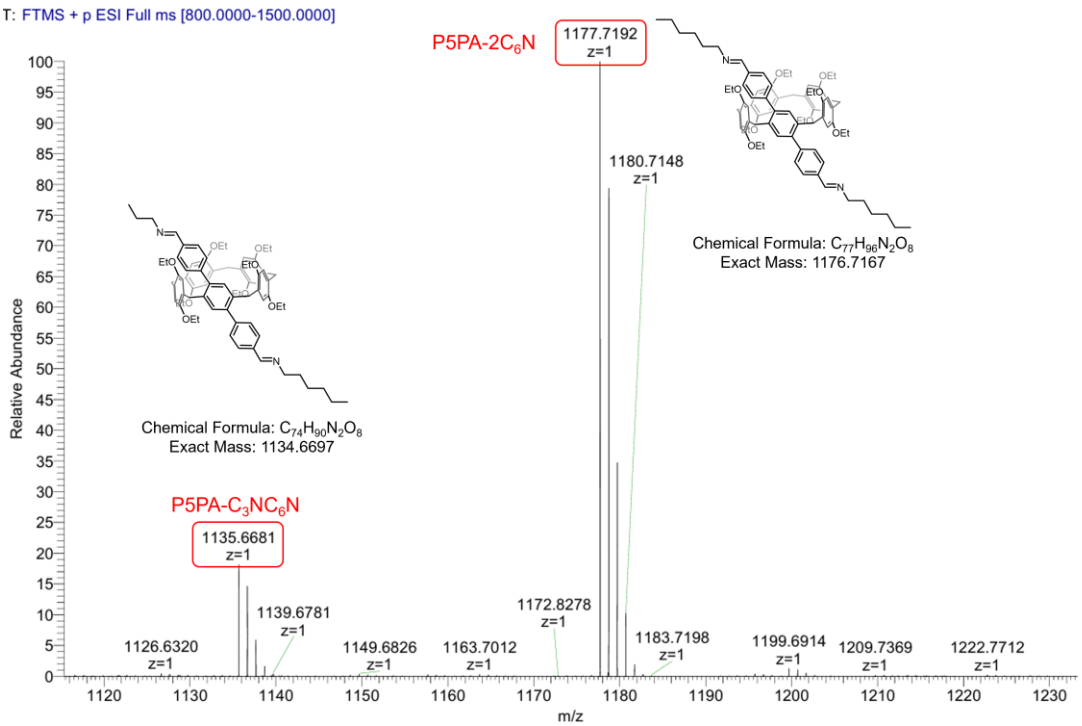

Supplementary Figure 61. HR-MS spectrum of as-synthesized CSP-1 after exposure to C_3N vapor for 30 minutes.

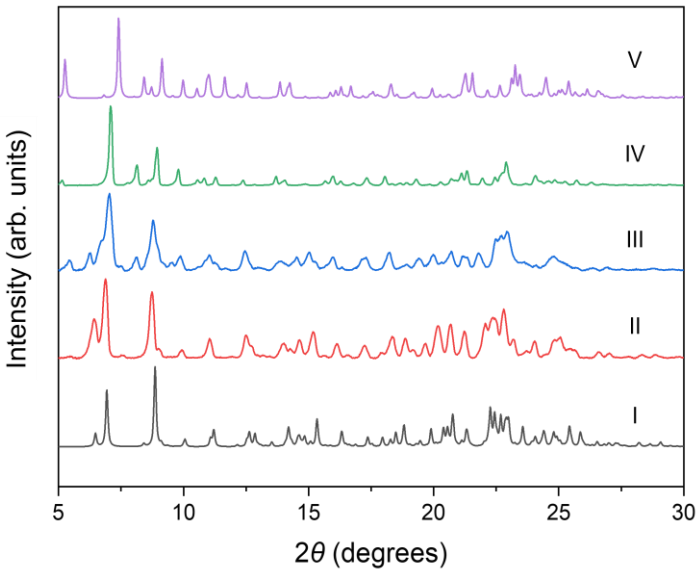

Supplementary Figure 62. PXRD patterns: (I) simulated from the SC-XRD structure of CSP-1; (II) as-synthesized CSP-1; (III) crystals of II after exposure to C_3N vapor for 2 hours; (IV) crystals of II after exposure to C_3N vapor for 4 hours; (V) simulated from the SC-XRD structure of C_3N@P5PA-2C_3N.

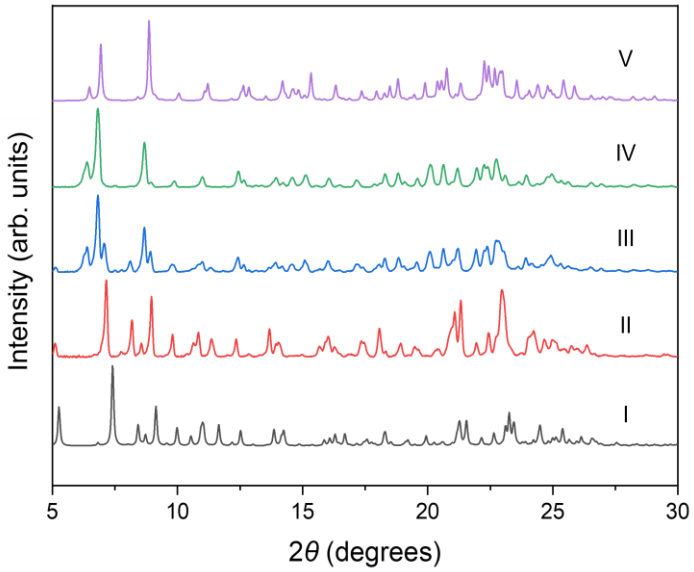

Supplementary Figure 63. PXRD patterns: (I) simulated from the SC-XRD structure of C_3N@P5PA-2C_3N; (II) experimental C_3N@P5PA-2C_3N; (III) crystals of II after exposure to C_6N vapor for 12 hours; (IV) crystals of II after exposure to C_6N vapor for 24 hours; (V) simulated from the SC-XRD structure of CSP-1.

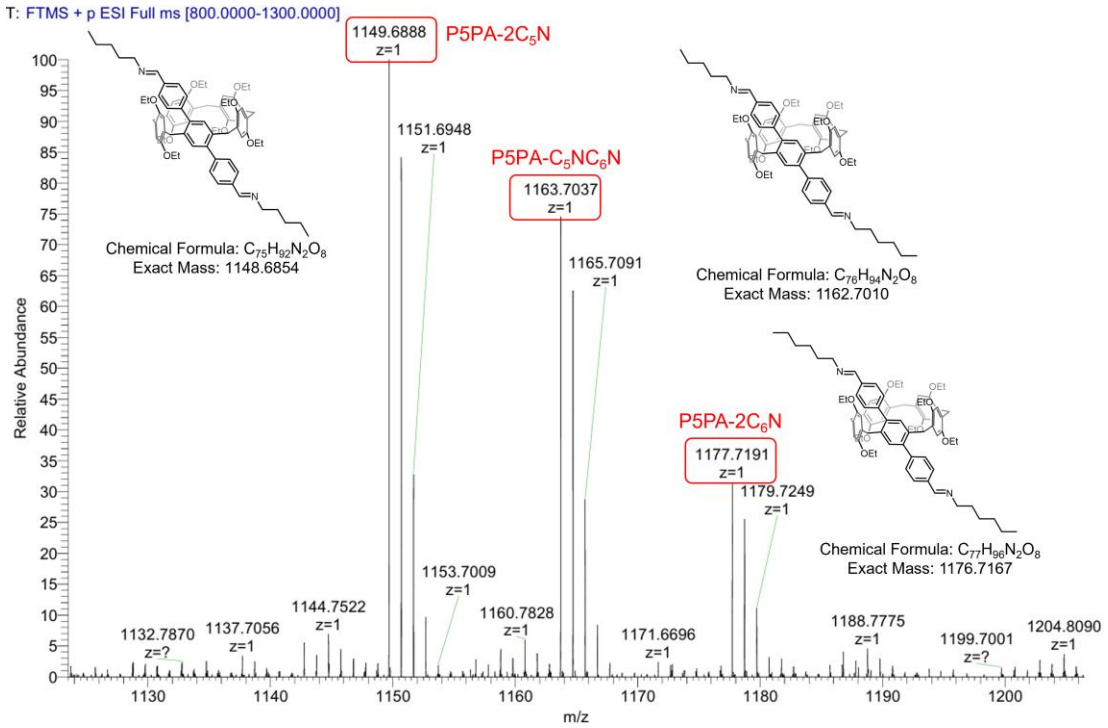

Supplementary Figure 64. HR-MS spectrum of as-synthesized CSP-1 after exposure to C_5N vapor for 6 hours.

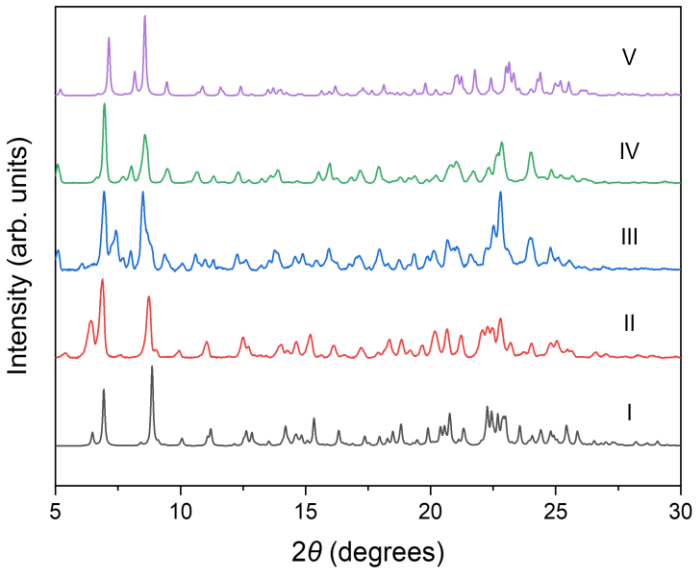

Supplementary Figure 65. PXRD patterns: (I) simulated from the SC-XRD structure of CSP-1; (II) as-synthesized CSP-1; (III) crystals of II after exposure to C_5N vapor for 24 hours; (IV) crystals of II after exposure to C_5N vapor for 48 hours; (V) simulated from the SC-XRD structure of C_5N@P5PA-2C_5N.

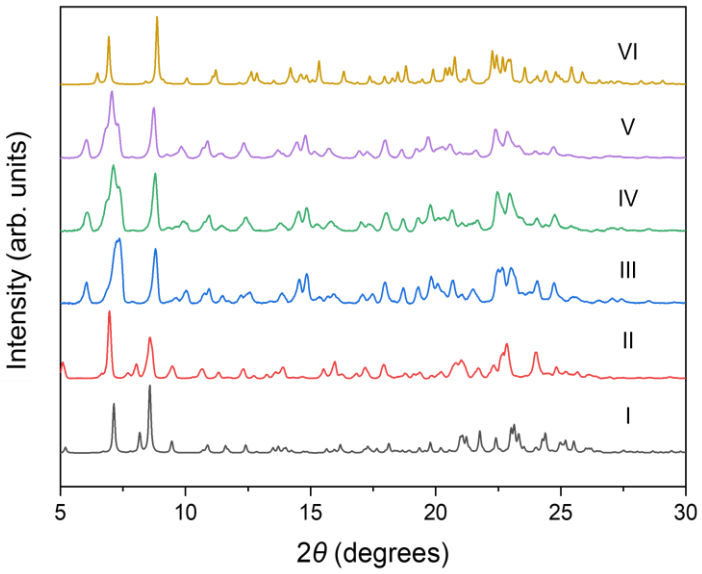

Supplementary Figure 66. PXRD patterns: (I) simulated from the SC-XRD structure of C_5N@P5PA-2C_5N; (II) experimental C_5N@P5PA-2C_5N; (III) crystals of II after exposure to C_6N vapor for 24 hours; (IV) crystals of II after exposure to C_6N vapor for 48 hours; (V) crystals of II after exposure to C_6N vapor for 72 hours; (VI) simulated from the SC-XRD structure of CSP-1.

6. Transformation of CSP-1 induced by competitive guest insertion

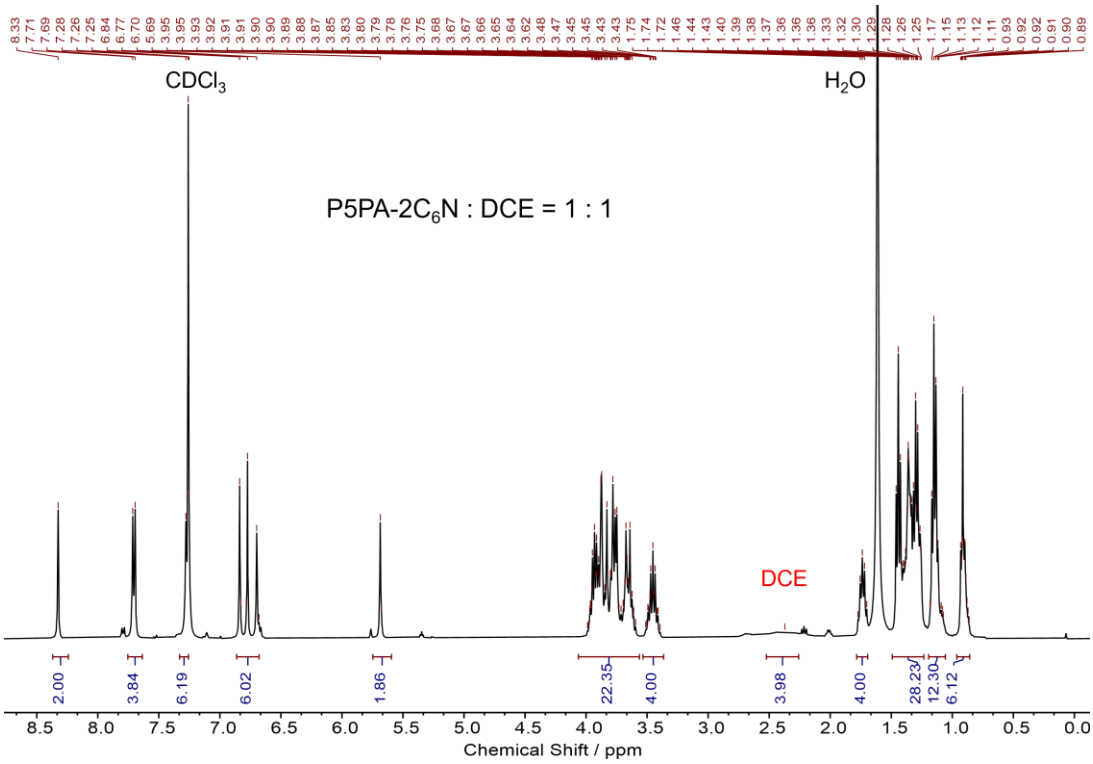

Supplementary Figure 67. ^{1}H NMR spectrum (400 MHz, $CDCl_3$, 298 K) of as-synthesized CSP-1 after exposure to DCE vapor for 12 hours.

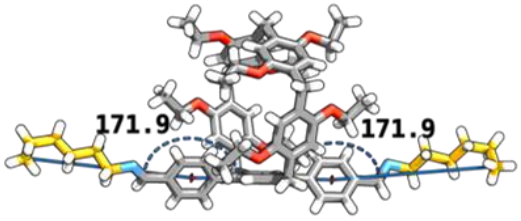

Supplementary Figure 68. The bending angles of appended *n*-hexyl chains of P5PA-2C_6N in the SC-XRD structure of DCE@P5PA-2C_6N.

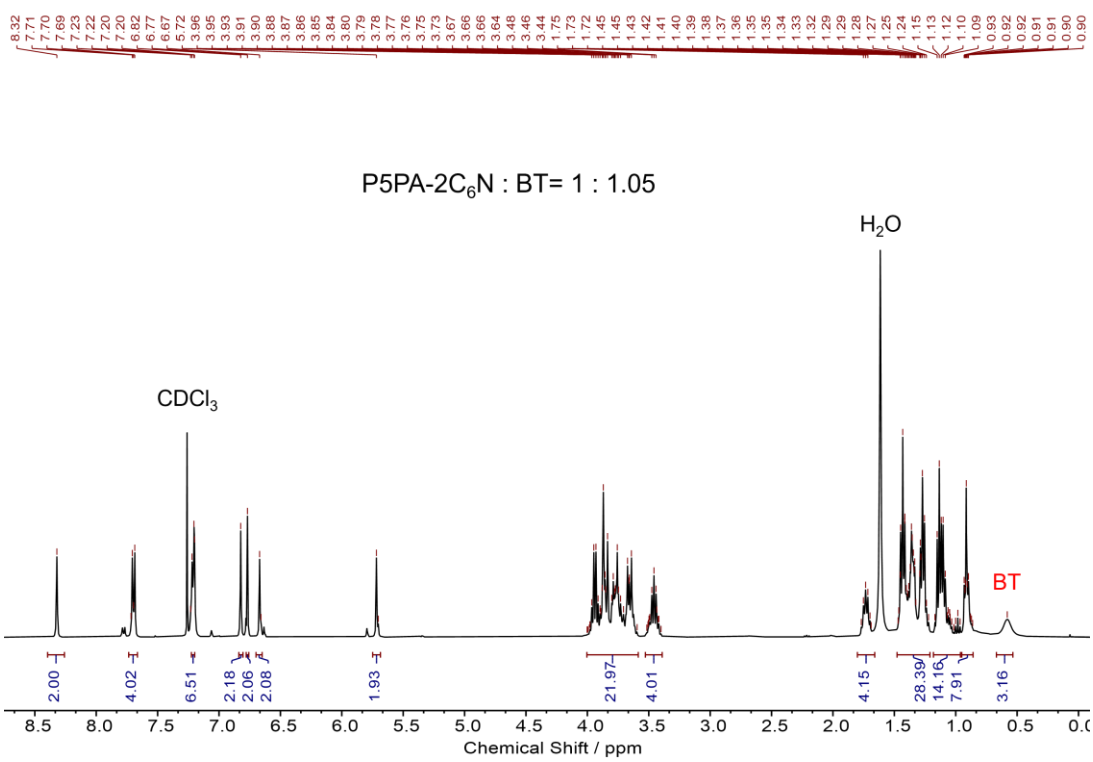

Supplementary Figure 69. ^{1}H NMR spectrum (400 MHz, $CDCl_3$, 298 K) of as-synthesized CSP-1 after exposure to butyronitrile (BT) vapor for 12 hours. BT molecules have completely replaced C_6N after exposure.

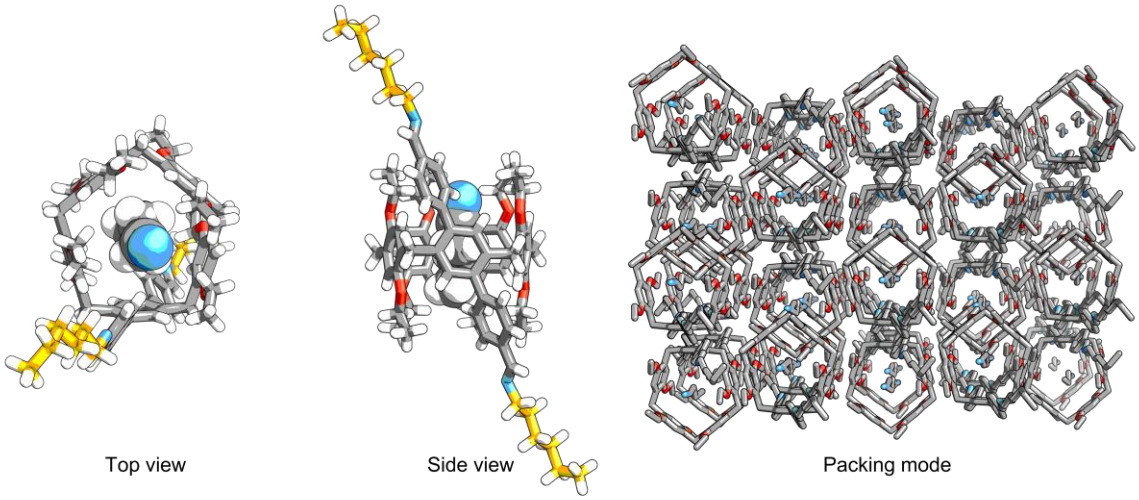

Supplementary Figure 70. SC-XRD structure of BT@P5PA-2C_6N. BT molecules insert into the cavities of P5PA-2C_6N and disrupt the SP chains.

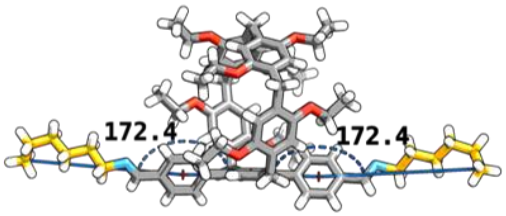

Supplementary Figure 71. The bending angles of appended *n*-hexyl chains of P5PA-2C_6N in the SC-XRD structure of BT@P5PA-2C_6N. Both *n*-hexyl chains in a P5PA-2C_6N molecule exhibit identical bending angles and adopt symmetric conformations.

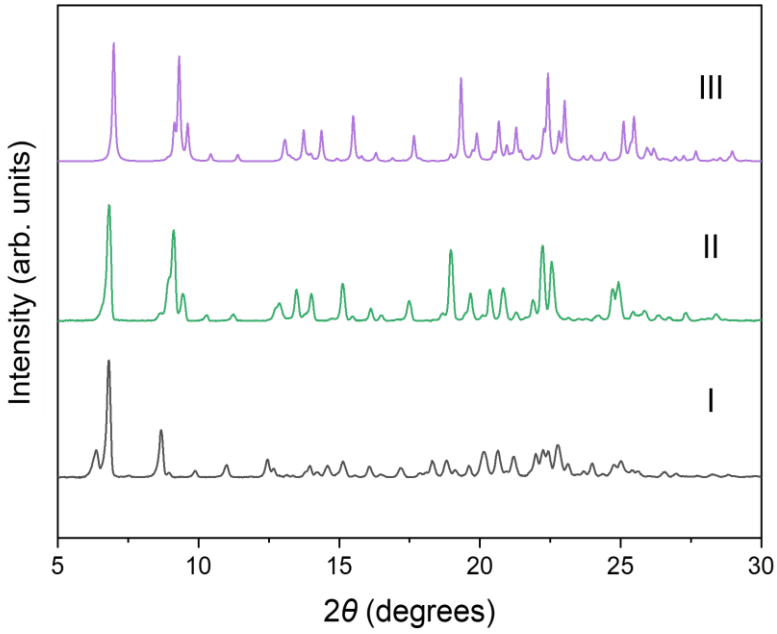

Supplementary Figure 72. PXRD patterns: (I) as-synthesized CSP-1; (II) crystals of I after exposure to BT vapor for 12 hours; (III) simulated from the SC-XRD structure of BT@P5PA-2C_6N. The phase consistency of II and III indicates that BT vapor treatment has transformed CSP-1 into BT@P5PA-2C_6N.

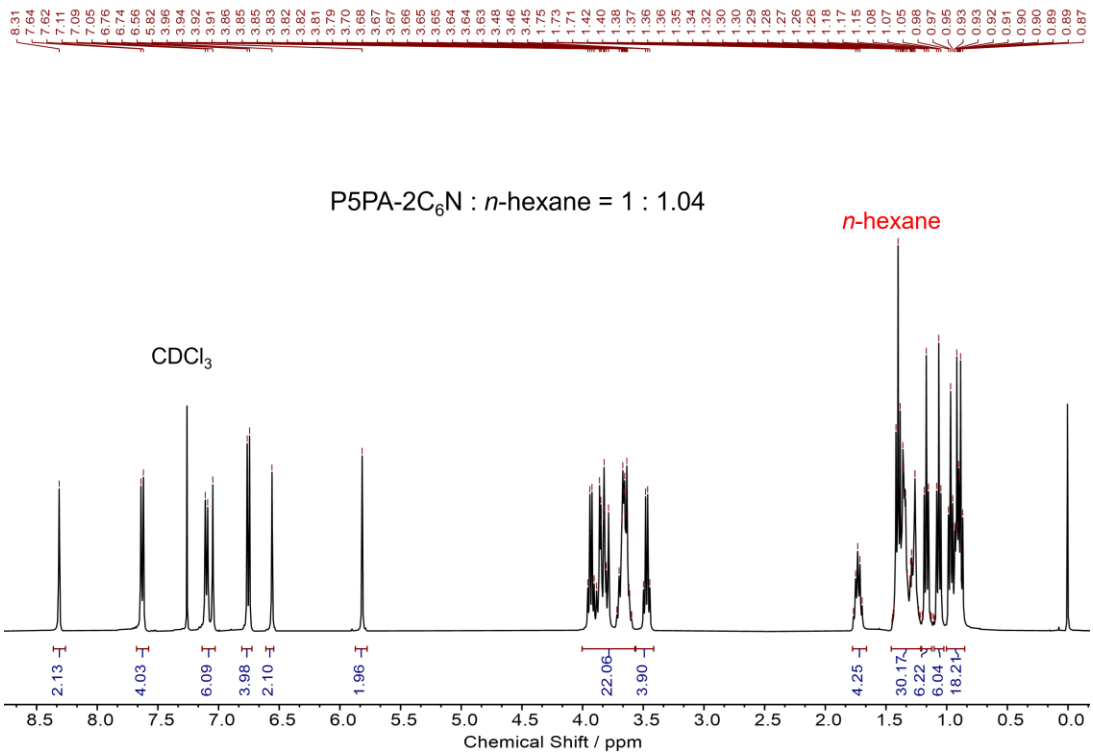

Supplementary Figure 73. ^{1}H NMR spectrum (400 MHz, $CDCl_3$, 298 K) of as-synthesized CSP-1 after exposure to *n*-hexane vapor for 12 hours.

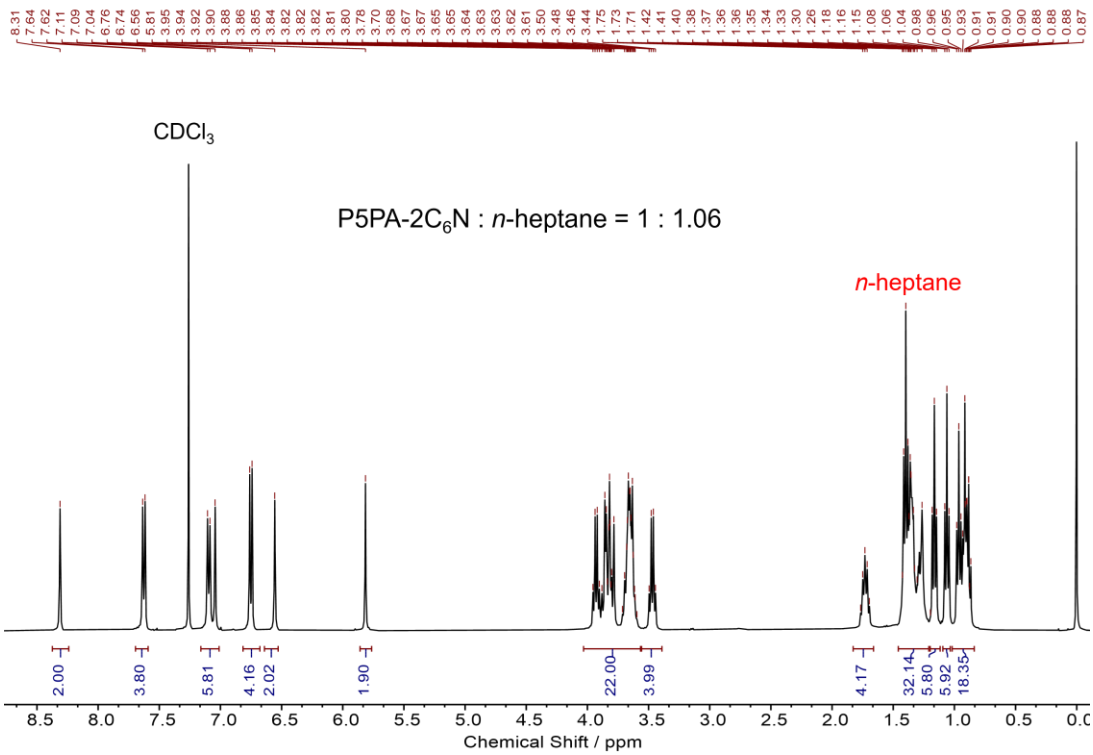

Supplementary Figure 74. ^{1}H NMR spectrum (400 MHz, $CDCl_3$, 298 K) of as-synthesized CSP-1 after exposure to *n*-heptane vapor for 12 hours.

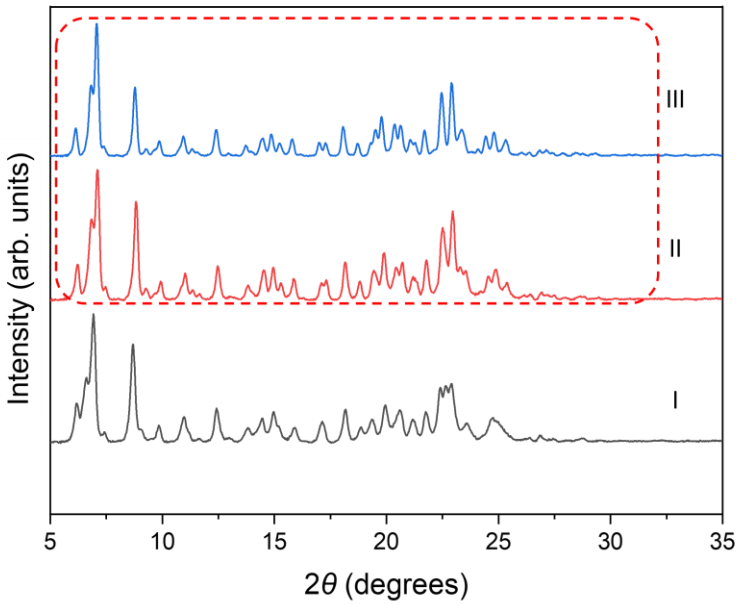

Supplementary Figure 75. PXRD patterns: (I) as-synthesized CSP-1 crystals after exposure to *n*-hexane vapor for 12 hours; (II) crystals of I after exposure to an open environment for 10 minutes; (III) solvent-free CSP-1.

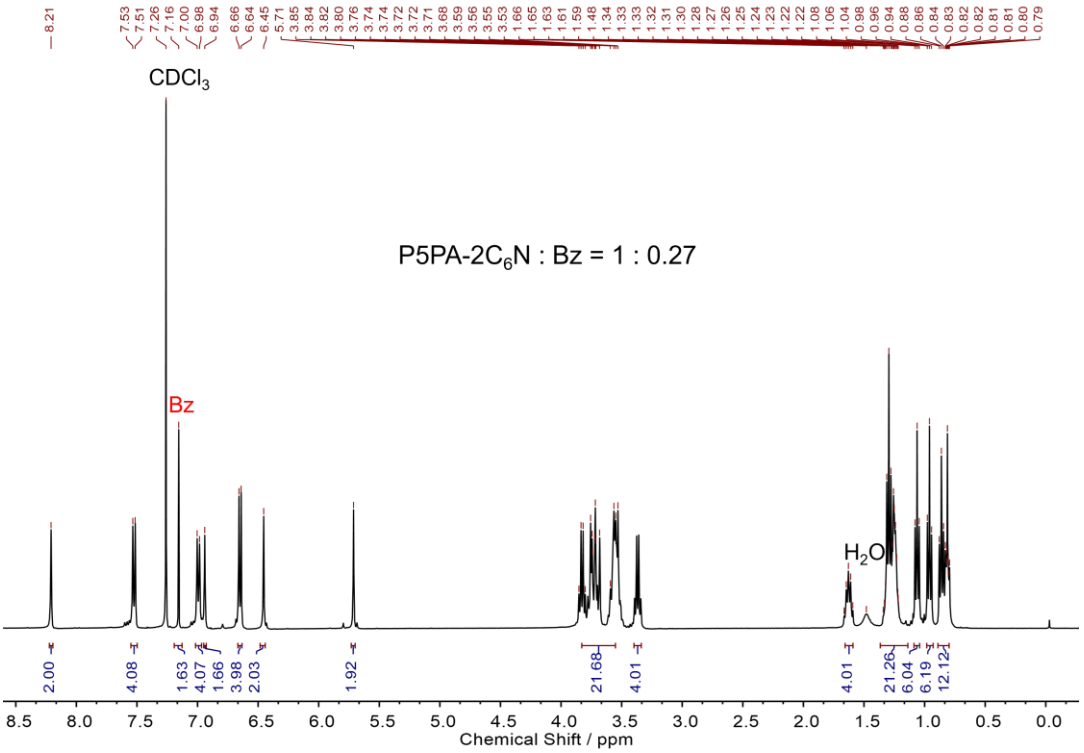

Supplementary Figure 76.[1]H NMR spectrum (400 MHz, $CDCl_3$, 298 K) of as-synthesized CSP-1 crystals after exposure to benzene vapor for 12 hours.

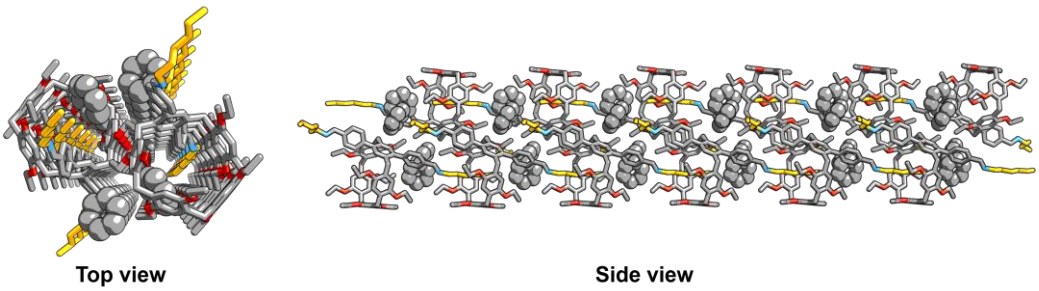

Supplementary Figure 77. Polymeric packing mode in the SC-XRD structure of Bz@P5PA-2C_6N.

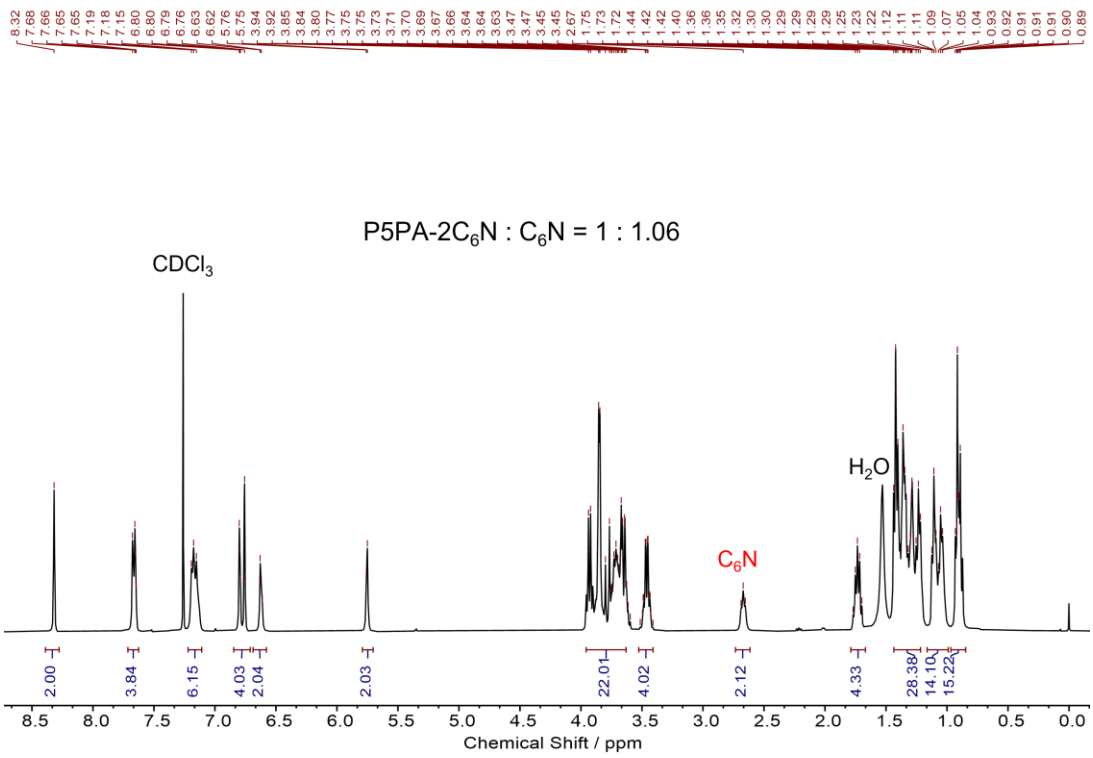

Supplementary Figure 78. ^{1}H NMR spectrum (400 MHz, $CDCl_3$, 298 K) of DisCSP crystals after exposure to C_6N vapor for 12 hours.

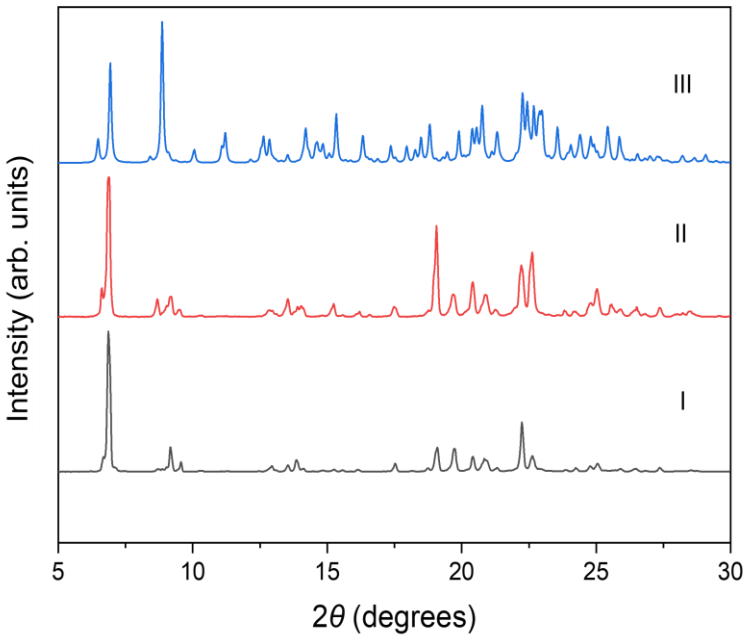

Supplementary Figure 79. PXRD patterns: (I) experimental DisCSP; (II) crystals of I after exposure to C_6N vapor for 12 hours; (III) simulated from the SC-XRD structure of CSP-1.

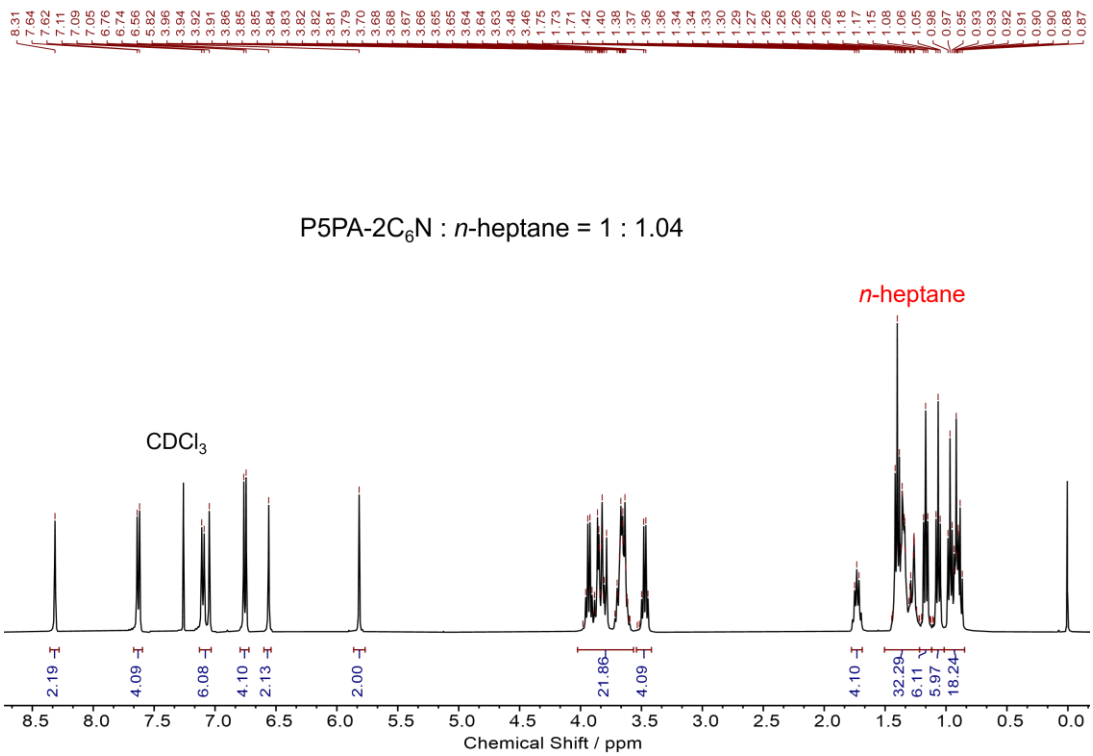

Supplementary Figure 80. ^{1}H NMR spectrum (400 MHz, $CDCl_3$, 298 K) of DisCSP crystals after exposure to *n*-heptane vapor for 12 hours. Approximately one equivalent of *n*-heptane was adsorbed.

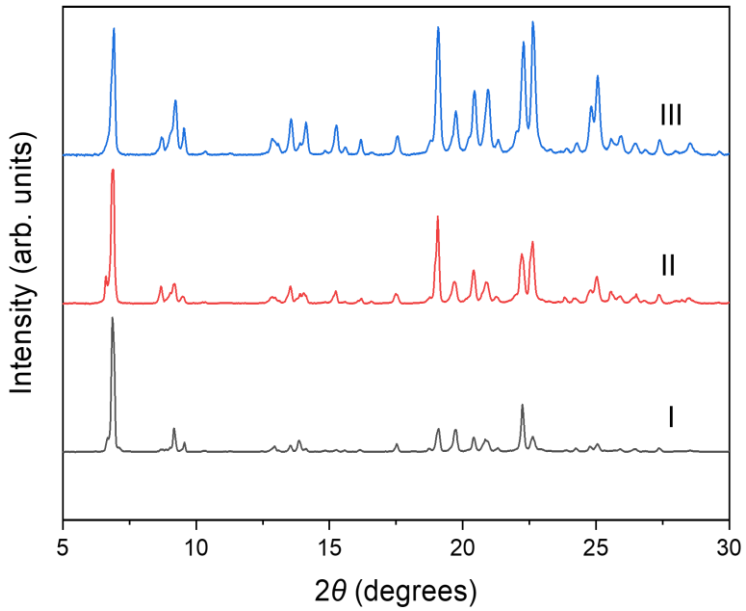

Supplementary Figure 81. PXRD patterns: (I) experimental DisCSP; (II) crystals of I after exposure to *n*-heptane vapor for 12 hours; (III) crystals of I after exposure to C_6N vapor for 12 hours. The pattern of DisCSP exhibited minimal changes after adsorption of either C_6N or *n*-heptane, indicating that the non-polymeric structure was retained.

7. Structure-controlled thermodynamic properties

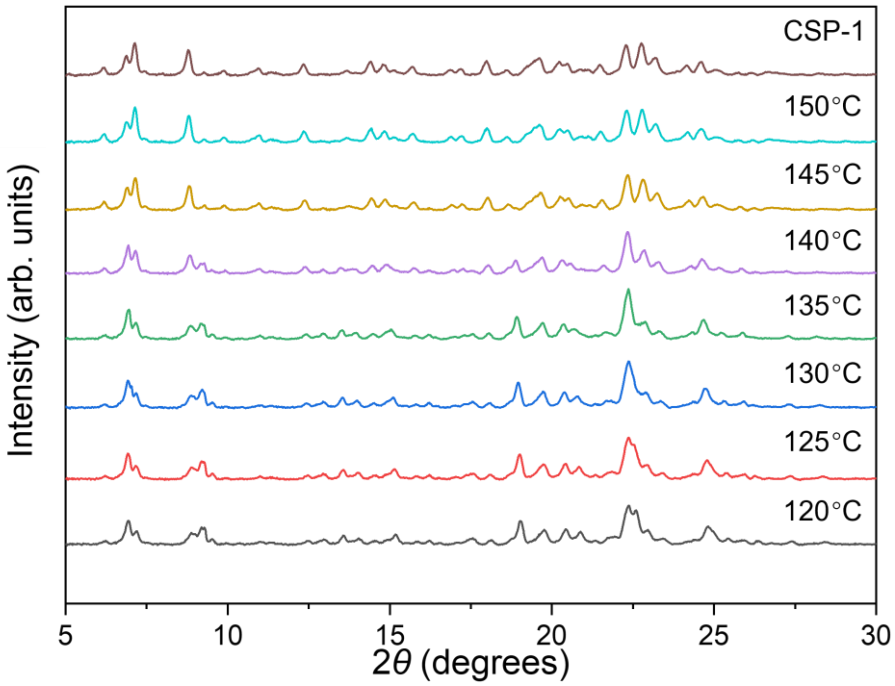

Supplementary Figure 82. PXRD patterns of DisCSP crystals after heating at different temperatures for 10 hours.

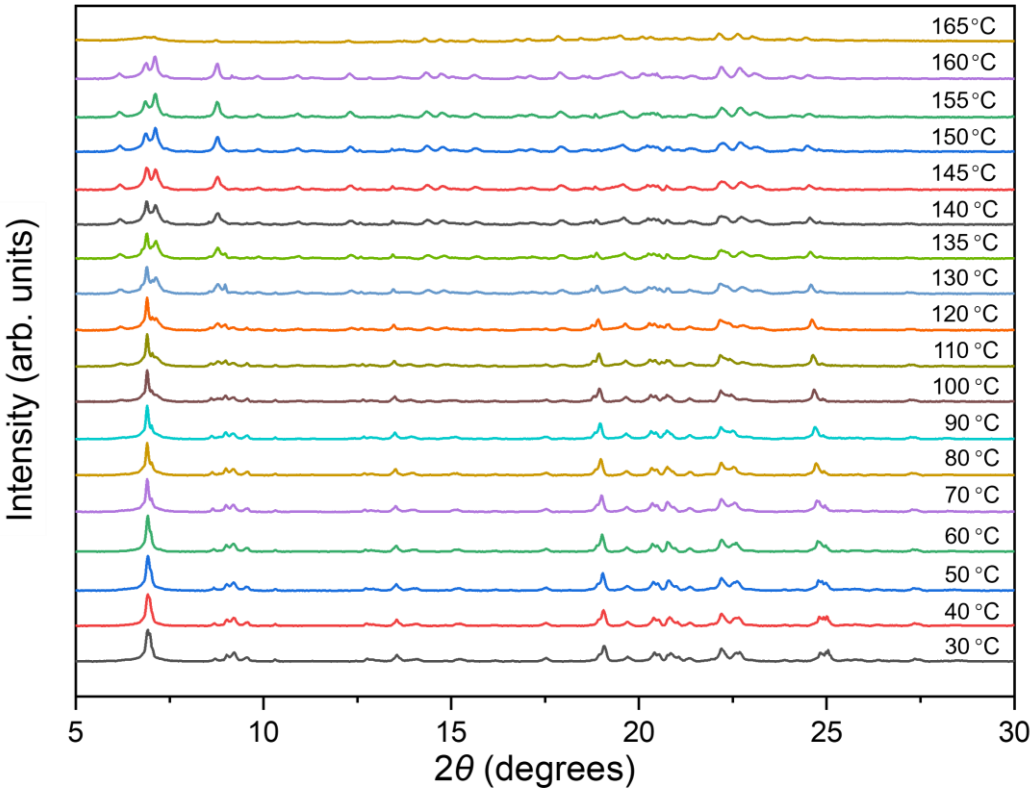

Supplementary Figure 83. VT-PXRD patterns showing the transformation from DisCSP to CSP-1 measured over the range 30–165 °C.

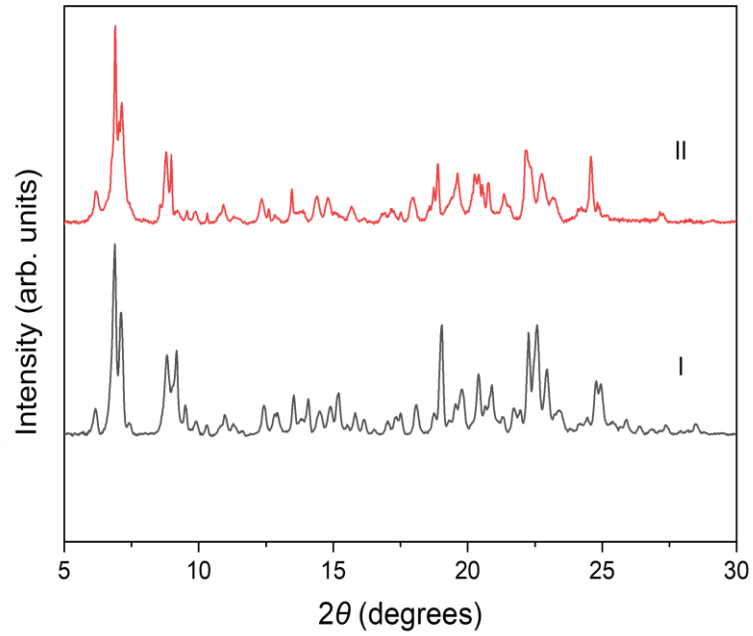

Supplementary Figure 84. PXRD patterns: (I) DisCSP/CSP-1 mixed crystals (obtained by heating DisCSP crystals at 120 °C for 10 hours); (II) crystals of I measured after 30 days.

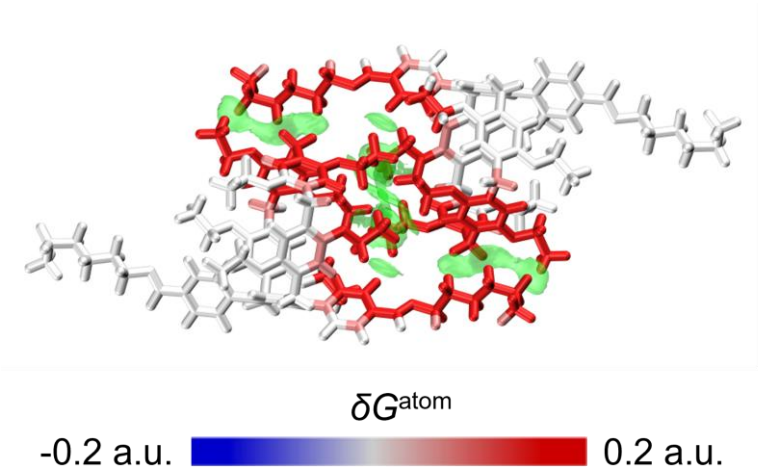

Supplementary Figure 85. Distribution of noncovalent interaction regions in DisCSP investigated by IGMH. The red-colored regions highlight the parts of P5PA-2C_6N that contribute most significantly to the overall interactions.

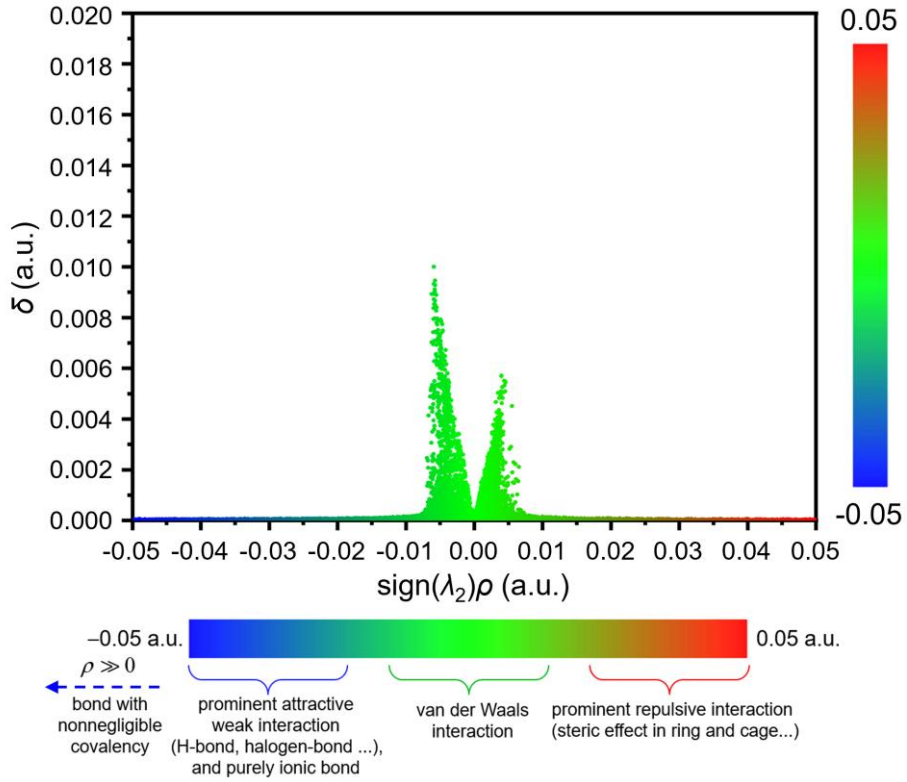

Supplementary Figure 86. IGMH scatter plot for noncovalent interactions in DisCSP.

Supplementary Table 4. Thermal correction and Gibbs free energy comparison between CSP-1 and DisCSP.

	CSP-1	**DisCSP**
Zero-point correction (Hartree)	2.286402	2.286333
Thermal correction to energy (Hartree)	2.310862	2.310491
Thermal correction to enthalpy (Hartree)	2.311807	2.311435
Thermal correction to Gibbs free energy (Hartree)	2.235067	2.235354
SCF energy (HF) (Hartree)	-7400.9635232	-7400.7848366
Total Gibbs Free Energy (Hartree)	−7398.7284562	−7398.5494826

The Gibbs free energy difference between CSP-1 and DisCSP is −0.178973 a.u., approximately −112.31 kcal/mol.

8. Crystallography data

Supplementary Table 5. Crystallography data and structural refinement summary of C_nN@P5A-2C_nN (n = 4–6).

Compounds	**C_4N@P5A-2C_4N**	**C_5N@P5A-2C_5N**	**C_6N@P5A-2C_6N**
CCDC number	2456988	2458746	2458745
Empirical formula	$C_{61}H_{80}N_2O_8 \cdot C_4H_{11}N$	$C_{63}H_{84}N_2O_8 \cdot C_5H_{13}N$	$C_{65}H_{88}N_2O_8 \cdot C_3H_{7.9}N_{0.7} \cdot C_3H_{7.1}N_{0.3}$
Formula weight	1042.40	1084.48	1126.56
Temperature (K)	193.00	193.00	193.00
Crystal system	triclinic	triclinic	monoclinic
Space group	$P\bar{1}$	$P\bar{1}$	Cc
a (Å)	12.3277(5)	12.3250(4)	22.1711(9)
b (Å)	13.0597(6)	13.2218(4)	16.3514(6)
c (Å)	21.9372(12)	22.1045(7)	19.9067(7)
α (°)	87.319(2)	87.4250(10)	90
B (°)	84.914(2)	85.1630(10)	108.4640(10)
Γ (°)	63.2090(10)	63.7450(10)	90
Volume (Å^3)	3140.2(3)	3218.88(18)	6845.2(4)
Z	2	2	4
ρ_{calc} (gcm^{-3})	1.102	1.119	1.093
μ (mm^{-1})	0.072	0.072	0.070
F(000)	1132	1180	2456
Crystal size (mm^3)	0.13×0.11×0.09	0.2×0.15×0.1	0.15×0.12×0.1
Radiation	MoK_α (λ=0.71073 Å)	MoK_α (λ=0.71073 Å)	MoK_α (λ=0.71073 Å)
Reflections collected	21617	24839	31719
Independent reflections	10820 R_{int} = 0.0487 R_{sigma} = 0.0698	11292 R_{int} = 0.0425 R_{sigma} = 0.0644	12125 R_{int} = 0.0481 R_{sigma} = 0.0568
Goodness-of-fit on F^2	1.375	1.041	1.040
Final R indexes [$I \geq 2\sigma(I)$]	R_1 = 0.1165 wR_2 = 0.3388	R_1 = 0.0905 wR_2 = 0.2493	R_1 = 0.0643 wR_2 = 0.1689
Final R indexes [all data]	R_1 = 0.1604 wR_2 = 0.3892	R_1 = 0.1403 wR_2 = 0.2930	R_1 = 0.0871 wR_2 = 0.1888

Supplementary Table 6. Crystallography data and structural refinement summary of C_nN@P5MA-$2C_nN$ (n = 4–6).

Compounds	**C_4N@P5MA-$2C_4N$**	**C_5N@P5MA-$2C_5N$**	**C_6N@P5MA-$2C_6N$**
CCDC number	2458734	2458735	2458736
Empirical formula	$C_{73}H_{88}N_2O_8 \cdot C_4H_{11}N$	$C_{75}H_{92}N_2O_8 \cdot C_5H_{13}N$	$C_{77}H_{96}N_2O_8 \cdot C_6H_{15}N$
Formula weight	1194.59	1236.66	1278.74
Temperature (K)	193.15	193.00	193.00
Crystal system	monoclinic	monoclinic	orthorhombic
Space group	$P2_1/c$	$P2_1/c$	$Pca2_1$
a (Å)	23.3665(15)	20.7346(11)	16.6463(6)
b (Å)	14.8643(10)	16.9808(9)	19.0766(8)
c (Å)	22.0177(14)	22.3104(13)	24.2178(9)
α (°)	90	90	90
β (°)	112.771(2)	111.251(2)	90
γ (°)	90	90	90
Volume (Å^3)	7051.3(8)	7321.1(7)	7690.5(5)
Z	4	4	4
ρ_{calc} (gcm^{-3})	1.125	1.122	1.104
μ (mm^{-1})	0.072	0.071	0.070
F(000)	2584	2680	2776
Crystal size (mm^3)	0.13×0.11×0.1	0.4×0.2×0.1	0.15×0.12×0.1
Radiation	MoK_α (λ=0.71073 Å)	MoK_α (λ=0.71073 Å)	MoK_α (λ=0.71073 Å)
Reflections collected	62079	65562	57178
Independent reflections	16123 R_{int} = 0.0871 R_{sigma} = 0.0876	16778 R_{int} = 0.1032 R_{sigma} = 0.1040	12774 R_{int} = 0.0847 R_{sigma} = 0.0802
Goodness-of-fit on F^2	1.047	1.032	1.021
Final R indexes [I≥2σ(I)]	R_1 = 0.0999 wR_2 = 0.2081	R_1 = 0.1058 wR_2 = 0.2365	R_1 = 0.0836 wR_2 = 0.2105
Final R indexes [all data]	R_1 = 0.1899 wR_2 = 0.2601	R_1 = 0.2004 wR_2 = 0.2960	R_1 = 0.1452 wR_2 = 0.2536

Supplementary Table 7. Crystallography data and structural refinement summary of C_nN@P5PA-$2C_nN$ (n = 3–5).

Compounds	**C_3N@P5PA-$2C_3N$**	**C_4N@P5PA-$2C_4N$**	**C_5N@P5PA-$2C_5N$**
CCDC number	2457557	2457558	2457559
Empirical formula	$C_{71}H_{84}N_2O_8 \cdot C_3H_9N$	$2(C_{73}H_{88}N_2O_8) \cdot 3(C_4H_{11}N)$	$2(C_{75}H_{92}N_2O_8) \cdot 3(C_5H_{13}N)$
Formula weight	1152.51	2462.31	2560.49
Temperature (K)	193.00	193.00	193.15
Crystal system	monoclinic	monoclinic	monoclinic
Space group	$P2_1/c$	$P2_1/c$	$P2_1/c$
a (Å)	12.1177(3)	12.5336(5)	12.7335(8)
b (Å)	22.0234(5)	21.9851(9)	22.2143(13)
c (Å)	26.3153(6)	26.6642(10)	27.0955(16)
α (°)	90	90	90
β (°)	100.2360(10)	101.478(2)	103.580(2)
γ (°)	90	90	90
Volume (Å^3)	6911.1(3)	7200.4(5)	7450.1(8)
Z	4	2	2
ρ_{calc} (gcm^{-3})	1.108	1.136	1.141
μ (mm^{-1})	0.071	0.072	0.072
F (000)	2488	2668	2780
Crystal size (mm^3)	0.5×0.13×0.13	0.15×0.13×0.1	0.17×0.16×0.15
Radiation	MoK_α (λ=0.71073 Å)	MoK_α (λ=0.71073 Å)	MoK_α (λ=0.71073 Å)
Reflections collected	65838	55006	54218
Independent reflections	15865 R_{int} = 0.1378 R_{sigma} = 0.0969	12685 R_{int} = 0.1532 R_{sigma} = 0.0979	13143 R_{int} = 0.0643 R_{sigma} = 0.0602
Goodness-of-fit on F^2	1.022	1.017	1.017
Final R indexes [$I \geq 2\sigma(I)$]	R_1 = 0.0889 wR_2 = 0.2042	R_1 = 0.0963 wR_2 = 0.2389	R_1 = 0.0936 wR_2 = 0.2303
Final R indexes [all data]	R_1 = 0.1633 wR_2 = 0.2526	R_1 = 0.1632 wR_2 = 0.2931	R_1 = 0.1560 wR_2 = 0.2759

Supplementary Table 8. Crystallography data and structural refinement summary of CSP-1 and MeOH@P5MA-2Aniline.

Compounds	**CSP-1**	**MeOH@P5MA-2Aniline**
CCDC number	2457560	2457592
Empirical formula	$C_{77}H_{96}N_2O_8 \cdot C_{3.7}H_{9.0}{}_5N_{0.5} \cdot C_{2.3}H_{4.95} \cdot 0.5(H_2N)$	$C_{77}H_{80}N_2O_8 \cdot 1.25(CH_4O)$
Formula weight	1278.74	1201.48
Temperature (K)	193.00	193.0
Crystal system	triclinic	monoclinic
Space group	$P\bar{1}$	$P2_1/c$
a (Å)	13.8837(9)	14.4998(14)
b (Å)	14.2389(9)	36.265(4)
c (Å)	19.1060(13)	13.1784(13)
α (°)	73.487(2)	90
β (°)	83.183(2)	93.078(5)
γ (°)	85.016(2)	90
Volume [Å^3]	3590.0(4)	6919.6(12)
Z	2	4
ρ_{calc} (gcm^{-3})	1.183	1.153
μ (mm^{-1})	0.372	0.075
F (000)	1388	2570
Crystal size (mm^3)	0.1×0.13×0.15	0.5×0.5×0.2
Radiation	GaK_α (λ=1.34139 Å)	MoK_α (λ=0.71073 Å)
Reflections collected	42245	57935
Independent reflections	12553 R_{int} = 0.0517 R_{sigma} = 0.0523	12661 R_{int} = 0.0801 R_{sigma} = 0.0665
Goodness-of-fit on F^2	1.047	1.065
Final R indexes [$I \geq 2\sigma(I)$]	R_1 = 0.0931 wR_2 = 0.2646	R_1 = 0.0739 wR_2 = 0.2066
Final R indexes [all data]	R_1 = 0.1341 wR_2 = 0.3077	R_1 = 0.1127 wR_2 = 0.2354

Supplementary Table 9. Crystallography data and structural refinement summary of DCE@P5PA-2C$_6$N, BT@P5PA-2C$_6$N, and Bz@P5PA-2C$_6$N.

Compounds	**DCE@P5PA-2C$_6$N**	**BT@P5PA-2C$_6$N**	**Bz@P5PA-2C$_6$N**
CCDC number	2458759	2458758	2459063
Empirical formula	$C_{77}H_{96}N_2O_8 \cdot C_2H_4Cl_2$	$C_{77}H_{96}N_2O_8 \cdot C_4H_7N$	$C_{77}H_{96}N_2O_8 \cdot 2(C_6H_6)$
Formula weight	1276.50	1246.66	1333.77
Temperature (K)	293.00	193.00	193.0
Crystal system	triclinic	monoclinic	triclinic
Space group	$P\bar{1}$	$C2/c$	$P\bar{1}$
a (Å)	14.206(2)	22.453(2)	14.7395(17)
b (Å)	14.218(2)	16.9456(17)	15.3526(18)
c (Å)	21.264(3)	21.8897(19)	18.554(2)
α (°)	106.609(5)	90	102.494(3)
β (°)	101.147(6)	117.950(5)	99.851(3)
γ (°)	106.476(5)	90	98.624(3)
Volume [Å^3]	3766.6(10)	7357.1(12)	3961.8(8)
Z	2	4	2
ρ_{calc} (gcm^{-3})	1.126	1.126	1.118
μ (mm^{-1})	0.139	0.071	0.070
F (000)	1372	2696	1440
Crystal size (mm^3)	0.2×0.1×0.1	0.15×0.1×0.1	0.11×0.12×0.13
Radiation	MoK_α (λ=0.71073 Å)	MoK_α (λ=0.71073 Å)	MoK_α (λ=0.71073 Å)
Reflections collected	28729	28127	30458
Independent reflections	13108 R_{int} = 0.0575 R_{sigma} = 0.0919	6491 R_{int} = 0.0965 R_{sigma} = 0.0872	18004 R_{int} = 0.0565 R_{sigma} = 0.1247
Goodness-of-fit on F^2	1.012	1.018	1.014
Final R indexes [I≥2σ(I)]	R_1 = 0.0735 wR_2 = 0.1690	R_1 = 0.0819 wR_2 = 0.2023	R_1 = 0.1205 wR_2 = 0.2820
Final R indexes [all data]	R_1 = 0.1750 wR_2 = 0.2326	R_1 = 0.1784 wR_2 = 0.2606	R_1 = 0.2352 wR_2 = 0.3574

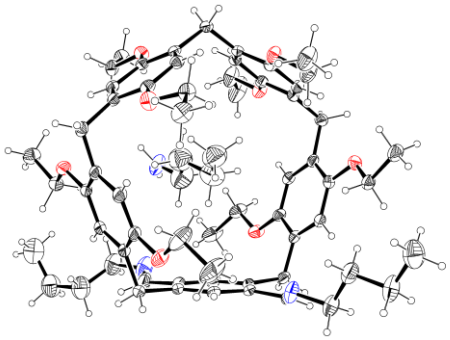

Supplementary Figure 87. ORTEP-style illustration of the asymmetric unit of C_4N@P5A-2C_4N at 193 K (CCDC no. 2456988). C and H atoms are shown in black, N atoms in blue, and O atoms in red. Ellipsoids are depicted at 25% probability level.

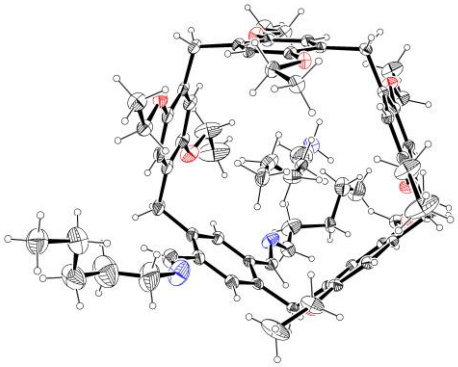

Supplementary Figure 88. ORTEP-style illustration of the asymmetric unit of C_5N@P5A-2C_5N at 193 K (CCDC no. 2458746). C and H atoms are shown in black, N atoms in blue, and O atoms in red. Ellipsoids are depicted at 20% probability level.

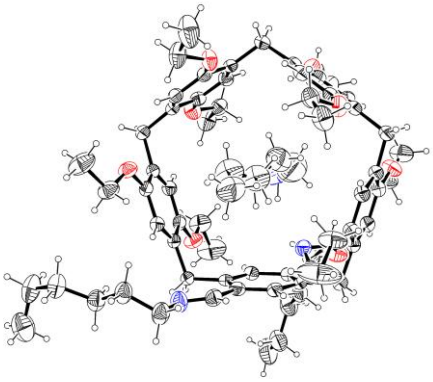

Supplementary Figure 89. ORTEP-style illustration of the asymmetric unit of C_6N@P5A-2C_6N at 193 K (CCDC no. 2458745). C and H atoms are shown in black, N atoms in blue, and O atoms in red. Ellipsoids are depicted at 50% probability level.

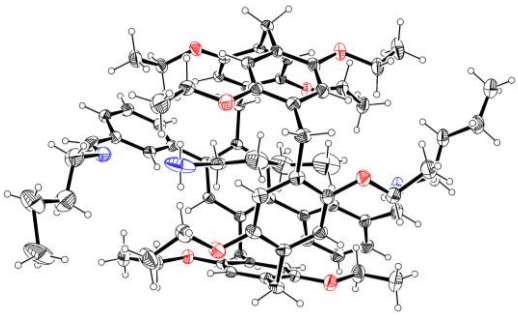

Supplementary Figure 90. ORTEP-style illustration of the asymmetric unit of C_4N@P5MA-2C_4N at 193 K (CCDC no. 2458734). C and H atoms are shown in black, N atoms in blue, and O atoms in red. Ellipsoids are depicted at 25% probability level.

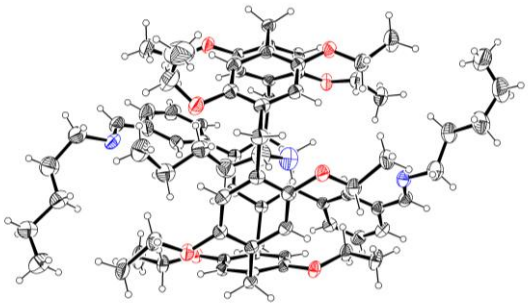

Supplementary Figure 91. ORTEP-style illustration of the asymmetric unit of C_5N@P5MA-2C_5N at 193 K (CCDC no. 2458735). C and H atoms are shown in black, N atoms in blue, and O atoms in red. Ellipsoids are depicted at 30% probability level.

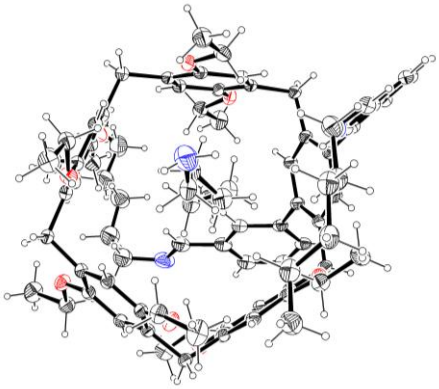

Supplementary Figure 92. ORTEP-style illustration of the asymmetric unit of C_6N@P5MA-2C_6N at 193 K (CCDC no. 2458736). C and H atoms are shown in black, N atoms in blue, and O atoms in red. Ellipsoids are depicted at 20% probability level.

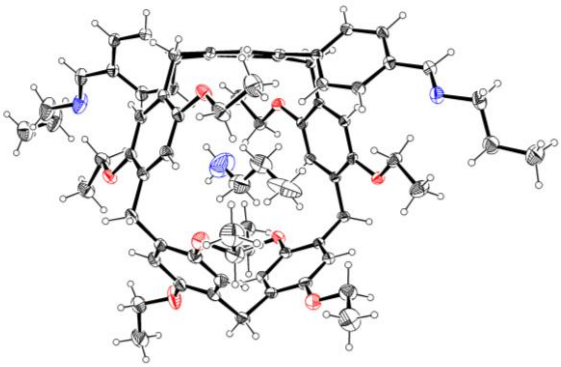

Supplementary Figure 93. ORTEP-style illustration of the asymmetric unit of C_3N@P5PA-2C_3N at 193 K (CCDC no. 2457557). C and H atoms are shown in black, N atoms in blue, and O atoms in red. Ellipsoids are depicted at 25% probability level.

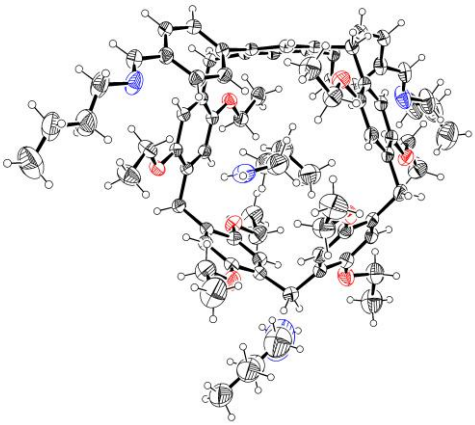

Supplementary Figure 94. ORTEP-style illustration of the asymmetric unit of C_4N@P5PA-2C_4N at 193 K (CCDC no. 2457558). C and H atoms are shown in black, N atoms in blue, and O atoms in red. Ellipsoids are depicted at 35% probability level.

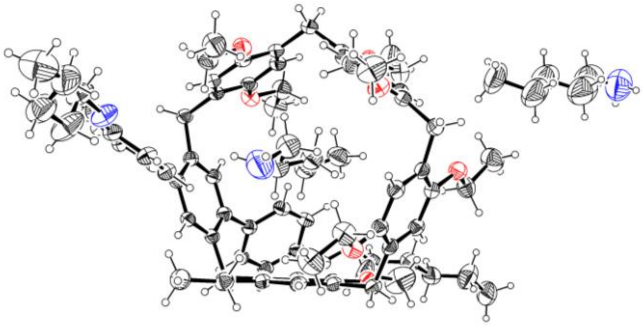

Supplementary Figure 95. ORTEP-style illustration of the asymmetric unit of C_5N@P5PA-2C_5N at 193 K (CCDC no. 2457559). C and H atoms are shown in black, N atoms in blue, and O atoms in red. Ellipsoids are depicted at 30% probability level.

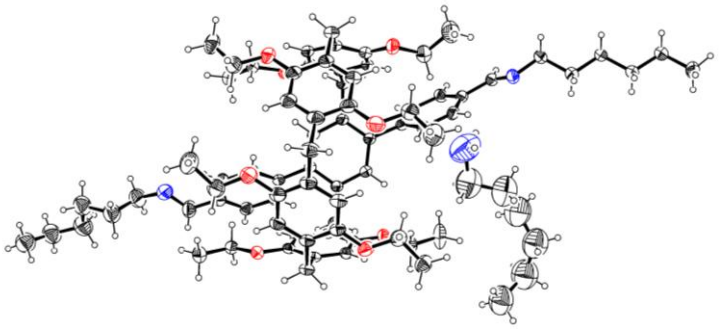

Supplementary Figure 96. ORTEP-style illustration of the asymmetric unit of CSP-1 at 193 K (CCDC no. 2457560). C and H atoms are shown in black, N atoms in blue, and O atoms in red. Ellipsoids are depicted at 30% probability level.

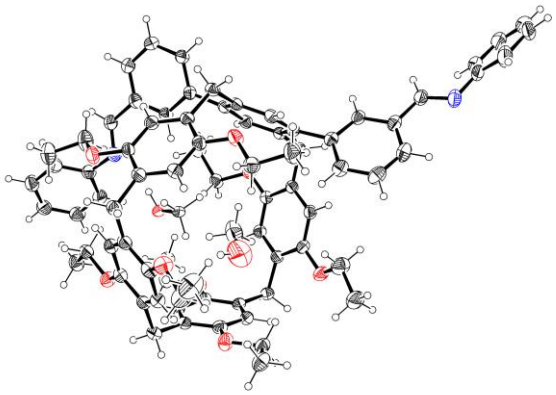

Supplementary Figure 97. ORTEP-style illustration of the asymmetric unit of MeOH@P5MA-2Aniline at 193 K (CCDC no. 2457592). C and H atoms are shown in black, N atoms in blue, and O atoms in red. Ellipsoids are depicted at 35% probability level.

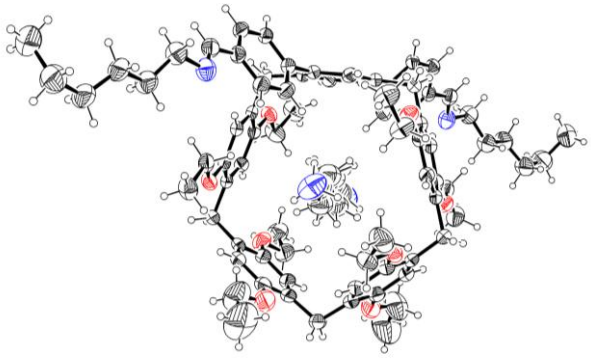

Supplementary Figure 98. ORTEP-style illustration of the asymmetric unit of BT@P5PA-2C_6N at 193 K (CCDC no. 2458758). C and H atoms are shown in black, N atoms in blue, and O atoms in red. Ellipsoids are depicted at 35% probability level.

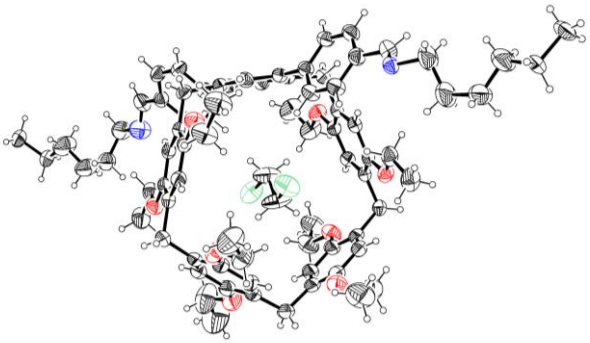

Supplementary Figure 99. ORTEP-style illustration of the asymmetric unit of DCE@P5PA-2C_6N at 293 K (CCDC no. 2458759). C and H atoms are shown in black, N atoms in blue, and O atoms in red. Ellipsoids are depicted at 30% probability level.

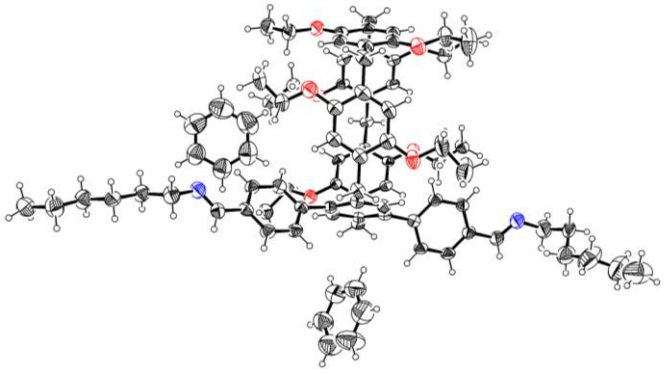

Supplementary Figure 100. ORTEP-style illustration of the asymmetric unit of Bz@P5PA-2C_6N at 293 K (CCDC no. 2459063). C and H atoms are shown in black, N atoms in blue, and O atoms in red. Ellipsoids are depicted at 35% probability level.

Notes: List of all CheckCif A- and B-level alerts in the reported crystal structures with justifications (the same justifications were included in the cif files deposited with CSD).

1. Crystal structure of C_4N@P5A-2C_4N (CCDC no. 2456988):

   PLAT084_ALERT_3_B High wR2 Value (i.e. > 0.25) ..... 0.39 Report

   The relatively high wR2 value is mainly associated with the partial disorder of the guest molecules and the resulting complexity of the refinement. Appropriate restraints were applied during refinement. This alert does not affec the structural assignment or the conclusions of this work.

2. Crystal structure of C_6N@P5MA-2C_6N (CCDC no. 2458736):

   PLAT340_ALERT_3_B Low Bond Precision on C-C Bonds ..... 0.01308 Ang.

   The relatively low bond precision is mainly associated with the partial disorder of the guest

molecules. Appropriate restraints were applied during refinement to model the disorder. This alert does not affect the structural assignment or the conclusions of this work.

3. Crystal structure of Bz@P5PA-2C_6N (CCDC no. 2459063):

   PLAT084_ALERT_3_B High wR2 Value (i.e. > 0.25) ..... 0.36 Report

   The relatively high wR2 value reflects the complexity of the refinement. Appropriate restraints were applied during refinement to obtain the best structural model. This alert does not affect the structural assignment or the conclusions of this work.

9. References

1. Stephens, P. J., Devlin, F. J., Chabalowski, C. F. & Frisch, M. J. Ab initio calculation of vibrational absorption and circular dichroism spectra using density functional force fields. *J. Phys. Chem.* **98**, 11623–11627 (1994).
2. Lee, C., Yang, W. & Parr, R. G. Development of the Colle-Salvetti correlation-energy formula into a functional of the electron density. *Phys. Rev. B* **37**, 785–789 (1988).
3. Becke, A. D. Density-functional thermochemistry. III. The role of exact exchange. *J. Chem. Phys.* **98**, 5648–5652 (1993).
4. Becke, A. D. A new mixing of Hartree–Fock and local density-functional theories. *J. Chem. Phys.* **98**, 1372–1377 (1993).
5. Rassolov, V. A., Pople, J. A., Ratner, M. A. & Windus, T. L. 6-31G* basis set for atoms K through Zn. *J. Chem. Phys.* **109**, 1223–1229 (1998).
6. Krishnan, R., Binkley, J. S., Seeger, R. & Pople, J. A. Self-consistent molecular orbital methods. XX. A basis set for correlated wave functions. *J. Chem. Phys.* **72**, 650–654 (1980).
7. Weigend, F. & Ahlrichs, R. Balanced basis sets of split valence, triple zeta valence and quadruple zeta valence quality for H to Rn: design and assessment of accuracy. *Phys. Chem. Chem. Phys.* **7**, 3297–3305 (2005).
8. Adamo, C. & Barone, V. Toward reliable density functional methods without adjustable parameters: the PBE0 model. *J. Chem. Phys.* **110**, 6158–6170 (1999).
9. Lu, T. & Chen, F. Multiwfn: a multifunctional wavefunction analyzer. *J. Comput. Chem.* **33**, 580–592 (2012).
10. Lu, T. A comprehensive electron wavefunction analysis toolbox for chemists, Multiwfn. *J. Chem. Phys.* **161**, 082503 (2024).
11. Lu, T. & Chen, Q. Independent gradient model based on Hirshfeld partition: a new method for visual study of interactions in chemical systems. *J. Comput. Chem.* **43**, 539–555 (2022).
12. Humphrey, W., Dalke, A. & Schulten, K. VMD: visual molecular dynamics. *J. Mol. Graph.* **14**, 33–38 (1996).
13. Purse, B. W. & Rebek, J. Self-fulfilling cavitands: packing alkyl chains into small spaces. *Proc. Natl Acad. Sci. USA* **103**, 2530–2534 (2006).
14. Ogi, S., Stepanenko, V., Thein, J. & Würthner, F. Impact of alkyl spacer length on aggregation pathways in kinetically controlled supramolecular polymerization. *J. Am. Chem. Soc.* **138**, 670–

678 (2016).

15. Matoba, S. et al. Directional supramolecular polymerization in a dynamic microsolution: a linearly moving polymer's end striking monomers. *J. Am. Chem. Soc.* **143**, 8731–8746 (2021).